

REPORT DOCUMENTATION PAGE		Form Approved OMB NO. 0704-0188	
Public Reporting Burden for this collection of information is estimated to average 1 hour per response, including the time for reviewing instructions, searching existing data sources, gathering and maintaining the data needed, and completing and reviewing the collection of information. Send comment regarding this burden estimate or any other aspect of this collection of information, including suggestions for reducing this burden, to Washington Headquarters Services, Directorate for Information Operations and Reports, 1215 Jefferson Davis Highway, Suite 1204, Arlington VA, 22202-4302, and to the Office of Management and Budget, Paperwork Reduction Project (0704-0188), Washington DC 20503			
1. AGENCY USE ONLY (Leave Blank)		2. REPORT DATE:	3. REPORT TYPE AND DATES COVERED Final Report 20-Sep-2001 - 19-Jul-2005
4. TITLE AND SUBTITLE Experimental determination of shock structures in hetrogeneous layered material systems.		5. FUNDING NUMBERS DAAD190110782	
6. AUTHORS Liren Tsai, Vikas Prakash		8. PERFORMING ORGANIZATION REPORT NUMBER	
7. PERFORMING ORGANIZATION NAMES AND ADDRESSES Case Western Reserve University 10900 Euclid Avenue Cleveland, OH 44106 -7221			
9. SPONSORING/MONITORING AGENCY NAME(S) AND ADDRESS(ES) U.S. Army Research Office P.O. Box 12211 Research Triangle Park, NC 27709-2211		10. SPONSORING / MONITORING AGENCY REPORT NUMBER 42552-MS.2	
11. SUPPLEMENTARY NOTES The views, opinions and/or findings contained in this report are those of the author(s) and should not contrued as an official Department of the Army position, policy or decision, unless so designated by other documentation.			
12. DISTRIBUTION AVAILIBILITY STATEMENT Approved for Public Release; Distribution Unlimited		12b. DISTRIBUTION CODE	
13. ABSTRACT (Maximum 200 words) The abstract is below since many authors do not follow the 200 word limit			
14. SUBJECT TERMS Heterogeneous material, S2 glass polymer matrix composites, layered material, Floquet Theory, plate impact experiments, structure of shock wave, shock induced compression,		15. NUMBER OF PAGES Unknown due to possible attachments	
		16. PRICE CODE	
17. SECURITY CLASSIFICATION OF REPORT UNCLASSIFIED	18. SECURITY CLASSIFICATION ON THIS PAGE UNCLASSIFIED	19. SECURITY CLASSIFICATION OF ABSTRACT UNCLASSIFIED	20. LIMITATION OF ABSTRACT UL

Report Title

Experimental determination of shock structures in heterogeneous layered material systems.

ABSTRACT

In the present study, in an attempt to better understand the dynamic response of heterogeneous materials, a combined analytical and experimental study is conducted on elastic-elastic and elastic-viscoelastic bilaminates. The analytical approach makes use of the Laplace transform and Floquet theory for ODE with periodic coefficients. The effects of material impedance mismatch, layer density and material inelasticity on shock wave propagation through elastic-elastic and elastic-viscoelastic bilaminates were studied. Besides the study on bilaminates, several series of plate impact experiments were performed on GRP. By varying the shock compression stress and GRP specimen thicknesses, the structure of shock waves in GRP were investigated. From the measurements of the free surface particle velocity history, the Equation of State, Hugoniot Elastic Limit and Hugoniot curve of GRP were determined. The spall strength of GRP was also studied by conducting a series of both normal-impact and combined pressure-shear plate impact experiments. The spall strength was found to decrease dramatically with increasing compression stress and increasing shear strain. Shock-resock and shock-release experiments were performed to determine the dynamic yield strength of GRP. The calculated dynamic yield strength was found to increase by approximately a factor of 10 within the test range.

List of papers submitted or published that acknowledge ARO support during this reporting period. List the papers, including journal references, in the following categories:

(a) Papers published in peer-reviewed journals (N/A for none)

Tsai, L. and Prakash, V. (2004). Structure of weak shock Waves in Periodically Layered Material Systems, International Journal of Solids and Structures, vol 42/2, pp.727-750.

Number of Papers published in peer-reviewed journals: 1.00

(b) Papers published in non-peer-reviewed journals or in conference proceedings (N/A for none)

Liren Tsai and Vikas Prakash. Dynamic Response and Spall Strength of S2 Glass Fiber Reinforced Polymer Composite. Proceedings of the 2005 SEM Annual Conference and Exposition on Experimental and Applied Mechanics, Portland, OR, Paper # 322.

Vikas Prakash and Liren Tsai. (2005). Shock Response of S2-glass Fiber Reinforced Polymer Composites. Dislocations, Plasticity, Damage and Metal Forming: Material Response and Multiscale Modeling. Proceedings of PLASTICITY'05: The Eleventh International Symposium on Plasticity and its Current Applications, Hawaii. Editors: A.S. Khan and Amir Khoei, NEAT Press, MD, pp 364-366.

Tsai, L. and Prakash, V. (2003). Dispersion and Attenuation of Stress Waves in layered Heterogeneous Material Systems. Proceedings of the 9th International Conference on the Mechanical Behavior of Materials, Geneva, Switzerland, May 25 to 29, 2003.

Tsai, L. and Prakash, V. (2003). Stress wave Propagation in Elastic-Elastic and Elastic-Viscoelastic Bilaminates. Proceedings of the 2003 SEM Annual Conference and Exposition on Experimental and Applied Mechanics, Charlotte, NC, USA, June 2-4, 2003.

Tsai, L. and Prakash, V. (2002) Structure of Shock Waves in Layered Heterogeneous Material Systems: Experimental Results. Proceedings of the Second International Conference on Structural Stability and Dynamics, Editors: C. M. Wang, G. R. Liu, K. K. Ang, Singapore December 16-18, 2002, pp. 1040-1045.

Tsai, L. and Prakash, V. (2002). Structure of Shock Waves in Layered Heterogeneous Material Systems: Analytical Results. Proceedings of the Second International Conference on Structural Stability and Dynamics, Editors: C. M. Wang, G. R. Liu, K. K. Ang, Singapore December 16-18, 2002, pp. 1034-1039.

Tsai, L. and Prakash, V. (2002). Structure of Pressure-shear Waves in Layered Materials Systems. Proceedings of Society of Experimental Mechanics, Milwaukee, WI, Paper No. 188.

Tsai, L. and Prakash, V. (2002), Structure of Shock Waves in Layered Heterogeneous Material Systems, Modeling the performance of Engineering Structural Materials III, Editors: T. S. Srivatsan, D. R. Lesuer, E. M. Taleef, TMS, Columbus, OH, pp. 41-60.

Number of Papers published in non peer-reviewed journals: 8.00

(c) Papers presented at meetings, but not published in conference proceedings (N/A for none)

Number of Papers not Published: 0.00

(d) Manuscripts

Structure of shock waves in S2-glass fiber reinforced composites. Liren tsai and Vikas Prakash.

Spall strength of s2-glass fiber reinforced composites under both compression and shear. Liren Tsai and Vikas Prakash.

Dispersion and attenuation of shock ewaves in GRP. Liren Tsai and Vikas prakash

Number of Manuscripts: 3.00

Number of Inventions:

Graduate Students

<u>NAME</u>	<u>PERCENT_SUPPORTED</u>
FTE Equivalent:	
Total Number:	

Names of Post Doctorates

<u>NAME</u>	<u>PERCENT_SUPPORTED</u>
FTE Equivalent:	
Total Number:	

Names of Faculty Supported

<u>NAME</u>	<u>PERCENT_SUPPORTED</u>
FTE Equivalent:	
Total Number:	

Names of Under Graduate students supported

<u>NAME</u>	<u>PERCENT_SUPPORTED</u>
FTE Equivalent:	
Total Number:	

Names of Personnel receiving masters degrees

<u>NAME</u>
Total Number:

Names of personnel receiving PHDs

<u>NAME</u>
Total Number:

Names of other research staff

NAME

PERCENT_SUPPORTED

FTE Equivalent:

Total Number:

Sub Contractors (DD882)

Inventions (DD882)

Chapter 1

INTRODUCTION

1.1 Background

World War II ballistic threats and multifunctional survivability requirements coupled with a U.S. strategy of “forward-presence” of ground-based forces have encouraged the evolution of ground fighting vehicles to their present 70+ ton status (Fink, 2000). However, global political dynamics and a return of public sentiment for a stronger U.S. role in global peace-keeping have made the ability to fast deploy ground forces around the world essential for future U.S. Army strategy, tactics, and weaponry development. Therefore, several programs have been proposed by U.S. military to decrease the weight of combat vehicles. In particular, in the late 1980's, polymer-matrix composites (PMCs) were considered to be the prime candidates to replace the aluminum hull in the Bradley Infantry Fighting Vehicle, and also for the Composite Armored Vehicle (CAV) program in the mid-1990s. In 2003, a joint U.S. military Future Combat Systems (FCS) program was initiated in an effort to develop combat vehicles at a fraction of the weight of current vehicles yet as lethal and survivable.

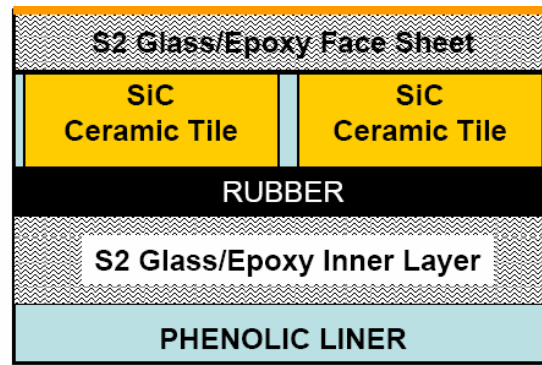
Lightweight PMCs are attractive choices for future combat vehicle armor applications, as they possess some clear advantages over more conventional monolithic materials, such as high specific modulus (E/ρ) and high specific strength (σ_{ult}/ρ) in the direction of their reinforcement (Kaw, 1997). However, the current progress in Composite Integral Armor (CIA) still falls short of Army's requirements for ballistic and shock resistance.

In view of the current lack of understanding of the shock response of the individual constituents of the composite integral armor system, a combined analytical-experimental investigation on S2-glass fiber-reinforced polymer composite (GRP) was conducted. The objective of this study is to understand the response of GRP under various shock loading conditions. Due to the complex architecture of the GRP, when shock waves propagate through it, the waves reflect, interact, and refract at the material interfaces. As a result, the shock front attenuation and late time dispersion at different thickness became an interesting topic to study. Also, utilizing various plate-impact configurations with appropriate shock compression conditions, the equation of state (EOS) and the spall strength of GRP can be determined. With this information, one can better understand and better characterize the dynamic behavior of glass fiber

reinforced polymer composites.

1.2 Composite Integral Armor (CIA)

Under the U.S. Army's Composite Armor Vehicles (CAV) program and the Future Combat Systems (FCS) program, various composite material systems have been investigated to understand and optimize the performance of potential Composite Integral armor (CIA) systems (Betheney, 1998; Vaidya, 1999). These composites generally comprise of several layers that contribute to specific functions, e.g. ballistic resistance, shock resistance, structure stability, etc. An example of CIA is illustrated in **Error! Reference source not found..** The cross-section view of this particular CIA demonstrates the arrangement of the constituents. In this architecture, the ceramic tile absorbs most of the kinetic energy of the incident projectile, while the rubber layer improves multi-hit ballistic performance (by shock-wave attenuation) and it also enables damage isolation to single ceramic tile. The S2-Glass/Epoxy layers in this structure not only provides structural stability and ballistic resistance, but also prevents bending failure of the ceramic tiles during low velocity impact. The phenolic liner at the bottom of the composite provides spall reduction, and fire, smoke, and toxicity protection (Gama, 2001).



Armor Cross-Section

Figure 1.1: Cross-section of an example of composite integral armor system.

From the Composite Integral Armor example above, it is clear that a successful design of a high performance and cost effective composite integral armor system is not an easy task; this is in particular because of the wide range of materials that are available for choice and the various design considerations such as ballistic and shock resistance, structural stability and damage tolerance, fire resistance, manufacturing procedure, and cost effectiveness. To narrow down design choices, and thus save money and time, computer simulations can be used to accurately evaluate the new composite integral armor system's performance before putting it through the actual test and manufacturing process. However, these computer simulations require detailed understanding of the dynamic behavior of the constituent materials comprising the Composite Integral Armor under intense shock wave loading conditions and states of stress such as those

considered in the present work.

1.3 S2 Glass Fiber Reinforced Polymer Composites

Historical examples of composites are abundant in the literature. Significant examples include the use of reinforcement bamboo shoots in mud walls for houses, glued laminated wood by Egyptians in 1500 BC, and laminated metals in forging swords in 1800 AD (Kaw, 1997). In the 20th century, modern composites were used in the 1930s with glass fiber reinforced resins. In general, long fibers in various forms are inherently much stiffer and stronger than the same material in bulk form. Ordinary plate glass fractures at stresses of only a few tens of MPa, yet glass fibers, in commercially available forms, have strengths of 3 to 5GPa and about 7GPa in laboratory prepared forms. The paradox of a fiber having different properties from bulk is due to the more perfect structure of a fiber. The crystals are aligned in the fiber along the fiber axis. Moreover, there are fewer internal defects in fibers than in bulk material (Jones, 1999). Because of its light weight and high strength, glass fiber has long been adopted intensively in composite manufacturing in several applications. In order to take advantage of its directional properties, glass fibers are also woven into layers to enhance its overall performance as the S2-glass fibers in S2 Glass Fiber Reinforced Polymer Composites.

S2 fiberglass was developed by Owens-Corning in 1960s as a bridge to the gap between E fiberglass and S fiberglass (John R. Sweet Co website). E fiberglass is the common all purpose fiberglass, in which “E” stands for electrical because it was originally used in electrical applications. S fiberglass, in which “S” stands for higher-strength, is stronger and stiffer than E fiberglass and more expensive. And there is also C fiberglass which was developed to resist chemicals, mostly acid, which destroy the E fiberglass (www.laborlawtalk.com). S fiberglass was developed for military applications, but it is extremely expensive due to the strict testing and certification requirements for military usage. S2 fiberglass is slightly less strong compared to S fiberglass but still provides 40% higher tensile strength, 10 to 20% higher compressive strength, and greater abrasion resistance than E fiberglass.

S2-glass fiber reinforced polymer composite (GRP) is one of the major components in Composite Integral Armor (CIA) systems. As mentioned before, it provides not only the lightweight structure stability but also serves an important role in shock resistance. However, its architecture is the most complex among all the constituents in CIA and most difficult to study. The

GRP specimens used in the present research were fabricated by Mr. Elias J. Rigas, Composites Development Branch, US army Research Laboratory, Watertown, MA, USA. They were made from S2-glass woven roving in CYCOM 4102 polyester resin matrix with 32% resin content by weight (Dandekar *et al.*, 2003). “Woven Roving” is made from continuous glass fiber roving which are interlaced into heavy weight fabrics, used in most cases to increase the flexural and impact strength of laminates, an example is shown in Figure 1.2.

The main reasons for epoxy being used as the polymer matrix material are (a) its relatively high strength; (b) its low viscosity and low flow rates, which allows good wetting of fibers and prevents their misalignment during processing; (c) its low volatility during cure and low shrink rate which reduces the tendency of the build-up of large shear stresses at the bond between the epoxy and its reinforcement; and (d) its availability in more than 20 grades to meet specific property and processing requirements (Jones, 1999). Figure 1.3 shows a layer of the S2 glass fiber woven roving of a GRP specimen used in the present research. As shown, each fiberglass bundle is approximately 5mm in width and 0.68mm in thickness.

The GRP studied in the present study was manufactured by stacking desired number of the S2 glass fiber woven roving in $\pm 90^\circ$ sequences. The glass fiber layers were stacked between two smooth steel plates with release film. The stacked layers were then vacuum bagged and undergone the following heat cycle:

- (1) Initially heated to 339 ± 4 K for 45 minutes.
- (2) Temperature raised to 353 ± 2 K for 2 hours.
- (3) Temperature raised to 398 ± 4 K and held for 2 hours.
- (4) Cooled to 312 ± 12 K at the rate of 7 K per minute.

The curing cycle starts with a gradual temperature increase under vacuum conditions so that the volatile gases including the water (vapor) can be driven off. Next, the temperature is gradually increased to the maximum curing temperature, which is held for a couple of hours to develop a high degree of cross-linking, followed by application of pressure to consolidate the laminate (Jones, 1999).

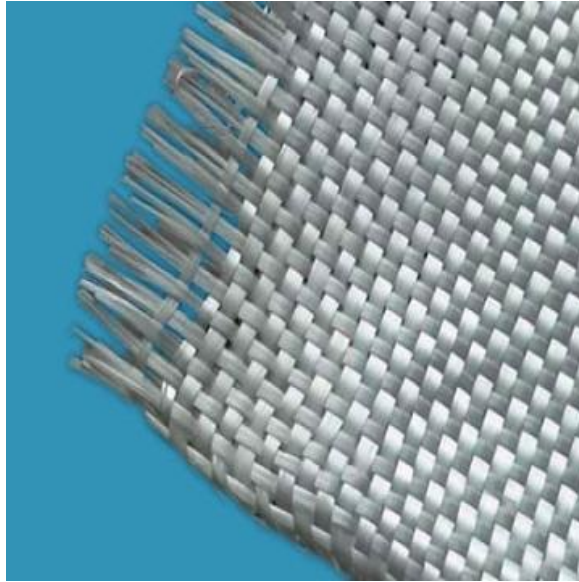


Figure 1.2: Fiberglass Woven Roving.

(Source:http://drywallmesh.en.alibaba.com/product/50025829/50062475/Fiberglass_Woven_Roving/Fiberglass_Woven_Roving/showimg.html)

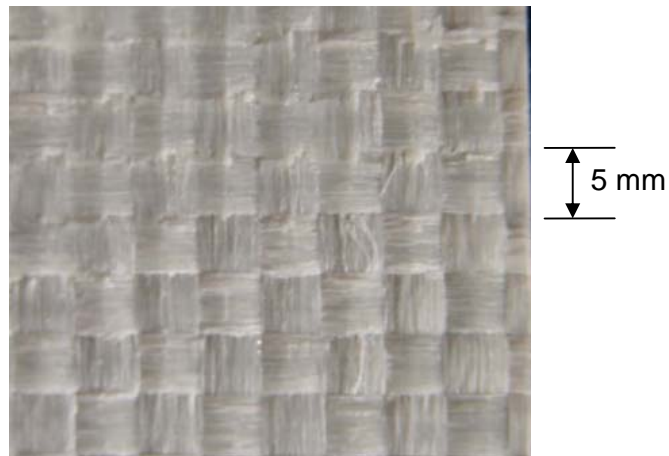


Figure 1.3: A S2 Glass Fiber woven roving layer of GRP tested in this research.

The density of the GRP was $1.959 \pm 0.043 \text{ Kg/m}^3$, with a longitudinal wave

speed 3.2 ± 0.1 km/s and bulk wave speed 2.6 km/s (Dandekar *et al.*, 1998).

The six independent elastic constants and elastic compliances of the tetragonal symmetry stiffness matrix are shown in **Error! Reference source not found.:**

Elastic Constants	GPa	Elastic Compliances	10^{-2}GPa^{-1}
C11	31.55 ± 3.8	S11	4.5039 ± 1.2
C33	20.12 ± 0.40	S33	6.2074 ± 1.28
C44	4.63 ± 1.22	S44	21.60 ± 5.6
C66	4.94 ± 1.31	S66	20.24 ± 5.4
C12	15.86 ± 4.53	S12	-1.8696 ± 0.82
C13	9.75 ± 3.83	S13	-1.2766 ± 0.77

Table 1.1: Values of elastic constants and elastic compliances.

Where, the stiffness matrix [C] is given by

$$[C] = \begin{bmatrix} C_{11} & C_{12} & C_{13} & 0 & 0 & 0 \\ C_{12} & C_{22} & C_{23} & 0 & 0 & 0 \\ C_{13} & C_{23} & C_{33} & 0 & 0 & 0 \\ 0 & 0 & 0 & C_{44} & 0 & 0 \\ 0 & 0 & 0 & 0 & C_{55} & 0 \\ 0 & 0 & 0 & 0 & 0 & C_{66} \end{bmatrix},$$

where $C_{22} = C_{11}$, $C_{23} = C_{13}$, and $C_{55} = C_{44}$.

1.4 Dynamic Response of Glass Fiber Reinforced Composites

Dynamic response of materials is important in a variety of engineering applications. Some of the more common examples include debris and bird strike to the jet engine blades; particle impact on vehicle window; or wave propagation in porous media used in seismological studies. In applications of interest to the military, impact, explosive detonation, and high strain rate deformations occur in numerous situations (Meyers, 1994). Many forms of high velocity projectiles can challenge the defensive structures on the battle field, e.g., shaped charges, explosively forged projectiles, or a kinetic energy penetrator. Careful structural design taking the dynamic material response into account has the potential to prevent catastrophic failure and save lives. The study of the dynamic response of materials has not been the focus until early 20th century when Hopkinson (1905) and Mason (1934) studied tensile pulse effects on wires. In 1937, Ginns carried

out one of the first research works attempted to record a dynamic stress-strain curve. Since that time investigations of material properties under dynamic loading have become widespread and relatively routine. Materials under high strain rates have shown to exhibit mechanical properties that are quite different from those measured under static or quasi-static loading conditions. Although glass-fiber reinforced resins were introduced in the 1930s, the dynamic response of these materials was not the focus until the 1970s when drop weight testing machine with strain gauges were utilized to test the impact strength of glass-fiber reinforced composites. Tensile strength and failure modes of unidirectional and angle ply E-glass fiber reinforced epoxy matrix polymer composites were studied (Lifshitz *et al.* 1976; Rotem *et al.*, 1973; Broutman *et al.*, 1973). Failure stresses were found to be considerably higher than those obtained from quasi-static test results. The drop weight test machines produced strain rates between $0.1 \sim 200 \text{ s}^{-1}$; the drop weight machines provided a quick and inexpensive facility but did not necessarily take wave propagation in the specimen into consideration.

Unlike the drop weight test machine, the Split Hopkinson Pressure Bar (SHPB) apparatus has proved to be a reliable and an accurate technique (O'toole, 2003).

Developed by Kolsky in 1949, the SHPB has become the standard to test materials at strain rates between $200 \sim 10,000 \text{ s}^{-1}$. In recent years many attempts have been made to examine the dynamic response of glass-fiber reinforced composites utilizing the SHPB (or Kolsky bar) technique to study strain rate effects in glass-fiber reinforced composites under relatively simple states of stress, such as uniaxial compression, uniaxial tension, and pure shear (Agbossou *et al.* 1995; Barre *et al.*, 1996; El-Habak ,1991; Gama *et al.*, 2001; Harding, 1993; Tay *et al.*, 1995; Vural *et al.*, 2004). The failure and ultimate strength of the composites were both reported to increase with strain rate. Haque *et al.* (2003) used SHPB technique to study the thermal and mechanical properties of S2 glass/epoxy/nanoclay polymer composite. In nanoclay reinforced composites, by dispersing 1% nanosilicates by weight increased the inter-laminar shear strength, bending strength and fracture toughness, by almost 44%, 24%, and 23%, respectively. It also exhibited a $\sim 26^{\circ}\text{C}$ higher decomposition temperature.

To test the material's dynamic response at strain rate above $10,000 \text{ s}^{-1}$, plate impact or direct contact explosives methodologies have been employed in the past to produce shock waves up to tens of GPa. A shock is a discontinuity of stress, temperature (or internal energy) and density (Meyers, 1994). When a

shock wave travels through a material, the composition of the material can undergo substantial transformation, especially when the amplitude of the shock wave exceeds the dynamic flow strength of the material. In 1958, Rice *et al.* published the first comprehensive description of theory and properties of materials subjected to very high ($>10\text{GPa}$) pressures. Since the mid-1960s considerable interest has developed concerning the response of solids at stresses from about 0.1 to 10GPa. Applications within this stress range involve metal forming, material strengthening, structure design, material damage, gauge design, etc. (Graham *et al.*, 1978). Gas guns were developed during the 1960s to propel planar impactors to pre-selected velocities so that samples could be subjected to well control loading (Hughes *et al.*, 1957; Graham, 1960; Lundergan, 1960). These planar projectile impact experiments have become the most widely used methods for shock loading. These experiments allow impact stresses to be virtually continuous, provide precisely defined loading conditions, and are also compatible with other laboratory experimentation.

Even though, by using the gas-gun, considerable progress has been made over the years on the experimental front, the propagation of acceleration and shock waves in heterogeneous material systems, including the phenomenon of material

and geometric dispersion continues to be poorly understood. Moreover, over the years, the number of plate impact experiments conducted on glass-fiber reinforced composites when compared to SHPB experiments, is relatively small. Zhuk *et al.* (1994) studied the shock compressibility and sound wave velocity in commercial plain-weave fiber-glass KAST-V (Soviet standard 102-92-74) composites using manganin gauges in the range of 5 GPa \sim 22 GPa. They also utilized the Valyn's Velocity Interferometer system for Any Reflector (VISAR) to monitor the free surface particle velocity in experiments conducted at stress levels between 0.8~1.2 GPa. No spall signal was observed in their experiments. Hydrodynamic shock front attenuation was observed for the experiments impacted by thin (\sim 1.3 mm) aluminum flyer plate. In these experiments, strong shock front dispersion was also reported. Zaretsky *et al.* (1997) also conducted plate impact experiments on commercial KAST-V for stress range between 0.3 GPa \sim 0.8 GPa using the VISAR. Spall signal was observed in the experiments with a shock stress of about 0.3 GPa, and the spall strength of KAST-V was estimated to be about 0.1 GPa. The EOS of KAST-V was also determined, and the shear strength was determined to be about 0.28 GPa. They proposed that the matrix-filler interfaces control the behavior of the material in compression. Zaretsky *et al.* (2004), later perform plate impact experiments on laminated

glass-fiber reinforced epoxy 7781 composite. The free surface velocities were recorded by the VISAR in the stress range of 0.5 ~ 2.4 GPa. The spall strength was calculated to be about 0.16 GPa. The dynamic viscosity was found to be much larger than the component epoxy material. Oscillation in the free surface particle velocity profile was observed, and the frequency of the oscillation was found to increase with increasing impact stress.

Plate impact experiments on S2-glass fiber reinforced polymer composite (GRP) have been conducted by several researchers in United States in the past several years. Dandekar *et al.* (1998) at Army Research Laboratory studied the elastic constants and spall strength of GRP. They utilized ultrasonic wave velocity measurements along the six axes of the GRP to calculate the six independent elastic constants for its tetragonal stiffness matrix. The measured spall strength was between 0.007 GPa ~ 0.06 GPa. On the same material, Boteler *et al.* (1999) at Sandia National Laboratory carried out a series of experiments using embedded polyvinylidene fluoride (PVDF) stress-rate gauges to study the shock wave profiles in GRP as a function of propagation distance. The experimental stress histories displayed shock wave attenuation with the increasing propagation distance. In the same year, Trott *et al.* (1999) at Sandia National

Laboratories applied a novel line-imaging velocity interferometer in order to simultaneously record the shock response of GRP at various points. The systematic difference in shock arrival time over a transverse distance of 2 mm and high amplitude fluctuations in the wave profile reflect the complex periodic geometry of GRP. Later on, Dandekar (2003) studied the shock response of GRP via a joint research program with Hall *et al.* at Sandia National Laboratory in an effort to present the first wide-stress-range systematic research on this material. The Equation of State for GRP was determined by Dandekar *et al.* (2003) from series of shock-resock and plate-reverberation experiments. The non-linear effects due to material heterogeneity can be ascribed to impedance (and geometric) mismatch present at various length scales, apart from material nonlinearities arising from material inelasticity effects, void nucleation and growth, and delamination.

Simulation works for fiber reinforced composites have been conducted by some researchers. Tsou *et al.* (1969) studied the shock wave propagation in unidirectional fiber reinforced composite along the fiber direction. The interface shear and heat transfer was estimated. Chen X. (2003), deBotton *et al.* (2004) and Espinosa *et al.* (2000) all performed shock simulation on plan woven glass

fiber reinforce composites. The fluctuation of particle velocity profiles were predicted because of the wave reverberation between material interfaces. The oscillation profile of late time solution was found difficultly to accommodate to the experiment data due to the complex structure of GRP.

S2-glass fiber reinforced polymer composite (GRP) is a very important component in Composite Integral Armor (CIA) systems. Although its elastic constants, Equation of State (EOS), spall strength and complex wave profiles have been studied by Dandekar *et al.* (1998), Dandekar and Hall *et al.* (2003), Boteler *et al.* (1999) and Trott *et al.* (1999), its Equation of State in the important lower stress range has been poorly documented, and only a few experiments have been conducted (six in all) to determine the spall strength.

In view of the importance to better understand the shock response of GRP, a combined analytical and experimental research has been conducted at the Case Western Reserve University. Analytical approach was carried out by applying asymptotic techniques to analyze propagation of acceleration waves in 2-D elastic/elastic and elastic/visco-elastic layered material systems. Both wave-front and late-time solutions for step-pulse loading on layered half-space

were compared with the plate impact experimental profiles on metal/metal and metal/polymer bilaminates. The effect of layer density, propagation distance, and material inelasticity were studied. These results explained the fluctuation of particle velocity profiles in GRP shock experiments. Numerous normal shock compression experiments were then performed on GRP specimens at compression stresses between 0.04 ~ 2.6 GPa in an effort to intensively and systematically fulfill the lack of EOS data in the previous researches. The spall strengths of GRP were also determined through both normal impact and combined pressure shear spall experiments at several different impact angles. A 3-D surface fit was generated to visualize the effect of normal compression stresses and shear stresses to the observed spall strength. Shock-resock and shock-release experiments were also performed to estimate the shear strengths of GRP under compression stress. The Hugoniot curve of GRP was also determined. These experiment configurations, designs, and experimental data calculations were all detailed in the following chapters.

1.5 Report Outline

Composite material systems have unique characteristic under shock loading such as scattering, dispersion and attenuation which play critical roles in determining the thermo-mechanical response of the composite. These phenomena can be

ascribed to a number of nonlinearities in the material such as wave characteristics, loading conditions, and material heterogeneity (measured at various spatial scales ranging from nanometers to a few millimeters). To understand the shock response in GRP, it is essential to first understand the role of material heterogeneity (its layered architecture) and the in-elasticity of its constituent materials (fiberglass woven roving and polyester resin matrix). In the present study, computer simulations, Chapter 2, and gas-gun plate impact experiments, Chapter 3, are performed on selected metal/metal and metal/polymer bi-laminates to understand the effect of layered architecture (both layer thickness and layer density) and material in-elasticity to the attenuation of shock front and dispersion of late time wave profiles.

In Chapter 4, the structure of shock-induced compression wave as a function of impact velocity, structure of shock-induced compression wave as a function of propagation distance, the HEL of the composite, its dynamic stress versus strain behavior, the various Hugoniot States (EOS), and the Hugoniot stress vs. strain curves are presented in an effort to better understand the dynamic response of the S2-glass fiber reinforced polymer composites.

In Chapter 5, the spall strength of GRP as a function of various levels of dynamic compression as well as after combined pressure and shear loading was studied. A computer simulated surface match was also determined to illustrate the effects of the presence of shear strain and normal stress on the spall strength of GRP.

In Chapter 6, the dynamic yield strength (critical strength) of the GRP was determined. Shock-resock and shock-release experiments were performed on GRP to estimate the residual shear strength of the GRP under various level of shock compression. The Results and Discussion are summarized in Chapter 7.

REFERENCES

- Agbossou A., Cohen I., and Muller D., 1995. "Effects of Interphase and Impact Strain Rates on Tensile Off-Axis Behaviour of Unidirectional Glass Fibre Composite: Experimental Results." *Engineering Fracture Mechanics*, 52(5), 923-934.
- Barker L. M. and Hollenbach R. E., 1970. "Shock-Wave Studies of PMMA, Fused Silica, and Sapphire", *Journal of Applied Physics*, 41(10), 4208-4226.
- Barker L. M., 1971. "A Model for Stress Wave Propagation in Composite Materials", *Journal of Composite Materials*, 5, 140-162.
- Barker L. M., Lundergan C. D., Chen P. J., Gurtin M. E., 1974. "Nonlinear Viscoelasticity and the Evolution of Stress Waves in Laminated Composites: A Comparison of Theory and Experiment", *Journal of Applied Mechanics*, 1025-1030.
- Barre S., Chotard T., and Benzeggagh M. L., 1996. "Comparative Study of Strain Rate Effects on Mechanical Properties of Glass Fibre-Reinforced Thermoset Matrix Composites", *Composites Part A*, 27A, 1169-1181.
- Betheney W., DeLuca E., Prifti J. and Chou S. C., 1998. Ballistic impact damage of S2-glass reinforced plastic structural armor. *Composites Science and Technology* 58, 1453-1461
- Boteler J. M., Rajendran A. M., Grove D., 1999. "Shock Wave Profiles in Polymer Matrix Composite", *Shock Compression of Condensed Matter - 1999*. ed: M. D. Furnish, L. C. Chhabildas and R. S. Hixson, American Institute of Physics, 563-566.
- Chen X., 2003. Micromechanics based modeling of high velocity impact response of layered heterogeneous material systems. Mechanical Engineering, Department, Florida State University.
- Dandekar D. P., Boteler J. M., and Beaulieu P. A., 1998. "Elastic Constants and Delamination Strength of a Glass-Fiber-Reinforced Polymer Composite",

Composite Science and Technology, 58, 1397-1403.

Dandekar D. P., Hall C. A., Chhabildas L. C., Reinhart W. D., 2003. "Shock Response of a Glass-Fiber-Reinforced Polymer Composite", Composite Structures, 61, 51-59.

deBotton G. and Tevet-Deree L., 2004. "The Response of a Fiber-Reinforced Composite with a Viscoelastic Matrix Phase", Journal of Composite Materials, 38(14), 1255-1277.

El-Habak A. M. A., 1991. "Mechanical Behavior of Woven Glass Fiber-Reinforced Composites under Impact Compression Load", Composites, 22(2), 129-141.

Espinosa H. D., Dwivedi S., and Lu H.-C., 2000. "Modeling Impact Induced Delamination of Woven Fiber Reinforced Composites with Contact/Cohesive Laws", Computer Methods in Applied Mechanics and Engineering, 183, 259-290.

Fink B. K., 2000. "Performance Metrics for Composite Integral Armor", Journal of Thermoplastic Composite Materials, 13, 417-431.

Gama B. A., Gillespie J. W., et al., 2001. "High Strain-Rate Behavior of Plain-Weave S-2 Glass/Vinyl Ester Composites", Journal of Composite Materials, 35(13), 1201-1228.

Graham R. A. and Asay J. R., 1978. "Measurement of wave profiles in shock loaded solids", High Temperatures - High Pressures, 10, 355-390.

Haque A., Shamsuzzoha M., Hussain F., and Dean D., 2003. "S2-Glass/Epoxy Polymer Nanocomposites: Manufacturing, Structures, Thermal and Mechanical Properties", Journal of Composite Materials, 37(20), 1821-1837.

Holmes B. S. and Tsou F. K., 1972. "Steady Shock Waves in Composite Materials", Journal of Applied Physics, 43(3), 957-961.

Jones R. M., 1999. Mechanics of Composite Materials, Taylor & Francis, Philadelphia.

Kaw A. K., 1997. Mechanics of Composite Materials, CRC Press, New York.

Kolsky H., 1949. "An investigation of the mechanical properties of materials at very high rates of loading," Proceedings of the Royal Society, B62, 676-700.

Kubair D. V., 2004. "Simulation of Low-velocity Impact Damage in Layered Composites using a Cohesive-based Finite Element Technique," Defence Science Journal, 54(4), 571-578.

Li Z. and Lambros J., 2000. "Dynamic Thermomechanical Behavior of Fiber Reinforced Composites", Composites Part A, 31, 537-547.

Lifshitz J. M., 1976. "Impact Strength of Angle Ply Fiber Reinforced Materials", Journal of Composite Materials, 10, 92-101.

Lundergan C. D. and Drumheller D. S., 1971. "Propagation of Stress Waves in a Laminated Plate Composite", Journal of Applied Physics, 42(2), 669-675.

Meyers M. A., 1994. Dynamic Behavior of Materials. John Wiley & Sons, New York.

Munson D. E. and Schuler K. W., 1971. "Steady Wave Analysis of Wave Propagation in Laminates and Mechanical Mixtures", Journal of Composite Materials, 5, 286-304.

Munson D. E. and May R. P., 1972. "Dynamically Determined High-Pressure Compressibilities of Three Epoxy Resin Systems", Journal of Applied Physics, 43(3), 962-971.

Munson D. E., Boade R. R., and Schuler K. W., 1978. "Stress-Wave Propagation in Al₂O₃-Epoxy Mixtures", Journal of Applied Physics, 49(9), 4797-4807.

Oguni K., Tan C. Y., Ravichandran G., 2000. "Failure Mode Transition in Unidirectional E-Glass/Vinylester Composites under Multiaxial compression", *Journal of Composite Materials*, 34, 2081-2097.

O'toole B., 2003. "Identification of Dynamic Properties of Materials for the Nuclear Waste Package," Technical Report: DE-FC08-98NV12081, US DOE/UCCSN Cooperative Agent.

Oved Y., Luttwak G. E., and Rosenberg Z., 1978. "Shock Wave Propagation in Layered Composites", *Journal of Composite Materials*, 12, 84-96.

Rice M. H., McQueen R. G., Walsh J. M., 1958. "Compression of Solids by Strong Shock Waves," *Solid State Physics*, VI, Eds Seitz F., Turnbull D., Academic Press, New York, 1-63.

Schuler K. W., 1970. "Propagation of Steady Shock Waves in Polymethyl Methacrylate", *Journal of the Mechanics and Physics of Solids*, 18, 277-293.

Shazly M., 2004. "Dynamic Deformation and Failure of GAMMA-MET PX at Room and Elevated Temperatures", Dissertation, Case Western Reserve University, Cleveland, Ohio.

Sve C., 1972. "Stress Wave Attenuation in Composite Materials", *Journal of Applied Mechanics*, 1151-1152.

Tay T. E., Ang H. G., and Shim V. P. W., 1995. "An Empirical Strain Rate-Dependent Constitutive Relationship for Glass-Fibre Reinforced Epoxy and Pure Epoxy", *Composite Structures*, 33, 201-210.

Trott W. M., Knudson M. D., Chhabildas L. C., and Asay J. R., 1999. "Measurements of Spatially Resolved Velocity Variations in Shock Compressed Heterogeneous Materials Using a Line-Imaging Velocity Interferometer," *Shock Compression of Condensed Matter-1999*, edited by M. D. Furnish, L. C. Chhabildas, and R. S. Hixson, 993-998.

Tsou F. K. and P. C. Chou, 1969. "Analytical Study of Hugoniot in Unidirectional Fiber Reinforced Composites" , Journal of Composite Materials, 3, 500-514.

Vaidya U. K., Hosur M. V., Kumar P., Mahfuz H., Haque A. and Jeelani S., 1999. "Impact damage resistance of innovative functional sandwich composites", In: ASME 1999 Mechanics and Materials Conference Blacksburg, VA.

Vural M. and Ravichandran G., 2004. "Transverse Failure in Thick S2-Glass/Epoxy Fiber-reinforced Composites", Journal of Composite Materials, 38(7), 609-623.

Zaretsky E., Igra O., Zhuk A. Z., Lash A. A., 1997. "Deformation Modes in Fiberglass under Weak Impact", Journal of Reinforced Plastics and Composites, 16, 321-331.

Zaretsky E., deBotton G., and Perl M., 2004. " The Response of a Glass Fibers Reinforced Epoxy Composite to an Impact Loading", International Journal of Solids and Structures, 41, 569-584.

Zhuang S., 2002. Shock Wave Propagation in Periodically Layered Composites, California Institute of Technology.

Zhuk A. Z., Kanel G. I., and Lash A. A., 1994. "Glass-Epoxy Composite Behaviour under Shock Loading", Journal de Physique IV, C8-403~C8-407.

Chapter 2

ASYMPTOTIC SOLUTION OF WEAK SHOCK WAVES IN 2-D LAYERED HETEROGENEOUS MATERIAL SYSTEMS

2.1 Introduction

Shock wave propagation in heterogeneous material systems is a complex matter.

Even though some progress has been made to understand the propagation of acceleration waves in heterogeneous material systems, the phenomenon of material and geometric dispersion continues to be poorly understood. Shock waves in the absence of phase transitions are understood to have a one-wave structure in most homogeneous materials. However, upon loading of a bi-laminate, a two-wave structure is obtained -- a leading shock front followed by a complex pattern that varies with time. This complex pattern is generated by a continuous interaction of compression and rarefaction waves due to the presence of inter-laminar interfaces.

Expressions for pressure and particle-velocity, based on the consideration of head-wave interaction with interfaces in linear elastic bilaminates, under weak shock wave loading have been obtained by Laptev and Trishin (1976). It was found that the attenuation of shock-pressure and particle-velocity is primarily determined by the ratio of acoustic impedance of the layers, and by the size of the periodic structure of the bilaminates (cell size). Smaller the cell size, the greater is the number of interfaces that interact with the propagating stress waves, and higher is the attenuation and dispersion. Analytical studies of wave dispersion relations for an infinite train of time-harmonic acceleration waves propagating in layered material systems have been conducted in a variety of elastic composites. Sun *et al.* (1968) studied the case of waves in elastic bilaminates (i.e. composites consisting of alternating plane layers of different linear elastic materials) propagating in directions parallel or perpendicular to the laminates. These exact dispersion relations have been compared by Hegemier (1972) to those obtained from various approximate theories. For viscoelastic bilaminates the understanding of dispersion relations is less complete. Stern,

Bedford, and Yew (1970) have considered wave propagation in a direction parallel to the laminates for alternating layers of elastic and viscoelastic materials. They simplified the analysis by neglecting the transverse displacement in the viscoelastic layers and the variation of the longitudinal displacement across the thickness of the elastic layers. Clifton (1972) considered the exact theory of time-harmonic waves propagating in the direction of the normal to the laminates for general linear viscoelastic bilaminates. The dispersion relations obtained were similar to those obtained by Sve (1961) for the closely related case of thermo-elastic waves in laminates. Transient solutions for the case of step loading applied uniformly over the surface of a half space consisting of alternating plane layers of elastic materials have been obtained by Peck and Gurtman (1969) and by Sve (1972) who considered, respectively, waves propagating parallel and perpendicular to the layers. In both these cases late-time asymptotic solutions were obtained which show the dispersive character of the main part of the wave. Sve (1972) also considered, in an approximate way, the late-time solution for

viscoelastic bilaminates in which the waves are propagating in the direction perpendicular to the laminates.

To date, only a limited number of experiments have been carried out that concern the finite amplitude wave propagation in composite materials for the loading stress in the intermediate regime. Barker *et al.* (1974) performed experiments on periodic laminates and found that below certain critical input amplitude, the stress wave amplitude decayed exponentially with distance and formed a structured shock wave above the critical amplitude. Lundergan and Drumhellar (1971) and Oved *et al.* (1978) also conducted limited shock wave experiments on layered stacks, which showed resonance phenomena due to layering. Nesterenko *et al.* (1983; 1984) observed an anomaly in the precursor decay for the case of propagation of strong shock waves in periodic bilaminates with a relatively small cell size. They noted that for bilaminates with a relatively small cell size the jump in particle velocity at the wave front is essentially higher than one obtained with the larger cell size at the same distance of propagation.

Similar observations were made for Ti-Al layered material systems under strong shock wave loading (Benson and Nesterenko, 2001). Comparison of the experimental results and computer simulations indicated that this effect is primarily due to the interactions of the secondary compression waves with the leading shock front. At early times, these secondary compression waves trail the shock front. However, with increasing distance of propagation these waves catch-up and eventually overtake the leading shock-wave front from behind. This increase in wave speed is facilitated by the propagation of the trailing secondary waves in a previously compressed material state. More recently Zhuang (2002) have conducted normal plate-impact experiments on layered stacks of polycarbonate and either glass, stainless steel or aluminum systems to investigate dispersion versus dissipation characteristics due to heterogeneity of the layered material system during propagation of strong shock waves. They also reviewed existing models for propagation of shock waves and proposed new scaling laws for shock viscosity of heterogeneous layered solids.

In view of the scientific and technological importance of heterogeneous materials in shock related applications and our current incomplete state of understanding of their performance under impact loading conditions, integrated experimental-analytical research is being conducted. The focus is to better understand wave scattering and dispersion at material interfaces and the role of material inelasticity in determining the structure of shocks during shock compression in heterogeneous material systems. The analytical works are included in this chapter while the experimental works are discussed in the following chapter.

2.2 WAVE PROPAGATION IN ELASTIC-VISCOELASTIC BILAMINATES

Consider bilaminates consisting of elastic and viscoelastic layers of uniform thickness and infinite lateral extent. The elastic layers occupy odd numbered layers, i.e. $n = 1, 3, 5, \dots$, and the viscoelastic layers occupy even numbered layers, i.e. $n = 2, 4, 6, \dots$. Consider the individual layers to be homogeneous and isotropic and the layer thickness of both constituents to be the same, i.e. $L_1 = L_2 = 0.5d$,

where L_1 and L_2 are the thickness of the elastic and viscoelastic layers, respectively, and d is the total thickness of a typical bilaminate.

Let the laminates be subjected to a time dependent normal stress loading which is applied uniformly over the plane $x = 0$ (see Figure 2.1). Under these conditions longitudinal wave of one-dimensional strain propagate in the direction normal to the laminates. We consider the case in which the applied loading has a step function time dependence, i.e. $\sigma = -\sigma_o H(t)$, and seek asymptotic solutions for the wave at the wave-front and the waveform at late times.

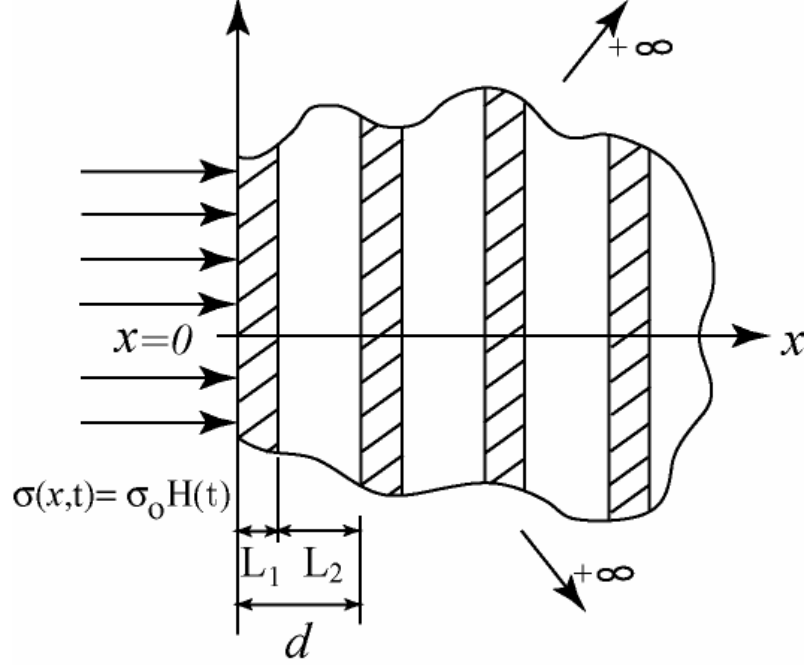


Figure 2.1: Schematic of the laminate used in the analytical analysis.

For infinitesimal deformation longitudinal waves propagating in the x-direction are governed by the balance of linear momentum and continuity. For the elastic layers these equations can be written as

$$\rho_1 \frac{\partial u_1}{\partial t}(x,t) - \frac{\partial \sigma_1}{\partial x}(x,t) = 0 \quad \text{and} \quad \frac{\partial \varepsilon_1}{\partial t}(x,t) = \frac{\partial u_1}{\partial x}(x,t). \quad (2.1)$$

For viscoelastic layers the balance of linear momentum and the continuity equations can be written as

$$\rho_2 \frac{\partial u_2}{\partial t}(x,t) - \frac{\partial \sigma_2}{\partial x}(x,t) = 0 \quad \text{and} \quad \frac{\partial \varepsilon_2}{\partial t}(x,t) = \frac{\partial u_2}{\partial x}(x,t). \quad (2.2)$$

The constitutive equations for elastic and viscoelastic layers can be expressed as

$$\sigma_1(x, t) = E \varepsilon_1(x, t) \text{ and } \sigma_2(x, t) = \int_{-\infty}^t G(t - \tau) d\varepsilon_2, \text{ respectively.} \quad (2.3)$$

In Eqs. (2.1) to (2.3), σ_1 and σ_2 are the longitudinal components of the stress in the elastic and viscoelastic layers; u_1 and u_2 are the longitudinal components of the particle velocities in the elastic and viscoelastic layers; ρ_1 and ρ_2 are the mass density of the elastic and the viscoelastic layers; ε_1 and ε_2 are the longitudinal components of the strain in the elastic and viscoelastic layers; and E and $G(t)$ represent the elastic and the viscoelastic modulus, respectively.

The relaxation function for the viscoelastic material behavior is assumed to be described by an exponential function of the type

$$G(t) = [G(0) - G(\infty)]e^{-t/\tau} + G(\infty), \quad (2.4)$$

where, $G(0)$ denotes the “glassy” modulus at $t = 0$; $G(\infty)$ denotes the “rubbery” modulus at $t = \infty$; and τ denotes the characteristic relaxation time.

We seek solution to Eqs. (2.1) to (2.3) which satisfy zero stress and zero particle-velocity initial conditions, and boundary conditions given by $\sigma(0, t) = -\sigma_0 H(t)$.

Solutions to such problems are obtained most conveniently by means of Laplace

Transform methods in which the Laplace transform, $\hat{f}(x, s)$, of a function $f(x, t)$

is defined by

$$\hat{f}(x, s) = \int_0^{\infty} f(x, t) e^{-st} dt. \quad (2.5)$$

Application of the Laplace transform to Eqs (2.1) to (2.3) yields a system of four

algebraic equations in the transformed plane. For a fixed s , these equations

represent ordinary differential equations in which the coefficients are periodic

functions of x with period $d = L_1 + L_2$. These equations contain four complex

constants associated with the solution for the longitudinal component of stress.

Two conditions on the four complex constants are obtained by requiring that the

particle velocity and stress be continuous across the interface between the two

adjacent layers comprising the bilaminate. The remaining conditions are

obtained by the application of Floquet theory for periodic structures (Chen and

Clifton, 1974). According to Floquet's theory, for such differential equations the solution at an arbitrary position x is related to the solution at $x - d$ by

$$\hat{w}(x, s) = e^{\mu(s)d} \hat{w}(x - d, s), \quad (2.6)$$

where, $\hat{w}(x, s)$ represents the solution vector for the particle velocity and stress and $\mu(s)$ is a characteristic parameter to be determined.

The characteristic parameter $\mu(s)$ in Eq. (2.6) can be obtained by solving the transcendental equation

$$\cosh \mu(s) d = \cosh \alpha_1(s) l_1 \cosh \alpha_2(s) l_2 + \frac{1}{2} \left(\frac{\rho_1 \alpha_1(s)}{\rho_2 \alpha_2(s)} + \frac{\rho_2 \alpha_2(s)}{\rho_1 \alpha_1(s)} \right) \sinh \alpha_1(s) l_1 \sinh \alpha_2(s) l_2 \quad (2.7)$$

where

$$\alpha_1(s) = \sqrt{\frac{s^2 \rho_1}{E}}, \text{ and } \alpha_2(s) = \sqrt{\frac{s \rho_2}{\hat{G}(s)}}. \quad (2.8)$$

Note that if μ is a solution of Eq (2.7), then $-\mu$ is also a solution. By considering wave propagation in the direction of increasing x , we can restrict our attention to roots for which $\text{Re } \mu(s) \leq 0$, so that the solution remains bounded

as $x \rightarrow \infty$. This requirement uniquely determines μ , except for added integer multiples of $2\pi i$ which do not affect the solution.

2.3 SOLUTION AT WAVEFRONT: ELASTIC PRECURSOR DECAY

Let the longitudinal wave-fronts propagate with speeds c_1 and c_2 in the elastic and the viscoelastic layers, respectively. An average wave speed for the longitudinal wave-fronts can be defined as

$$c_{Wave} = \frac{d}{(l_1/c_1 + l_2/c_2)} . \quad (2.9)$$

At the arrival of the longitudinal wave at $x = x_n$, where $x_n = (n/2)d$ is the distance from $x = 0$ to the interface between the n^{th} and the $(n+1)^{\text{th}}$ layers, the stress is given by

$$\sigma(x_n, x_n^+ / c_{Wave}) = -\sigma_0 \left\{ \exp \left[\frac{l_2 G'(0)}{2c_2 G(0)} \right] \right\}^{n/2} \theta^{-n/2} . \quad (2.10)$$

where,

$$\theta = \frac{1}{2} + \frac{1}{4} \left(\frac{\rho_2 c_2}{\rho_1 c_1} + \frac{\rho_1 c_1}{\rho_2 c_2} \right) . \quad (2.11)$$

For the case of elastic-elastic bilaminates the argument of the exponential function is zero and the RHS of Eq. (2.10) can be interpreted as an average transmission coefficient for propagation of an elastic wave through a cell of length d . The attenuation of the amplitude at the wave-front is the decay primarily due to successive elastic wave reflections. For the case of elastic-viscoelastic bilaminates the argument of the exponential function gives rise to additional attenuation due to material inelasticity. The rate of decrease in stress is often so rapid that the stress at the wave front can become negligibly small at remote positions.

Figure 2.2 shows the magnitude of the elastic precursor as a function of number of layers and the impedance mismatch. A strong decay in the elastic precursor is observed with an increase in the number of layers and/or the increase in impedance mismatch.

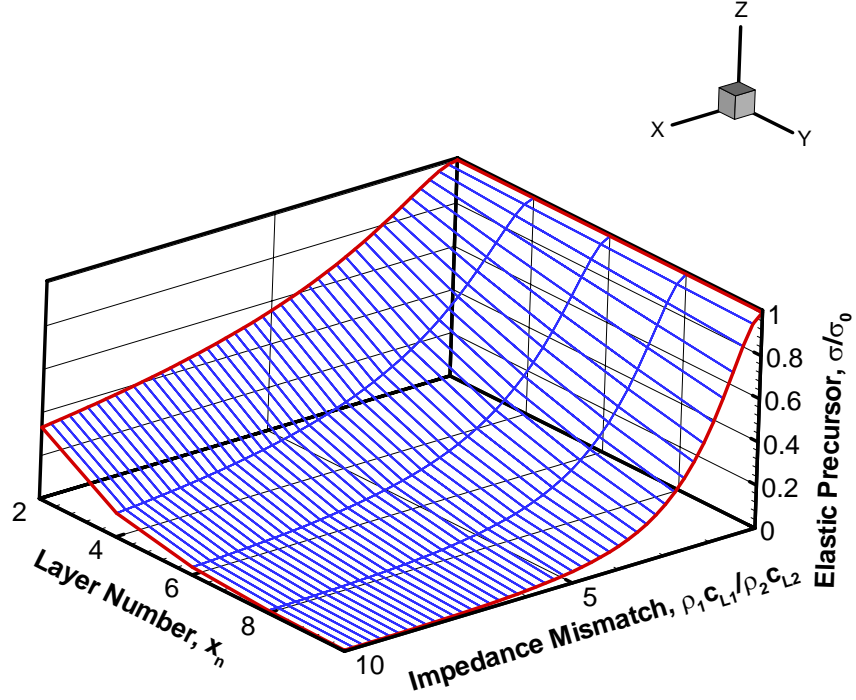


Figure 2.2: Effect of material mismatch and the number of layers on the elastic precursor decay for elastic-elastic bilaminates.

Figure 2.3 shows the effect of viscoelasticity on the elastic precursor decay after wave propagation through 10 layers. The stress at the wave front is normalized by the amplitude of the corresponding elastic precursor for the case of elastic-elastic bilaminates. The x-axis represents the ratio of the time taken for the longitudinal wave to travel the thickness of a viscoelastic layer to the relaxation time constant for the material. It is to be noted that when the relaxation time is

large and/or the viscoelastic layer thickness, i.e. L_2 is small, the effect of material inelasticity on elastic precursor decay is small. Also, when the ratio between the instantaneous modulus and the rubbery modulus, i.e. $\gamma^2 = G(0)/G(\infty)$, is close to one the effect of material inelasticity on the elastic precursor decay is negligible.

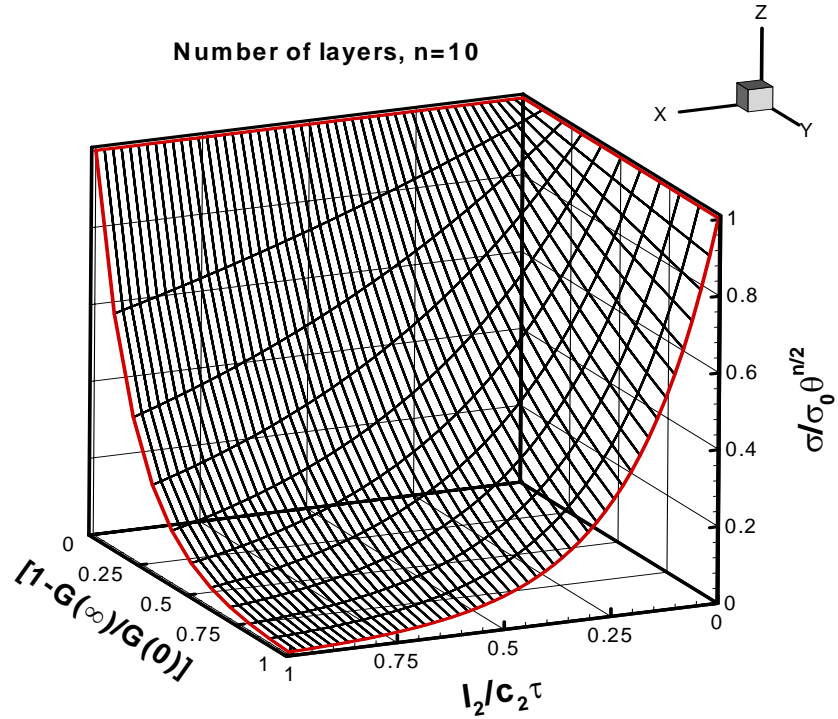


Figure 2.3: Effect of material inelasticity on the elastic precursor decay. The stress at the wave front (y-axis) is normalized by the amplitude of the elastic precursor for the case of elastic-elastic bilaminates.

2.4 LATE TIME ASYMPTOTIC SOLUTION

At sufficiently late times after the arrival of the wave front, the stress at a remote position is expected to reach a level σ_o , which corresponds to the applied stress boundary condition at $x = 0$. The transition from the low-amplitude stress at the wave front to this equilibrium state at late-times can be characterized by obtaining the late-time asymptotic solution to the integral

$$\sigma(x_n, t) = \frac{1}{2\pi i} \int_{\gamma-i\infty}^{\gamma+i\infty} \hat{\sigma}(x_n, s) e^{st} ds. \quad (2.12)$$

The integral in Eq (2.12) can be evaluated asymptotically for large t by using the method of steepest descent. To this end, it is convenient to introduce the small time scale

$$\delta = t - x_n / c_{Lave} \quad (2.13)$$

in which c_{Lave} denotes the average wave-speed at which the main parts of the longitudinal disturbance propagates at late time and is given by

$$c_{Lave} = \frac{d}{\left[\left(\frac{l_1}{c_1} \right)^2 + \left(\frac{l_2}{c_2} \right)^2 + \left(\frac{\rho_1 c_1}{\rho_2 c_2} + \frac{\rho_2 c_2}{\rho_1 c_1} \right) \left(\frac{l_1}{c_1} \right) \left(\frac{l_2}{c_2} \right) \right]^{\frac{1}{2}}}. \quad (2.14)$$

It should be noted that c_{Lave} is equivalent to defining the phase velocity of an infinite train of sinusoidal waves of zero frequency, i.e. the long wavelength limit.

It is interesting to note that the speed of longitudinal disturbance at late times depends on the impedance mismatch between the layers. For laminate architectures in which the impedance mismatch is close to one, the late time dispersion wave and the elastic precursor arrive at a particular location at the same time. However, for laminates in which the impedance mismatch is large, c_{Lave} is considerably less than c_{Wave} . This effect is shown graphically in Figure 2.4 for a select number of material pairs.

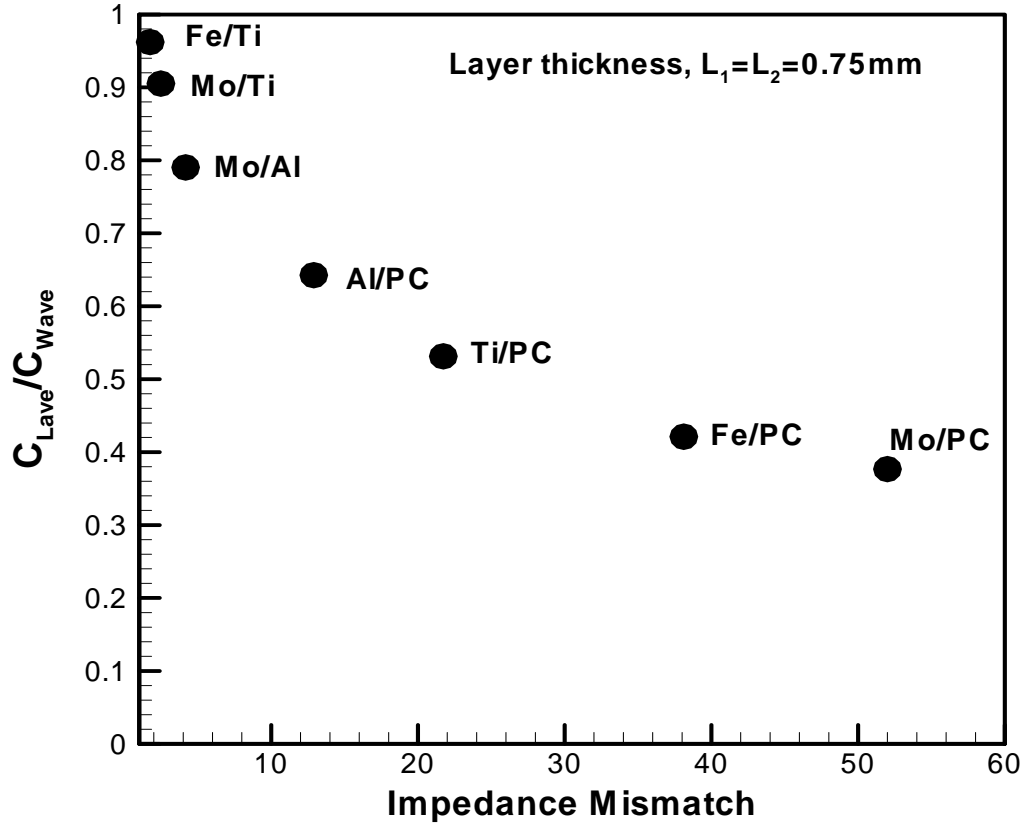


Figure 2.4: The effect of impedance mismatch on the average wave speed c_{Lave} at which the main parts of the longitudinal disturbance propagate at late times.

Substituting Eq (2.13) in Eq (2.12), we can obtain an alternate form of the

inverse transform, i.e.

$$\sigma(x_n, t) = \frac{\sigma_0}{2\pi i} \int_{\Gamma-i\infty}^{\Gamma+i\infty} \frac{e^{-\delta g(s)} e^{th(s)}}{s} ds, \quad (2.15)$$

where

$$g(s) = \mu(s)c_{Lave}, \quad (2.16)$$

and

$$h(s) = \mu(s)c_{Lave} + s. \quad (2.17)$$

In order to evaluate the integral in Eq. (2.15) for $t \rightarrow \infty$, we employ the method of steepest descent (Achenbach, 1973). In view of this it must be noted that the main contribution to the integral is expected to arise from $s = 0$. Expanding $h(s)$ about the saddle point $s = 0$ gives

$$g(s) \cong -s + \frac{h''(0)}{2!}s^2 + \frac{h'''(0)}{3!}s^3 \quad (2.18)$$

and

$$h(s) \cong \frac{h''(0)}{2!}s^2 + \frac{h'''(0)}{3!}s^3. \quad (2.19)$$

In Eqs (2.18) and (2.19), $h''(0)$ and $h'''(0)$ are given by

$$h''(0) = \frac{c_{Lave}^2}{d^2} \left[\left[\frac{l_2^2}{c_2^2} \tau(\gamma^2 - 1) \right] - \frac{l_1 l_2}{c_1 c_2} \left[\tau(\gamma^2 - 1) \left(\frac{\rho_1 c_1}{\rho_2 c_2} \right) \right] \right], \quad (2.20)$$

and

$$\begin{aligned} h'''(0) = & \frac{c_{Lave}^4}{d^4} \frac{l_2(l_2 \rho_2 + l_1 \rho_1)}{4c_1^6 \rho_2^3 \rho_1^3 c_2^6} \{ c_1^2 l_1^2 l_2 \rho_2^3 \rho_1 (l_2 \rho_2 - 2l_1 \rho_1) c_2^4 + l_1^3 l_2 \rho_2^5 c_2^6 \\ & + c_1^6 l_2 \rho_1^3 (l_1^2 l_2 \rho_1^2 + 3(1 + 2\gamma^2 - 3\gamma^4) l_2 \rho_2^2 \tau^2 c_2^2) + 3(1 + 2\gamma^2 - 3\gamma^4) l_1 \rho_2 \rho_1 \tau^2 c_2^2 \\ & + c_1^4 l_1 \rho_2 \rho_1^2 c_2^2 (l_1^2 l_2 \rho_1^2 - 12\gamma^2 (\gamma^2 - 1) l_2 \rho_2^2 \tau^2 c_2^2 - 21 \rho_2 \rho_1 (l_2^2 + 6\gamma^2 (\gamma^2 - 1) \tau^2 c_2^2)) \} \end{aligned} \quad (2.21)$$

where, as before, γ^2 is the ratio between the instantaneous modulus and the rubbery modulus.

In view of Eqs (2.15) to (2.19), the integral in Eq (2.15) along the path of steepest descent Γ can be written as

$$\begin{aligned}\sigma(x, \delta) &= \frac{\sigma_0}{2\pi i} \int_{\Gamma} \frac{1}{s} e^{-\left\{ \frac{h'''(0)}{3!} s^3 + \frac{h''(0)}{2!} s^2 - s \right\} \delta + \left\{ \frac{h'''(0)}{3!} s^3 + \frac{h''(0)}{2!} s^2 \right\} t} ds \\ &= \frac{\sigma_0}{2\pi i} \int_{\Gamma} \frac{1}{s} e^{\delta s + (t-\delta) \frac{h''(0)}{2!} s^2 + (t-\delta) \frac{h'''(0)}{3!} s^3} ds\end{aligned}\quad (2.22)$$

Substituting Eq (2.13) into Eq (2.22) and applying the transformation

$$s = z \left[\frac{6}{(x_n / c_{Lave}) h'''(0)} \right]^{1/3} - \frac{h''(0)}{h'''(0)} \quad (2.23)$$

yields

$$\sigma(x_n, t) = e^A \frac{\sigma_0}{2\pi i} \int_{\Gamma_z} \frac{e^{Bz + z^3}}{z} dz. \quad (2.24)$$

In Eq. (2.24)

$$A = -(t - x_n / c_{Lave}) \frac{h''(0)}{h'''(0)} + \frac{1}{3} \frac{(h''(0))^3}{(h'''(0))^2} (x_n / c_{Lave}) \quad (2.25)$$

and

$$B = \left[(t - x_n / c_{Lave}) - \frac{1}{2} \frac{[h''(0)]^2}{h'''(0)} (x_n / c_{Lave}) \right] \left(\frac{6}{h'''(0)(x_n / c_{Lave})} \right)^{1/3}. \quad (2.26)$$

The path of steepest descent Γ approaches $s = 0$ along the directions

$\arg(s) = -\frac{\pi}{3}$; it is indented to the right around the pole $s = 0$ and leaves the

origin along the direction $\arg(s) = \frac{\pi}{3}$. The contribution to the integral from the

one-third of a circle indentation around the origin is $\sigma_0/3$. Thus, the integral in

Eq. (2.24) along the steepest descent path becomes (Cerrillo, 1950)

$$\sigma(x_n, t) = e^A \sigma_0 \left[\frac{1}{3} + \int_0^B Ah(B) dB \right], \quad (2.27)$$

in which $Ah(B)$ is the Airy Hardy function

$$Ah(B) = \frac{1}{2\pi i} \int_{\Gamma} e^{Bz+z^3} dz. \quad (2.28)$$

After certain algebraic manipulations it can be shown that Eq. (2.12) can be

expressed as

$$\sigma(x_n, t) = \sigma_0 e^A \left[\frac{1}{3} + \sum_{m=0}^{\infty} \frac{\Gamma\left(\frac{m+1}{3}\right)}{(m+1)!} B^{m+1} \sin\left(\frac{\pi}{3}(m+1)\right) \right] \quad (2.29)$$

where $\Gamma(m)$ is the gamma function defined as

$$\Gamma(m) = \int_0^{\infty} t^{m-1} e^{-t} dt \quad \text{for } m > 0. \quad (2.30)$$

For infinitesimal deformation, solutions for elastic precursor decay and late-time dispersion which satisfy zero stress and particle velocity initial conditions and boundary conditions given by a step loading function in time, are summarized in Figure 2.5. Upon impact of the laminate, a two wave structure is obtained. The leading elastic precursor propagates at a speed dictated by the average wave speed in the two constituents given by c_{Wave} , while the late-time dispersed front arrives at a speed c_{Lave} . The late time stress wave oscillates about a mean level dictated by the amplitude of the input stress pulse.

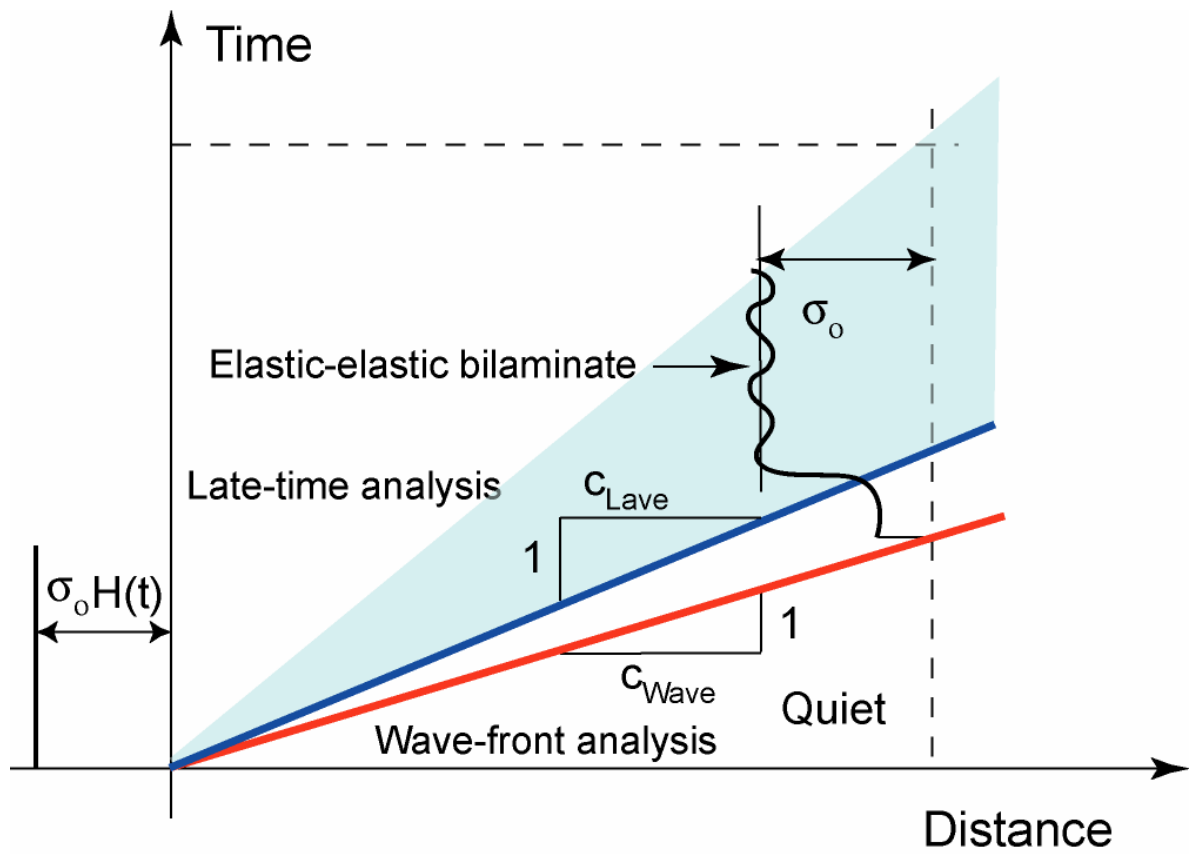


Figure 2.5: The two wave structure obtained during impact of a typical elastic bilaminate.

2.5 ANALYTICAL RESULTS AND DISCUSSION

Next, stress wave profiles obtained from the asymptotic solutions at the wave front and the waveform at late times are presented. These simulations are designed to illustrate the effect of impedance mismatch, distance of wave propagation, layer thickness, i.e. cell size, density of interfaces, and material inelasticity on the amplitude of stress wave at the wave front and the dispersive characteristics of the waveform at late times. The simulations are carried out for elastic-elastic bilaminates comprising Ti-Fe and Mo-Fe material pairs, and elastic-viscoelastic bilaminates comprising Al-PC material pair. The acoustic impedance mismatch for Ti-Fe and Mo-Ti bilaminates is 1.75 and 2.45, respectively. For the Al-PC bilaminates the acoustic impedance mismatch is 8.31. Three different layer thicknesses are evaluated for the Ti-Fe and Mo-Fe laminates: 0.75 mm, 1.5 mm and 2.25 mm for total laminate thickness of 9 mm. For the Al-PC laminates the simulations are presented for layer thickness of 0.125 mm with total laminate thicknesses of 0.5 mm, 1.0 mm and 1.5 mm. The relaxation time in Eq (2.4) for PC is taken to be $\tau = 2\mu s$. The ratio of the

instantaneous modulus to the rubbery modulus, i.e. $G(0)/G(\infty)$, is taken to be

1.01. Table 2.1 gives the physical properties of all the materials used in the simulations.

Layer Material	Elastic Modulus (GPa)	Density (g/cm ³)	Longitudinal Wave Speed (m/s)	Acoustic Impedance GPa-mm/ μ s
Titanium (Ti)	120.2	4.5	6716	30.22
Iron (Fe)	211.4	7.87	5950	46.83
Molybdenum (Mo)	324.8	10.22	6250	63.88
Aluminum (Al)	70.6	2.7	6420	17.33
Polycarbonate (PC)	2.3	1.2	1832	2.20

Table 2.1: Physical properties of the material layers employed in the simulations.

Figure 2.6 and Figure 2.7 present the predictions of the wave profiles for elastic-elastic bilaminates illustrating the effects of impedance mismatch on the wave front and late-time dispersion wave characteristics. Two different bilaminates are considered: Fe-Ti bilaminates with an impedance mismatch of 1.75 and Mo-Ti

bilaminates with an impedance mismatch of 2.48. In each case the thickness of the individual layers is 0.75 mm. The abscissa represents the time after impact while the ordinate represents the theoretical normal stress normalized by the amplitude of the input stress. The stress profiles are shown at a propagation distance of 3mm, 6mm, and 9mm. As discussed earlier, for each laminate a two-wave structure is obtained. A leading wave front (elastic precursor) that propagates at the speed c_{Wave} , and a late-time dispersion wave propagating at the speed c_{Lave} . For the case of Mo-Ti bilaminates a larger precursor decay as well as a lower frequency of the late time dispersive waves is observed. Also, consistent with Eqs (2.9) and (2.14), the time difference between the arrival of the leading wave front and the late time dispersive wave is much longer in the case of Mo-Ti laminates when compared with the Fe-Ti laminates. It is also interesting to note that for both cases the late-time dispersive waves show steady wave profiles with increasing distance of propagation into the bilaminates.

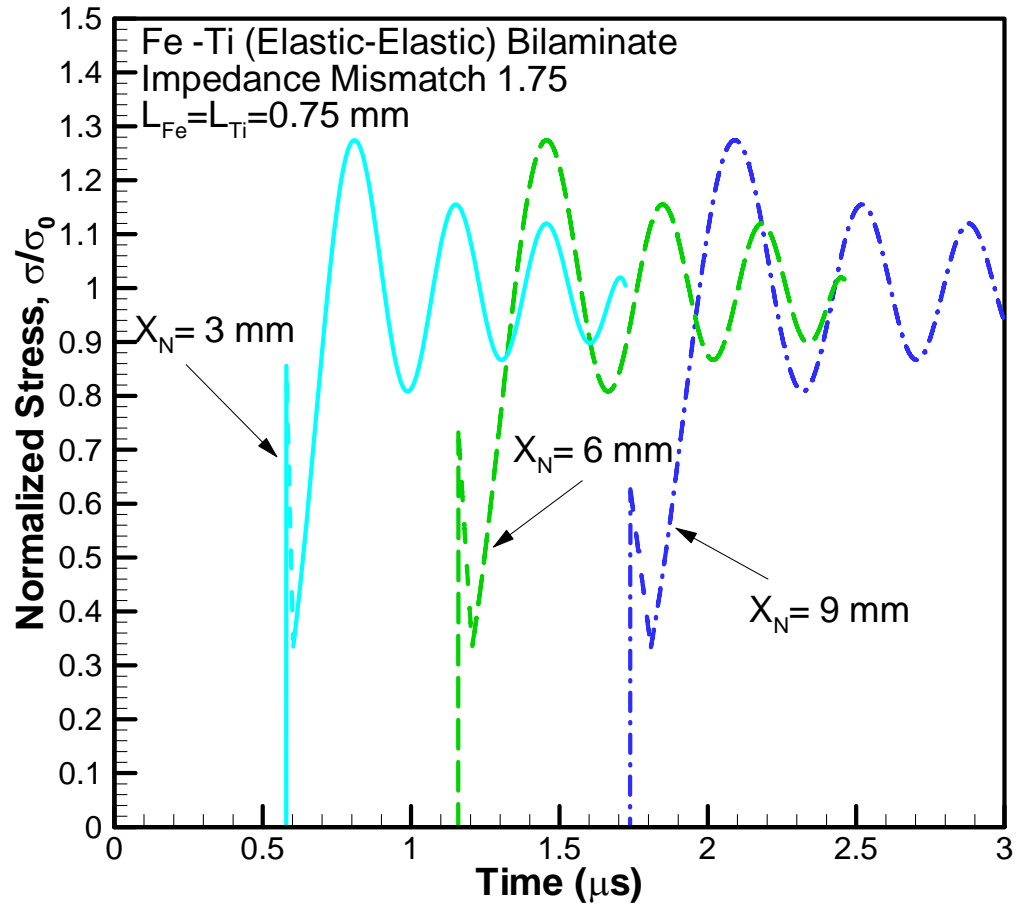


Figure 2.6: Effect of distance of propagation on the elastic precursor and late-time dispersion for Fe-Ti laminates.

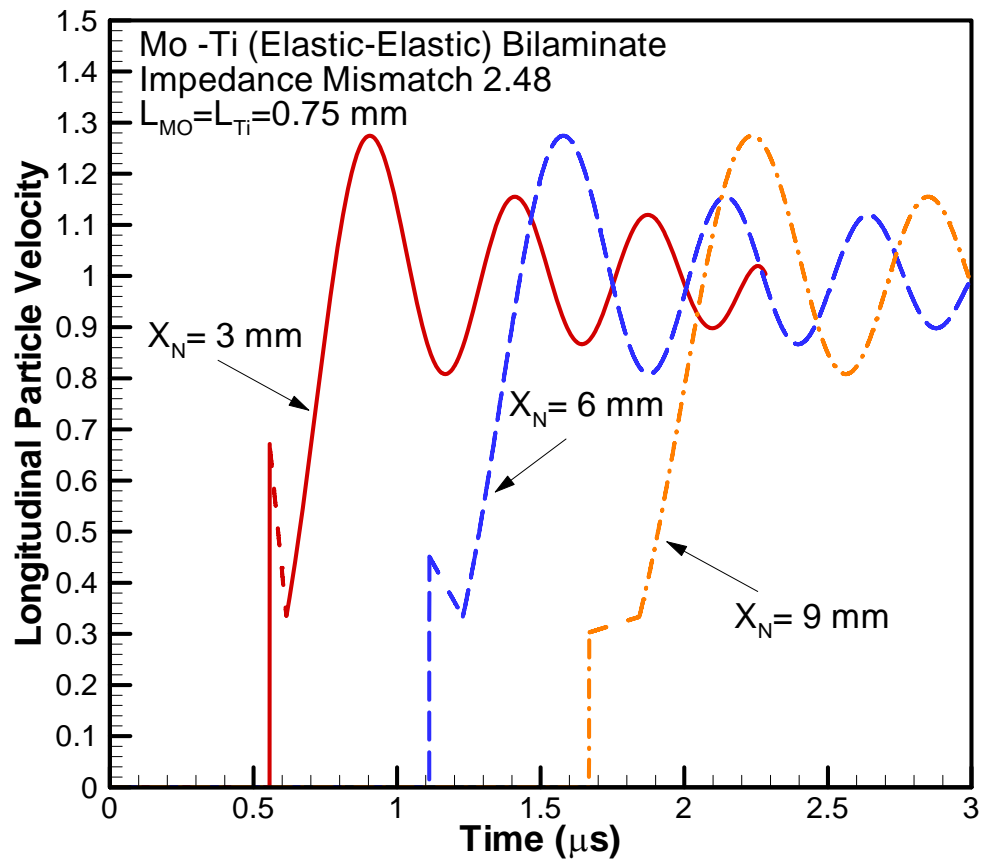


Figure 2.7: Effect of distance of propagation on the elastic precursor and late-time dispersion for Mo-Ti laminates.

Figure 2.8 shows the effect of the layer thickness on the elastic precursor decay and late time dispersion during propagation of stress waves in Ti-Fe laminates. Results for three different layer thicknesses are presented: 0.75 mm, 1.5 mm and 2.25 mm. As expected, the arrival of the elastic precursor at $x_n = 9$ mm occurs at the same time for the three different laminate architectures. However, the laminates with largest layer thickness, i.e. 2.25 mm, shows the smallest elastic precursor decay, while the laminate with the smallest layer thickness, i.e. 0.75 mm, shows the highest precursor decay. The late-time dispersive wave for the smallest layer thickness laminates contain the highest frequency oscillations while the largest layer thickness laminates contain the lowest frequency oscillations. Also, the rise-time associated with the late-time dispersive wave decreases with layer thickness and an increase in the density of interfaces (i.e. number of layers in a given laminate thickness).

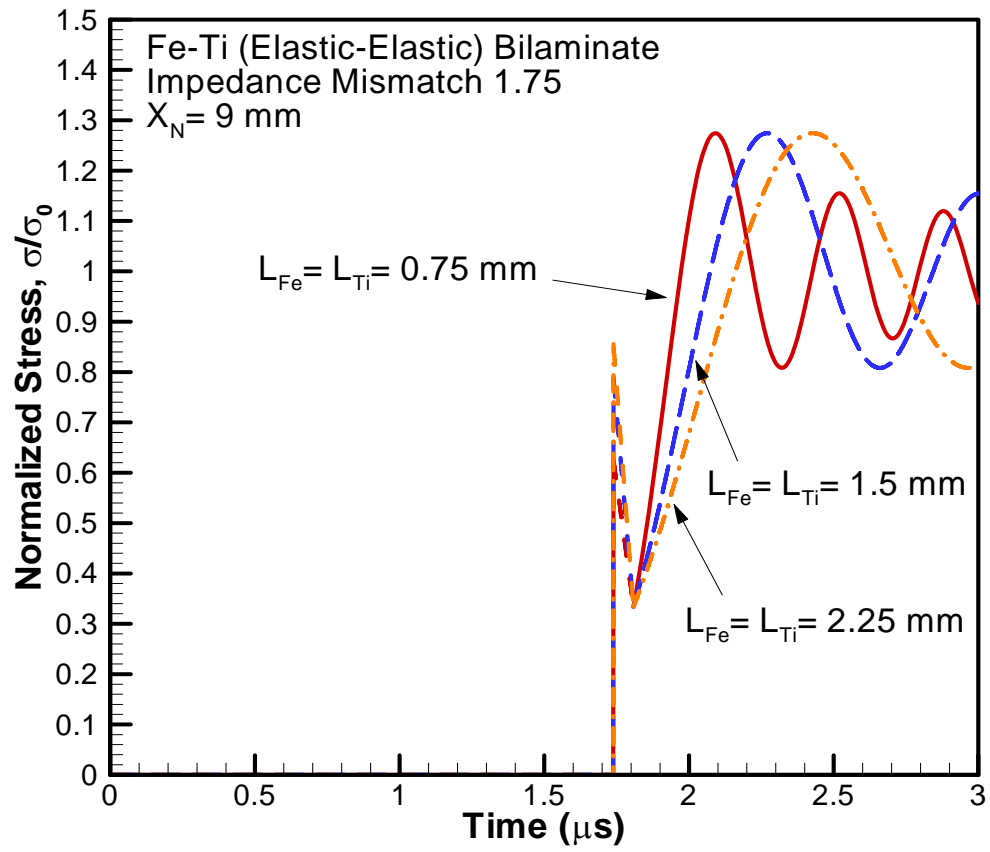


Figure 2.8: Effect of layer thickness on the elastic precursor and the late-time dispersion for Fe-Ti laminates.

Figure 2.9 shows the wave-front as well as the late-time solution for the Al-PC laminate for $x_n=0.5$ mm, 1 mm and 1.5 mm. The impedance mismatch for the Al-PC material pair is 8.3. The thickness of each Al and PC layer is 0.125 mm. Due to the relatively high impedance mismatch between the Al and PC layers, and also the viscoelasticity associated with PC, a very strong elastic precursor decay is observed; so-much-so that the elastic precursor is reduced to approximately zero as the stress wave propagates only 0.5 mm into the laminate. This is seen more clearly from the insert in Figure 2.9, which shows the early parts of the wave profiles for the three thicknesses. Also, it is interesting to observe that the frequency of the oscillations in the late-time dispersive wave solution is much smaller when compared to the lower impedance mismatch Mo-Ti and Ti-Fe material pair laminates.

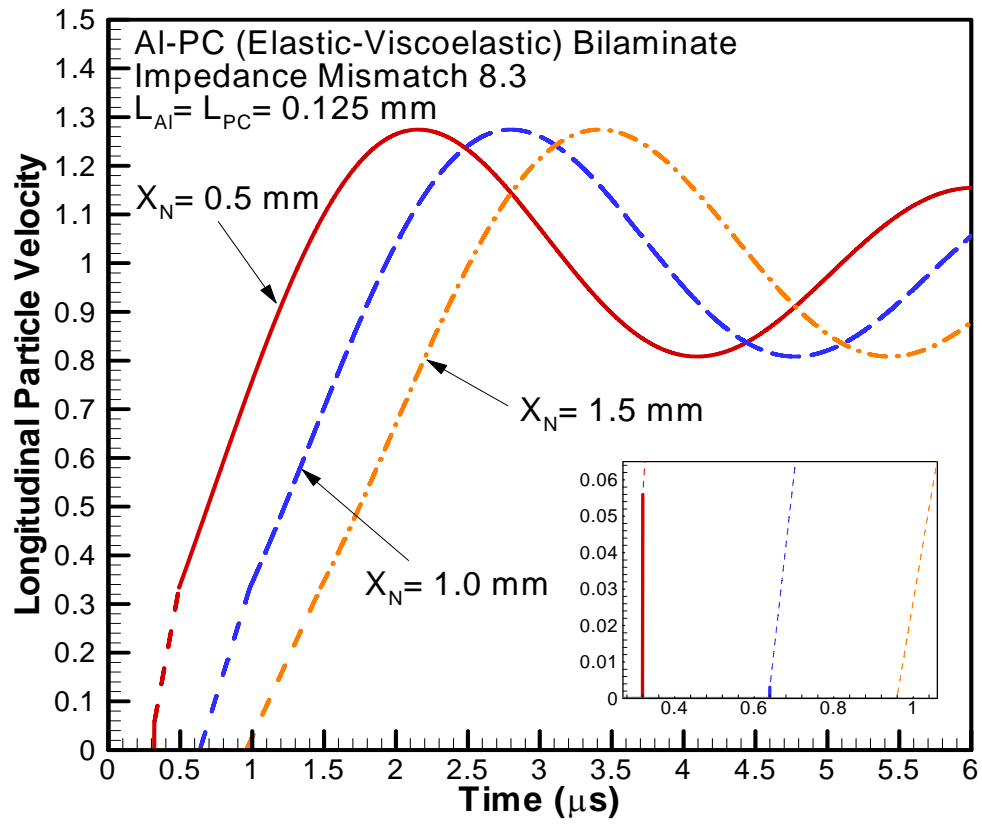


Figure 2.9: Wave front and late-time dispersion results for Al-PC bilaminates.

Figure 2.10 compares the late-time dispersion characteristics for several select material pairs with different impedance mismatch laminates. Because of the dependence of c_{Lave} on the impedance mismatch, the dispersion profiles have been shifted in time so as to start at the same point in time. The late-time dispersion profiles can be characterized by the rise time and the frequency of the oscillations contained in the wave profiles. The rise times of the dispersion waves is observed to increase with an increase in impedance mismatch, while the frequency of the oscillations decreases with an increase in the impedance mismatch. Also, the late-time dispersive wave oscillates about the mean level corresponding to the input stress. The maximum amplitude of the late time dispersion wave is $\sim 1.3 \sigma_o$, and is observed to be independent of the impedance mismatch of the elastic-elastic laminates. Also, it is interesting to note the effect of material inelasticity on the dispersion characteristics of the late time wave profiles. With an increase in the ratio between the instantaneous modulus to the rubbery modulus the rise time associated with the late time dispersive waves is observed to increase while the frequency of the oscillations decreases.

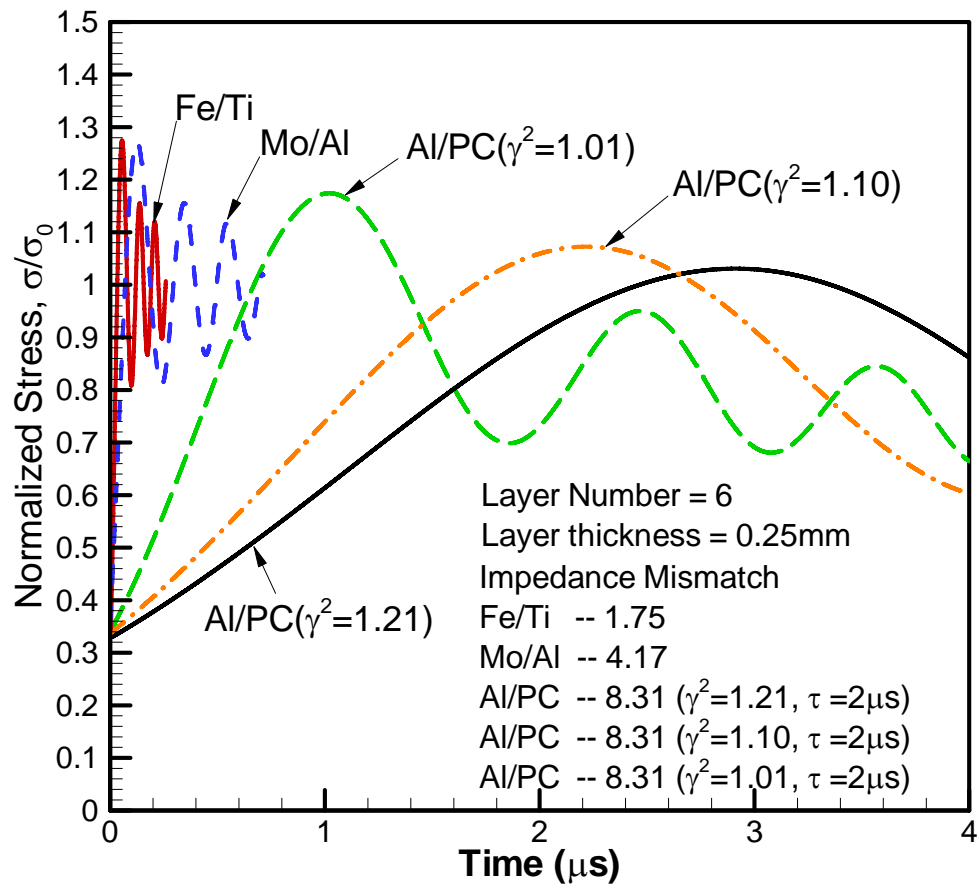


Figure 2.10: Characteristics of late-time dispersion for select material pairs with different impedance mismatch.

2.6 SUMMARY

Asymptotic techniques were applied to analyze propagation of acceleration waves in 2-D layered material systems. The analysis makes use of the Laplace transform and Floquet theory for ODE's with periodic coefficients (Chen and Clifton, 1974). Both wave-front and late-time solutions for step-pulse loading on layered half-space were described for several elastic/elastic and elastic/visco-elastic bilaminates.. The elastic precursor was found to decrease with increasing propagation distance, layer density, or impedance mismatch. The late time oscillation frequency was found to decrease with increasing impedance mismatch or decreasing layer density. The material in-elasticity was found to dramatically decrease the late-time oscillation frequency and elastic precursor.

REFERENCES

- Achenbach J. D., 1973. Wave Propagation in Elastic Solids. North-Holland, Amsterdam.
- Barker L. M., Lundergan C. D., Chen P. J. and Gurtin M. E., 1974. Nonlinear viscoelasticity and the evolution of stress waves in laminated composites: a comparison of theory and experiment. *Journal of Applied Mechanics* 41, 1025-.
- Benson D. J. and Nesterenko V. F., 2001. Anomalous Decay of shock impulses in laminated composites. *Journal of Applied Physics* 89(7), 3622-3626.
- Betheney W., DeLuca E., Prifti J. and Chou S. C., 1998. Ballistic impact damage of S2-glass reinforced plastic structural armor. *Composites Science and Technology* 58, 1453-1461.
- Cerrillo M V, 1950. Technical Report No.55, 2a, Research Laboratory of Electronics MIT, Cambridge, MA.
- Chen C. C. and Clifton R. J., 1974. Asymptotic Solutions for Wave Propagation in Elastic and Viscoelastic Bilaminates. In: *Developments in Mechanics, Proceedings of the 14th Mid-Eastern Mechanics Conference*: 26, 8., pp. 399-417.
- Clifton R. J., 1972. Solution of wave problems in inelastic materials. In: *Summer Course on Dynamics of Inelastic Materials* Jablonna, Poland.
- Fink B., 2000. Performance metrics for composite integral armor. *Journal of Thermoplastic Composite Materials* 13(5), 417-431.
- Hegemier G. A., 1972. On a theory of interacting continua for wave propagation in composites. In: *Dynamics of Composite Materials*. ed(s): E. H. Lee. ASME, pp. 70-121.
- Hemsing W. F., 1979. Velocity sensing interferometer (VISAR) modification. *Review of Scientific Instrumentation* 50(1), 73-78.

Hill W H and Shimmin K D, 1961. Elevated Temperature Dynamic Elastic Moduli of Various Metallic Materials. WADD Twchnical report 60-438. Wright-Patterson Air force base, Ohio.

Laptev V. I. and Trishin Y. A., 1976. The increase of velocity and pressure under impact on inhomogeneous target. Journal of Applied Mechanics and Technical Physics, 837-841.

Lundergan C D and Drumheller D S, 1971. Dispersion of shock waves in composite materials. Shock Waves and the Mechanical Properties of Solids. Syracuse University Press, New York, p 141-.

Nesterenko V F, Fomin V M and Cheskidov P A, 1983. Attenuation of strong shock waves in laminate materials. Nonlinear Deformation Waves. Springer Verlag, Berlin, pp 191-7.

Nesterenko V. F., Fomin V. M. and Cheskidov P. A., 1984. Damping of strong waves in laminar materials. Journal of Applied Mechanics and Technical Physics, 567-575.

Oved Y., Luttwak G. E. and Rosenberg Z., 1978. Shock wave propagation in layered composites. Journal of Composite Materials 12, 84-.

Peck J. C. and Gurtman G. A., 1969. Dispersive pulse propagation parallel to the interfaces of a laminated composite. Journal of Applied Mechanics, 479-484.

Sherby O. D., Lee S., Koch R., Sumi T. and Wolfenstine J., 1990. Multilayered composites based on ultrahigh carbon steel and brass. Materials and Manufacturing Processes 5, 363-376.

Stern M., Bedford A. and Yew C. H., 1970. Wave propagation in viscoelastic laminates. Journal of Applied Mechanics 70-WA/APM-40, 1-7.

Sun C.-T., Achenbach J. D. and Herrmann G., 1968. Time-harmonic waves in a stratified medium propagating in the direction of the layering. Journal of Applied Mechanics, 408-411.

Sve C., 1971. Thermo-elastic Waves in a Periodically Laminated Medium. International Journal of Solids Structures, 7, 1363-1373.

Sve C., 1972. Stress wave attenuation in composite materials. Journal of Applied Mechanics, 1151-1153.

Vaidya U. K., Hosur M. V., Kumar P., Mahfuz H., Haque A. and Jeelani S., 1999. Impact damage resistance of innovative functional sandwich composites. In: ASME 1999 Mechanics and Materials Conference Blacksburg, VA.

Zhuang S, 2002. Shock Wave Propagation in Periodically layered composites. PhD Dissertation, California Institute of Technology, Pasadena, CA.

Chapter 3

STRUCTURE OF WEAK SHOCK WAVES IN 2-D LAYERED HETEROGENEOUS MATERIAL SYSTEMS

3.1 Introduction

In view of the scientific and technological importance of heterogeneous materials in shock related applications and our current incomplete state of understanding of their performance under impact loading conditions, integrated experimental-analytical research is being conducted. In chapter 2, asymptotic solutions were established to explore the two-wave structure for selected elastic/elastic and elastic/visco-elastic bilaminate materials. The effects of layer density, impedance mismatch, propagation distance, and material in-elasticity to the elastic precursor and late-time oscillations were discussed. In this chapter, experiment results were presented to compare with the asymptotic solutions in chapter 2. Iron/titanium and aluminum/polycarbonate bilaminates were shock compressed to between 0.8

to 1.9 GPa and the free surface velocities were recorded using VISAR system.

The observed elastic precursors and late-time wave profiles showed good agreements with the asymptotic solutions. The effects of material in-elasticity were found to affect the two-wave structure dramatically.

3.2 Experimental Configuration

The experiments described in this paper are designed to illustrate the effect of impedance mismatch, layer thickness, and material inelasticity on the elastic precursor decay and late-time dispersion characteristics of weak shock waves in 2-D laminates. In view of this, normal plate impact experiments are conducted on laminates comprising alternating Ti-Fe (elastic-elastic) and the Al-PC (elastic-viscoelastic) layers. The experiments are conducted using the 82.5mm single-stage gas-gun at Case Western Reserve University. The experiments involve the impact of an elastic flyer plate with a target assembly at normal incidence. The target assembly is a sandwich in which the laminate under investigation is confined between two metal plates that remain elastic under impact. Impact takes place on the front target plate; the waves transmitted through the layered

specimen are monitored on the free surface of the rear target plate by means of laser interferometer. The measured motion at the free surface of the rear target plate and the known elastic properties of the front and the rear target plates are used to obtain the wave characteristics as the shock wave propagates through the layered specimen.

The schematic of the plate-impact experimental configuration is shown in Figure 3.1. A fiberglass projectile carrying the flyer plate is accelerated down the gun barrel by means of compressed nitrogen gas. The rear end of the projectile has sealing O-ring and a plastic (Teflon) key that slides in a key-way inside the gun barrel to prevent any rotation of the projectile. In order to reduce the possibility of an air cushion between the flyer and target plates, impact takes place in a target chamber that has been evacuated to 50 μm of Hg prior to impact. A laser based optical system utilizing a UNIPHASE Helium-Neon 5mW laser (Model 1125p) and a high frequency photo-diode is used to measure the velocity of the projectile. To ensure the generation of plane waves with wave-front sufficiently

parallel to the impact face, the flyer and the target plates are carefully aligned to be parallel to within 2×10^{-5} radians by using an optical alignment scheme. The actual tilt between the two plates is measured by recording the times at which four, isolated, voltage-biased pins, that are flush with the surface of the target plate, are shorted to ground. The acceptance level of the experiments is of the order of 0.5 mrad. A VALYN VISAR laser interferometer is used to measure the history of the normal particle velocity at the rear surface of the target plate. A COHERENT VERDI 5 Watt solid-state diode-pumped frequency doubled Nd:YVO₄ CW laser with wavelength of 532 nm is used to provide a coherent monochromatic light source.

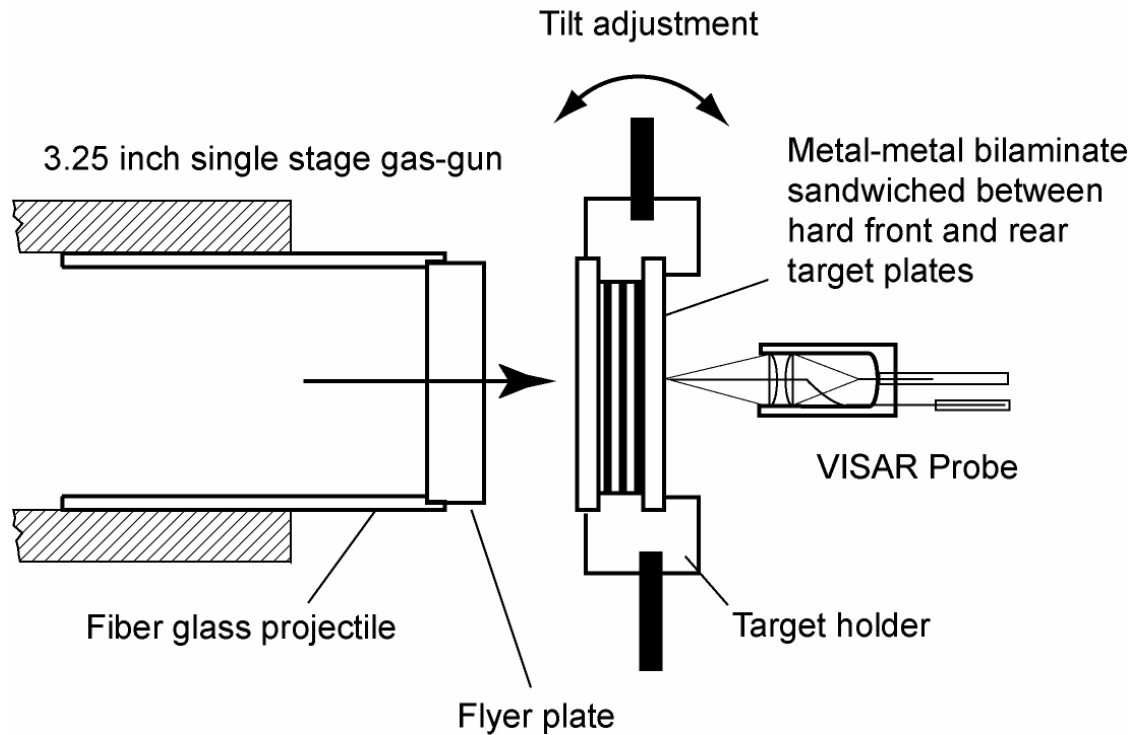


Figure 3.1: Schematic of the plate impact configuration employed in the present investigation. The layered specimen is sandwiched between two hard plates of the target assembly.

The schematic of the light path of the laser interferometer is shown in Figure 3.2.

The VALYN VISAR is based on the wide angle Michelson interferometer (WAMI) concept and capable of velocity measurements from either a spectrally or diffusely reflecting specimen surface. Using a laser light coupler, the light from the laser is coupled into an optical fiber of diameter $125\ \mu m$ which directs light onto the surface of the specimen. By an optical assembly called the optical fiber

probe, the reflected light is collected and coupled into an out-going fiber which has a diameter of $300\text{ }\mu\text{m}$. The laser light from the out-going fiber, which contains the Doppler shift effect due to the motion of the surface under shock loading, is collimated and then directed into the VISAR optical system to extract the interferometer information of particle velocity. In order to monitor any intensity change of the reflected laser beam resulting from self illumination due to shock compression, part of the light is sampled by a beam sampler and directed to a photomultiplier tube, which converts the light signal into an electric signal to be recorded on the oscilloscope. The 50/50 large beam splitter evenly splits the light from the main beam into two; one is sent to a PZAT mirror of the interferometer, while the other passes through a $1/8$ wave plate, etalon and then is returned by a mirror. One half of the returned light passing through the 50/50 large beam splitter is combined with the reflected part of the returned beam from PZAT mirror to form interference fringes. The other half of the returned light from the PZAT mirror is combined with the beam passing through the 50/50 large beam splitter and reflected from the mirror to form interference fringes.

The alignment of the interfering laser beams which give rise to the interference fringe pattern is optimized by monitoring the bull's eyes pattern. Each interference pattern then passes through two separate polarizing beam splitters, separating the S and P components of the laser light, which have a 90° phase angle difference due to the retardation of a $1/8$ wave plate to the phase angle of the P component of light. In order to increase the signal to noise ratios the two s -polarized beams and the two p -polarized beams, which are both 180° out of phase, are subtracted (Hemsing, 1979). This feature known as push-pull significantly reduces the noise level introduced by incoherent light entering the interferometer. The subtracted S and P components of the interference fringes are directed into two photomultiplier tubes. Separately recording the S and the P fringes (quadrature coding) eliminates the ambiguity in the sign of the acceleration and improves accuracy when data reduction is performed using the high resolution regimes of the traces. The electrical signals from the photomultipliers are amplified by 1.2 GHz bandwidth amplifiers before being sent to 1 GHz digital oscilloscope for recording.

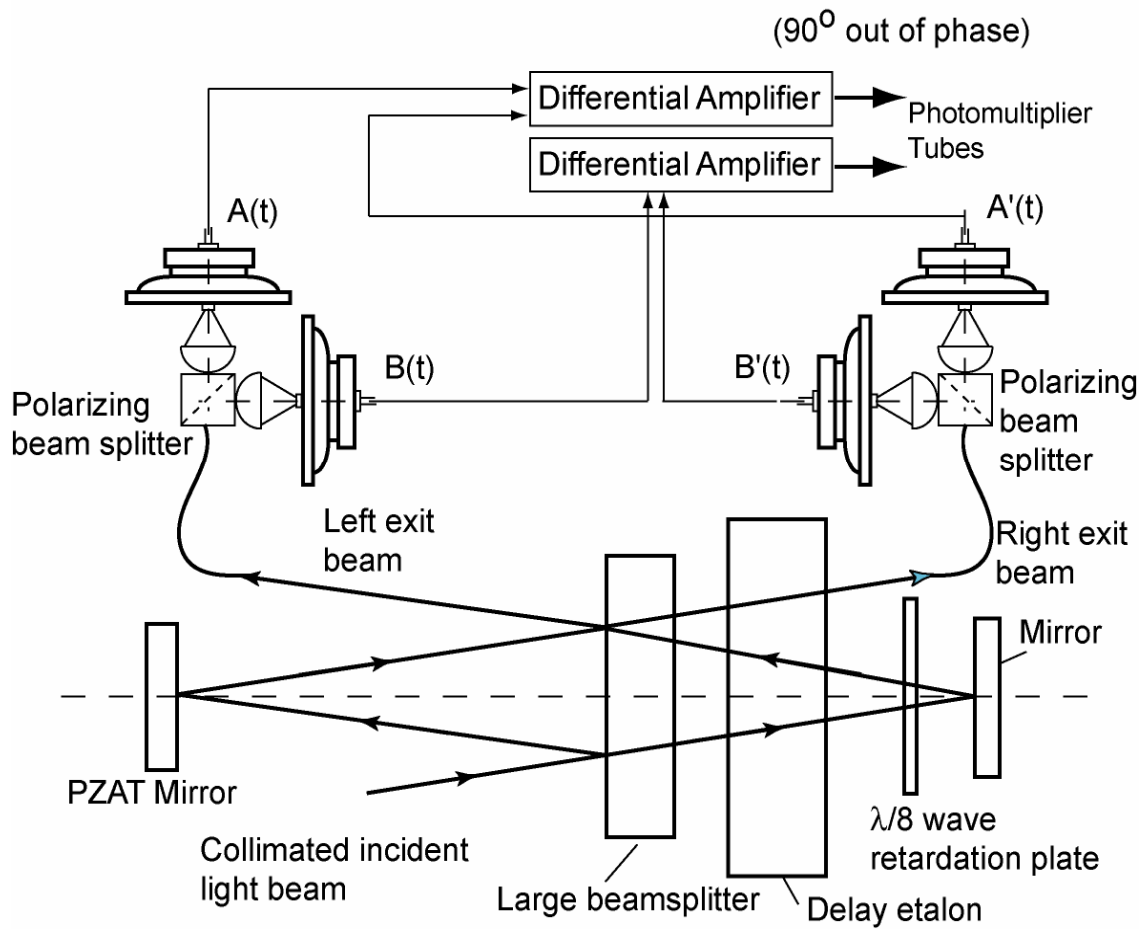


Figure 3.2 : Schematic showing the light path in a VISAR interferometer.

Figure 3.3 shows a typical oscillograph of the recorded VISAR signal (Shot LT24). The resonant oscillations induced by the multiple reflections of the shock wave at the material interfaces are clearly seen in the record. Part of the data reduction procedure involves plotting the amplitudes of the two fringe records

against each other at each data reading time, thereby forming a Lissajous plot of the data. This plot for Shot LT24 is shown in Figure 3.4. The Lissajous plot allows the user to judge whether certain corrections to the input data are warranted. The judgment is based in part on how nearly the Lissajous plot resembles a perfect circle, which would be the result if the fringe amplitudes of the two data sets were equal, and if the phase difference were 90 degrees. Judging from Figure 3.4, the Lissajous of this experiment is a near perfect circle, which confirms the high quality of the interference signal.

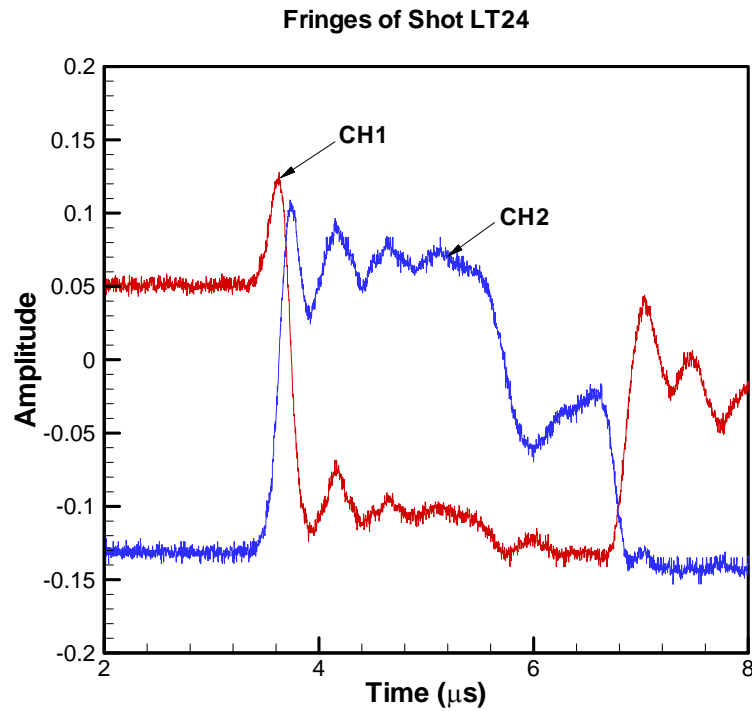


Figure 3.3: Oscillographs of VISAR signals for Shot LT24.

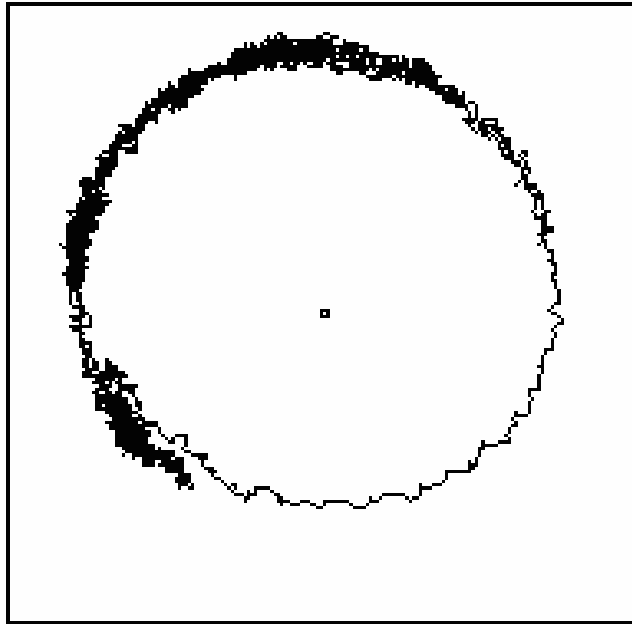


Figure 3.4: Lisajous showing the amplitude of the VISAR fringe records plotted against each other at each time data.

3.3 Results and Discussion

In the present study four series of experiments were designed and conducted. The first series of experiments involved the investigation of the effect of distance of propagation on elastic precursor decay and the late-time dispersion. The experiments were conducted using Fe-Ti laminates. The thickness of each Fe and Ti layer in the laminate was 0.75 mm. A schematic of the experimental configuration is shown in Figure 3.5. In the first experiment (Shot LT07) 12 alternating layers of Fe and Ti with a total laminate thickness of 9 mm were utilized. In the second experiment (Shot LT06) 4 alternating layers of Fe and Ti with a total laminate thickness of 3 mm were utilized. For both experiments the flyer plate was made from hardened CH tool-steel, and was approximately 16 mm in thickness. The thicknesses of the front and rear CH tool-steel plates that sandwich the laminate were 8.65 mm and 5.14 mm, respectively. The relatively large thickness of the flyer plate precludes any unloading waves from the back surface of the flyer plate to reach the flyer/target interface during the total window time of the experiment.

Figure 3.6 shows experimental results on the Ti-Fe laminates. The impact velocities for Shots LT07 and LT06 were 74 m/s and 79 m/s, respectively. In the figure the abscissa represents the time after impact while the ordinate represents the normalized particle velocity measured at the free surface of the target plate. For both experiments the impact velocity is used as the normalization factor for the y axis. The elastic precursor arrives at the free surface of the target plate at approximately $4.2\mu s$ for Shot LT06 and at $5.65\mu s$ for Shot LT07. The later arrival of the elastic precursor in the case of Shot LT07 is consistent with the larger thickness of the laminate employed in Shot LT07. The precursor decay is much higher for Shot LT07 indicating that the decay increases with distance of propagation. The late-time dispersion arrives after the arrival of the elastic precursor. The highest particle-velocity attained observed in the measured wave profiles is approximately 1.2 times the impact velocity and the late-time dispersive wave is observed to oscillate about a mean level 1.0. As expected, the frequency of the oscillations is not affected by the distance the wave propagates into the laminates and is essentially the same for the two experiments. Also, the

amplitude of these oscillations is observed to decay with time. It is interesting to note that the general characteristics of the wave structure are strikingly similar to the analytical predictions for wave front and late time dispersive waves as shown in chapter 2.

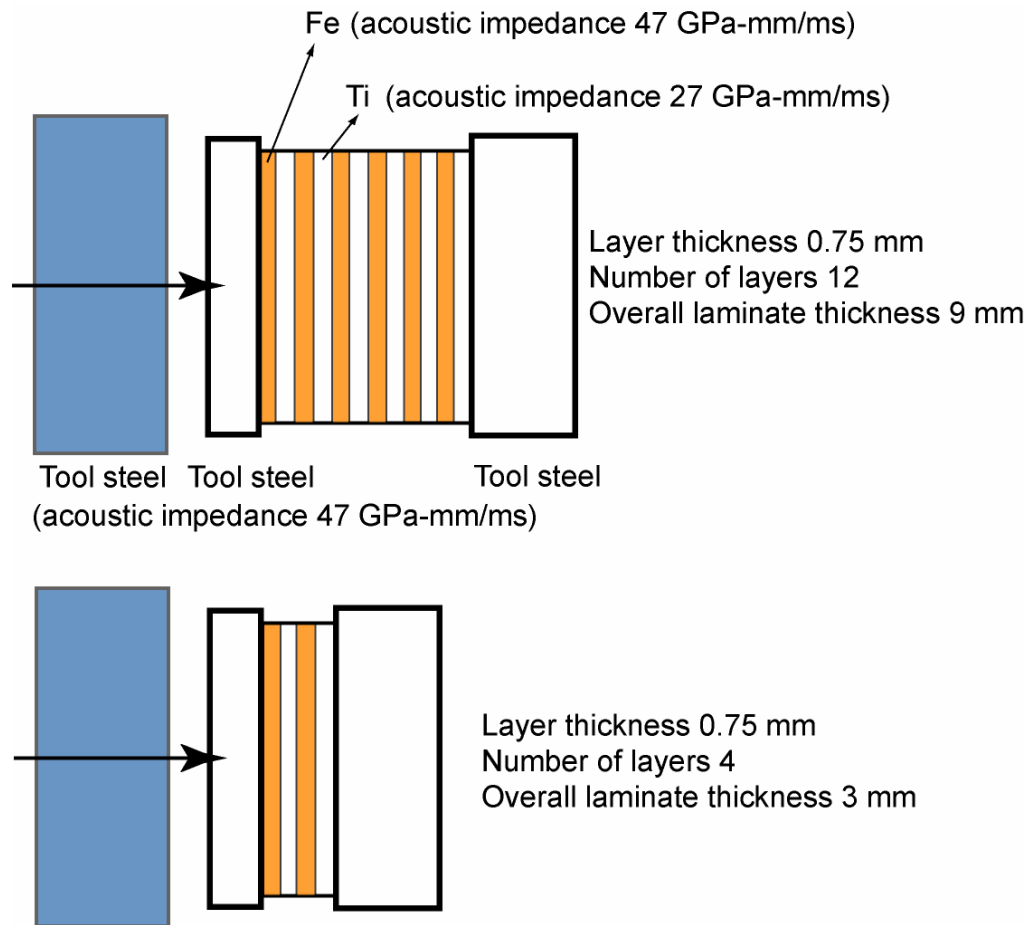


Figure 3.5: Schematic of the laminate architecture employed to conduct the first series of plate impact experiments.

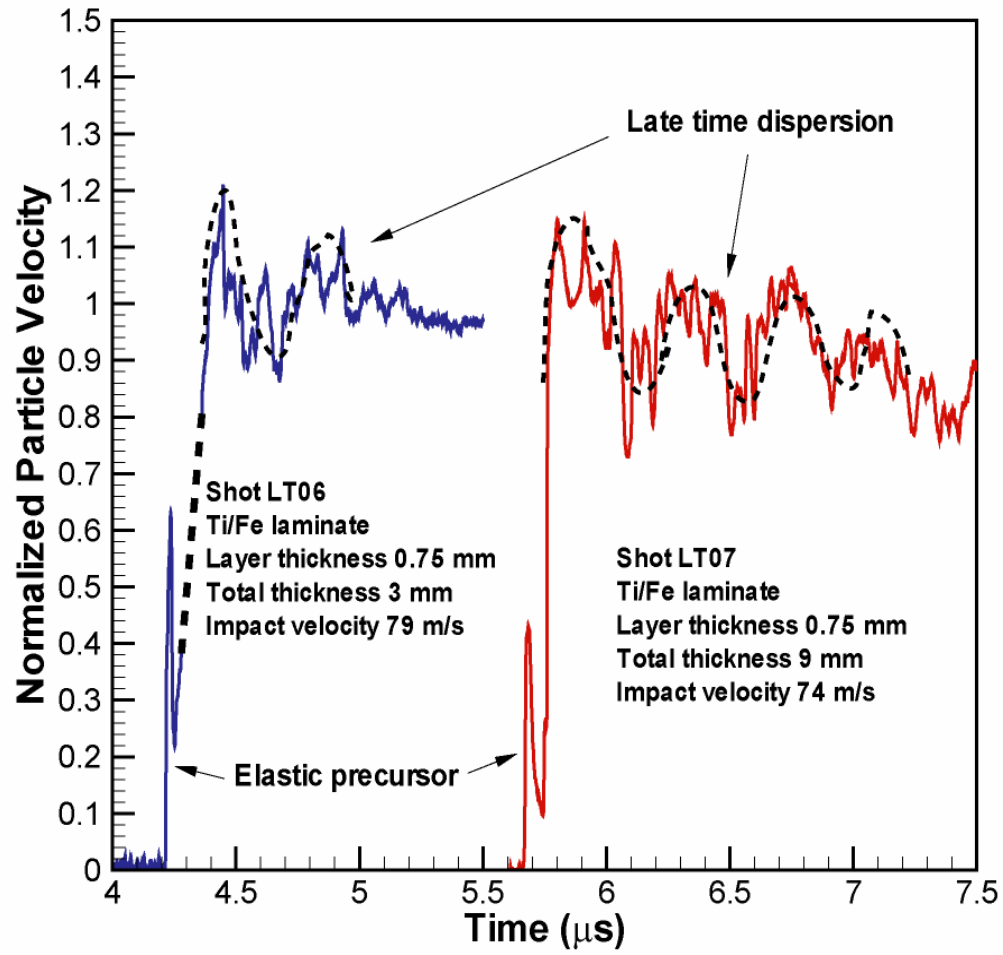


Figure 3.6: Results of plate impact experiments on Fe-Ti laminates showing the effect of distance of propagation on precursor decay and late time dispersion.

The second series of experiments was conducted to understand the effects of density of interfaces on the elastic precursor decay and late time dispersion. Again, in this series of experiments Fe-Ti laminates were utilized. A schematic of the layer architectures employed in this series of experiments is shown in Figure 3.7. For the two experiments the overall thickness of the laminate was 9 mm. In the first experiment (LT07) 12 alternating layers of Fe and Ti with an individual layer thickness of 0.75 mm were utilized. In the second experiment 6 alternating layers of Fe and Ti with an individual layer thickness of 1.5 mm were utilized. Figure 3.8 shows the results of the two experiments conducted in this series. The impact velocities for Shot LT07 and LT09 were 74 m/s and 71m/s, respectively. It can be seen that the precursor decay for Shot LT07 is much greater than that obtained for Shot LT09. Moreover, the rise-time associated with the late-time dispersive wave is shorter for Shot LT07 when compared with Shot LT09. The frequency of oscillations in the late-time dispersive wave is higher for the Shot LT07 when compared with Shot LT09. These results are all consistent with the analytical results shown in chapter 2 for Fe-Ti laminates.

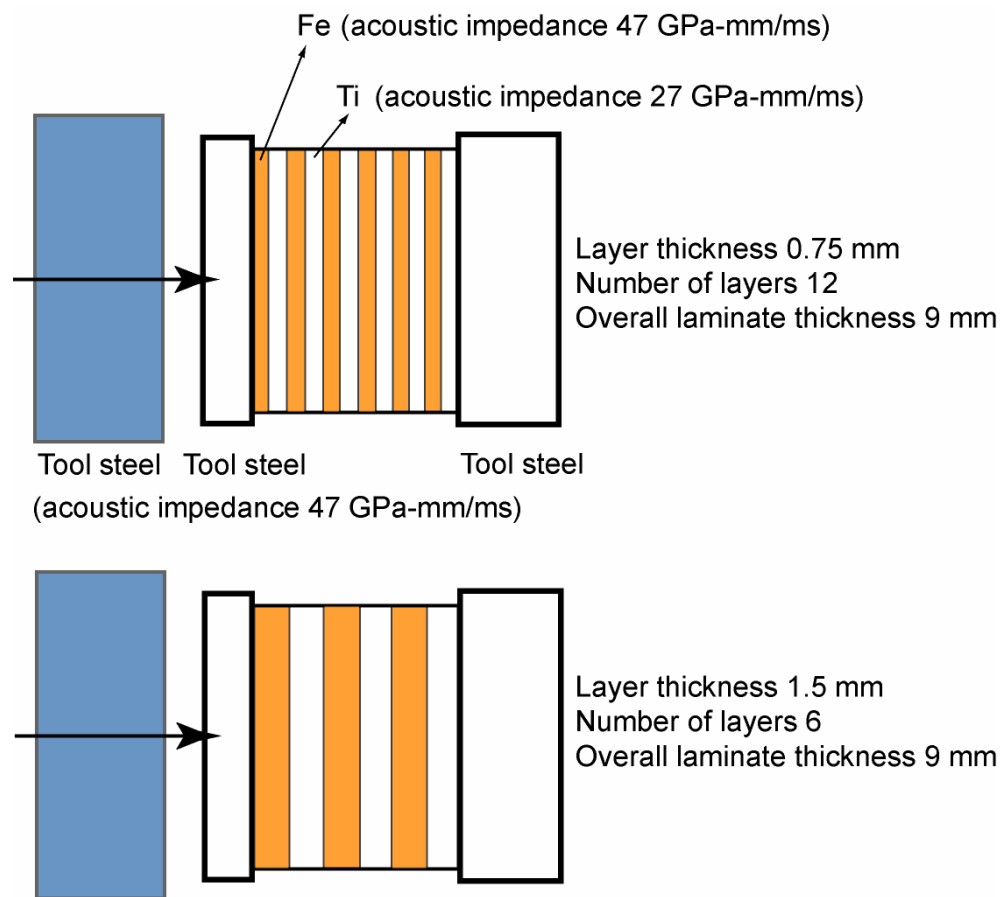


Figure 3.7: Schematic of the laminate architecture employed to conduct the second series of plate-impact experiments.

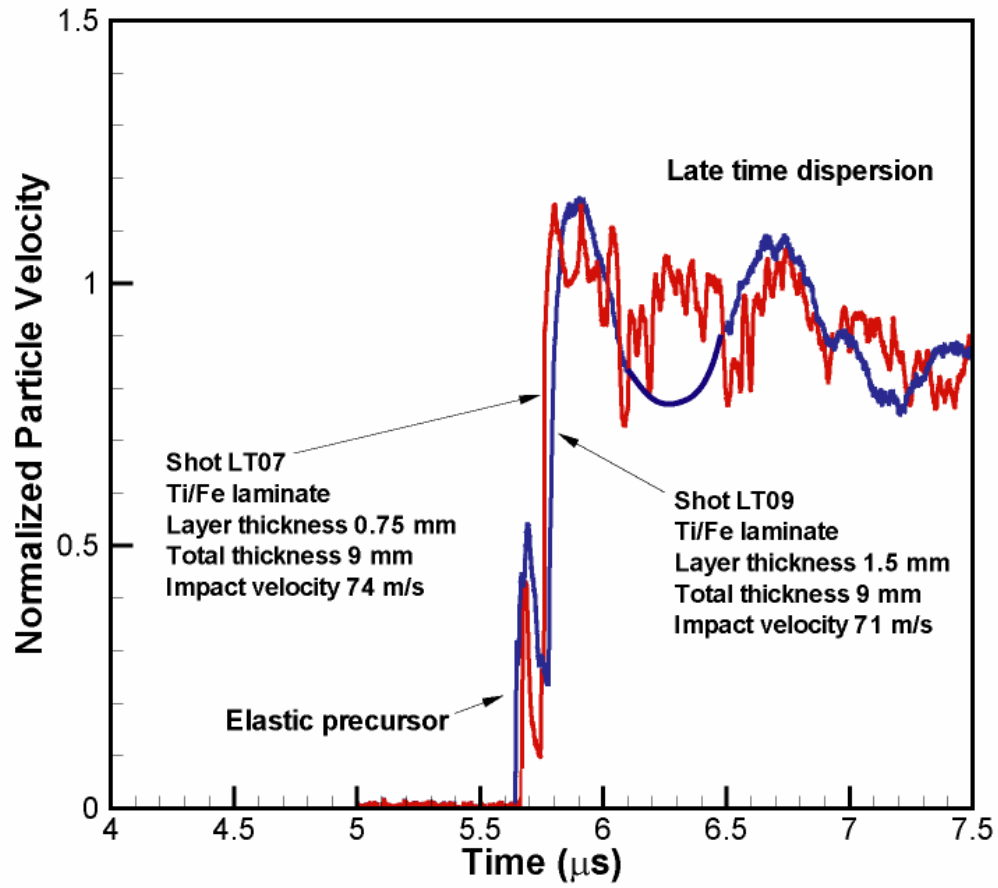


Figure 3.8: Results from plate impact experiments on Ti-Fe laminates, LT07 and LT09, showing the effects of layer thickness on elastic precursor decay and late time dispersion.

The objective of the third series of experiments was to understand the effects of impedance mismatch, density of interfaces, and the material inelasticity on precursor decay and late-time dispersion. These experiments were conducted by employing Al-PC laminates. A schematic of the laminate architectures used in the series of experiments is shown in Figure 3.9. For shot LT23 the thickness of the Al and PC layers were 0.75 mm and 0.8 mm, respectively. The total number of layers was 4 with an overall thickness of 3.1 mm. The laminate was sandwiched between impedance matched 7075-T6 Al front and rear target plates. Moreover, the layers in the laminate were bonded to each other by using a low viscosity epoxy. For shot LT24 the thickness of the Al and PC layers was 0.25 mm. A total of 12 Al and PC layers were used to make the laminate, with a total laminate thickness of 3.0 mm. Again, for this experiment the laminate was sandwiched between impedance matched 7075-T6 Al front and rear target plates. Also, the layers in the laminate were bonded to each other with a low viscosity epoxy.

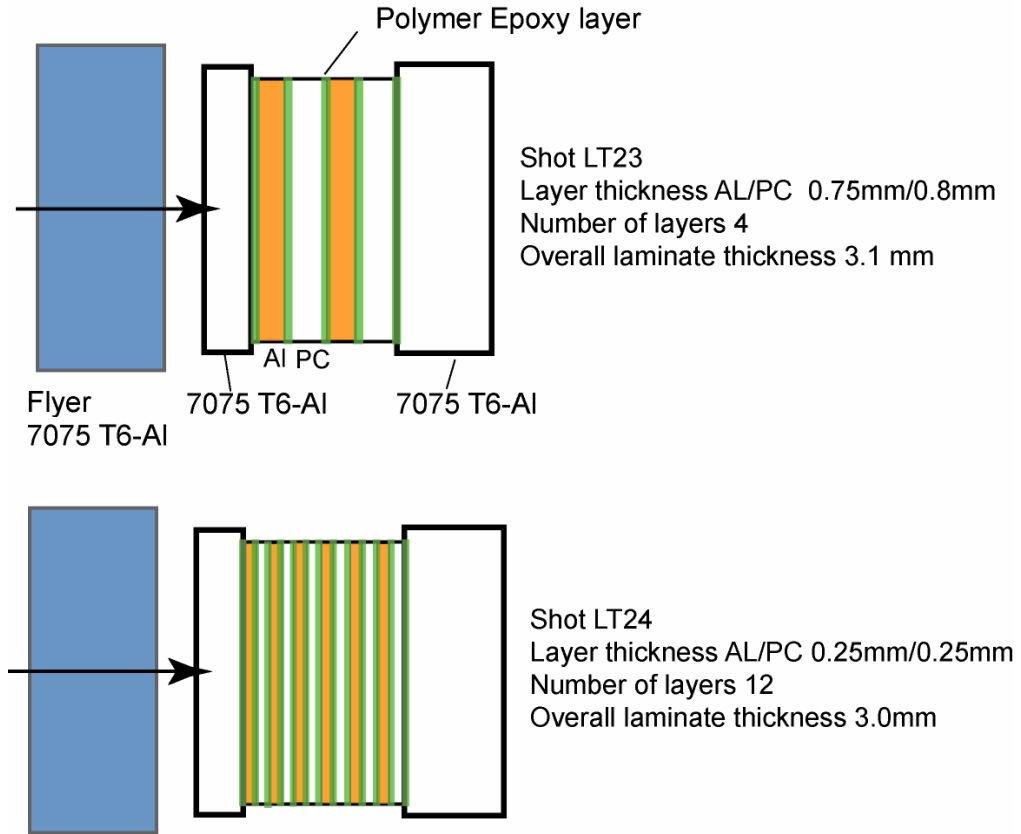


Figure 3.9: Schematic of the laminate architecture employed to conduct the third series of plate-impact experiments.

Figure 3.10 and Figure 3.11 show the experimental results obtained from the two experiments on the Al-PC laminates. The impact velocities for Shots LT23 and LT24 were 84 m/s and 82 m/s respectively. For both experiments the flyer plate and the front and rear target plates are made from 7075-T6 Al alloy. The relatively large thickness of the flyer plate precludes any unloading waves from the back surface of the flyer plate to reach the flyer-target interface during the

window time of the experiment. In both plots the abscissa represents the time after impact while the two ordinates represent the normalized particle velocity measured at the free surface of the target plate and the normalized stress obtained by using Eq (2.29), respectively. It is interesting to note that the velocity versus time profiles obtained in the experiments are much smoother when compared with the particle velocity profiles obtained for the elastic-elastic (Fe-Ti) bilaminates. In the case of the Fe-Ti bilaminates a high frequency oscillatory signal was observed to be riding on top of the particle-velocity profiles. The presence of air gaps of several microns between the Fe-Ti layers are understood to be the origin of the high frequency oscillations observed in the signal. The reason for the absence of these oscillations in the Al-PC laminates is understood to be due to the use of epoxy in preparing the Al-PC laminates. The use of epoxy to bond the individual layers precludes any air gaps in between the layers. The parameters of the visco-elastic material model for PC that are used in the simulations correspond to nearly elastic behavior, i.e. $\gamma \approx 1$. It is interesting to note that the predicted and the experimentally observed arrival

times of the late-time dispersive waves are very close. Also, the frequency of the oscillations contained in the late-time dispersive wave corresponds closely to the analytical predictions with $\gamma \approx 1$ for PC. It should be noted that the experimental results are for particle velocity on the rear surface of the target plate while the analytical solutions are for stress (shown on the Y2 axis).

It is also interesting to compare the experimental results for Shot LT06 and Shot LT23. For Shot LT06 experiments were conducted using Fe-Ti bilaminates with layer thickness of 0.75 mm. The total laminate thickness was 3 mm. For Shot LT23 the laminate comprises Al-PC layers with layer thickness of 0.75 mm and an overall laminate thickness 3 mm. The difference between the two architectures is the impedance mismatch at the layer interface. For the case of Al-PC laminates the impedance mismatch is 8.3, while for the case of the Fe-Ti laminates the impedance mismatch is 1.75. It is interesting to note the relatively long rise-time associated with the late-time dispersive waves for the case of the higher impedance mismatch Al-PC laminates. Also, as predicted by the

analytical results, the frequency of the late-time dispersive waves is much smaller for the case of the higher impedance Al-PC laminates as compared with the Fe-Ti laminates.

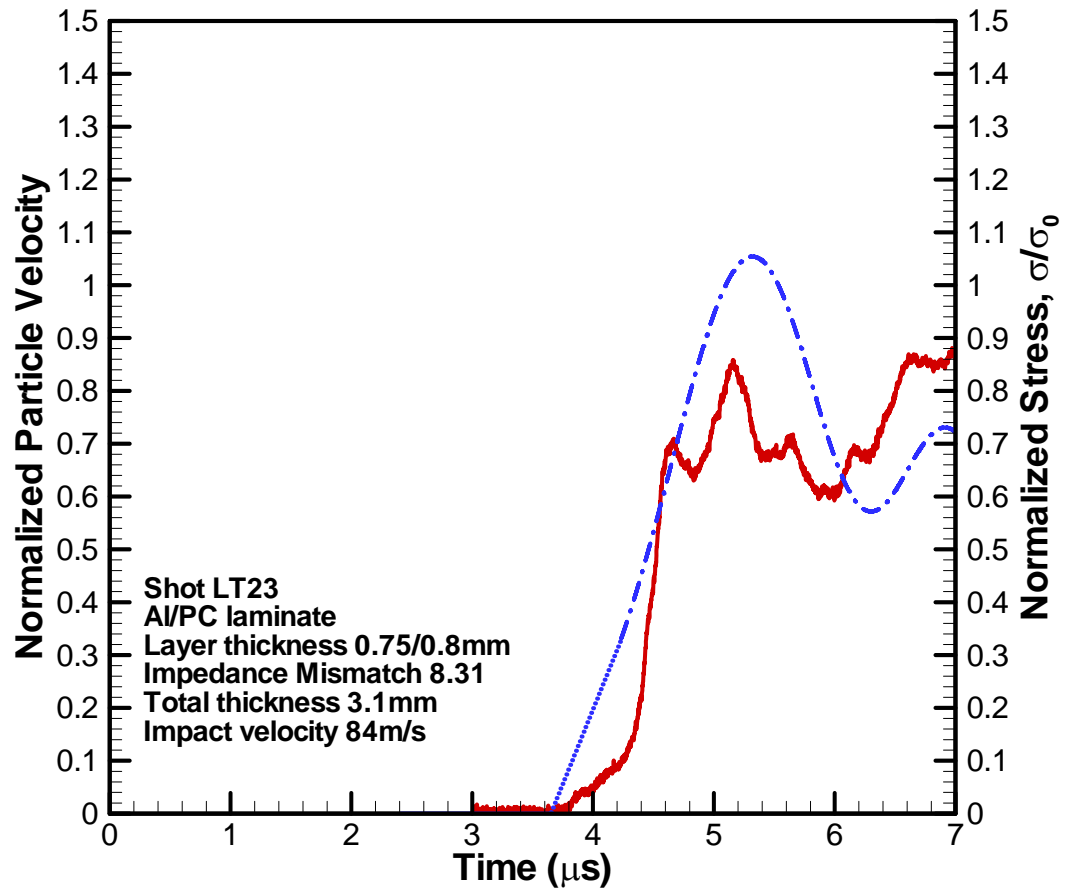


Figure 3.10: Results from plate impact experiments on Al-PC laminates showing the late time dispersion wave.

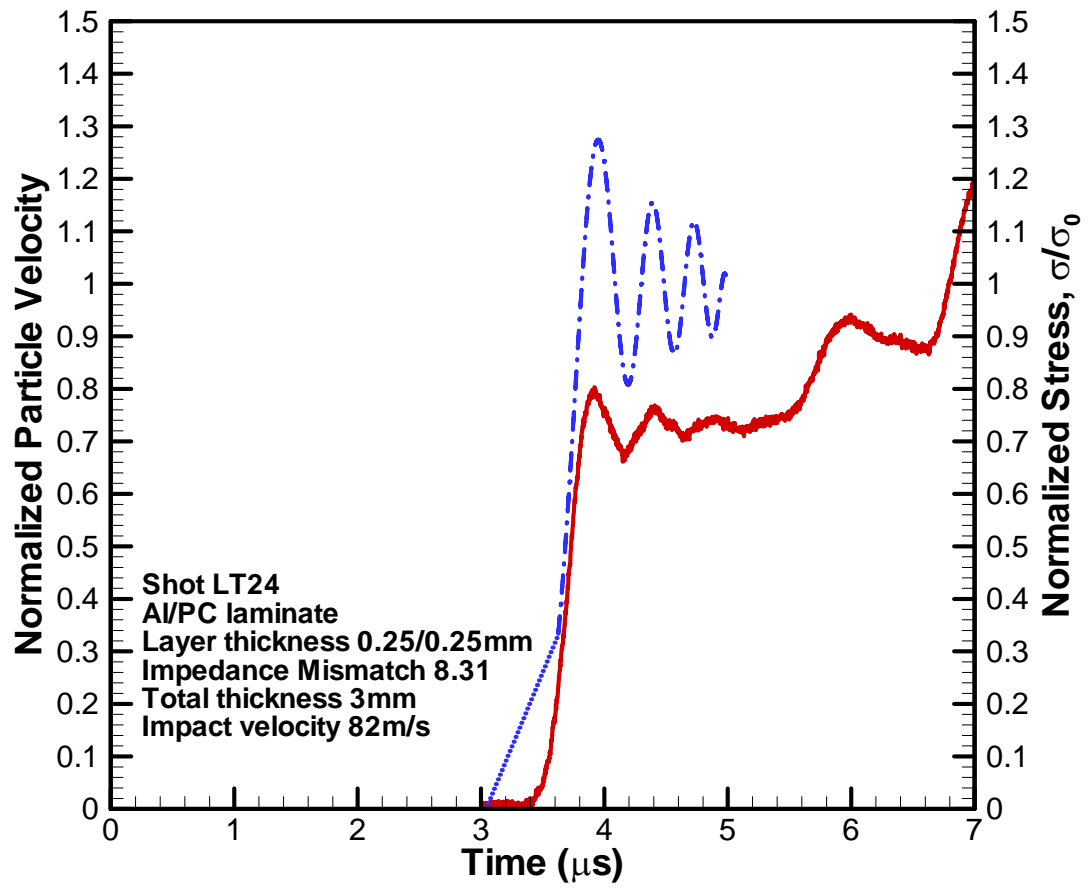


Figure 3.11: Results from plate impact experiments on Al-PC laminates showing the late-time dispersion wave.

The fourth series of experiments was conducted to understand wave propagation in elastic-viscoelastic laminates confined by high impedance elastic plates. The high impedance plates result in reverberation of stress waves within the relatively low impedance sandwiched laminate resulting in an incremental build up of stress with each reverberation of stress wave. In this series of experiments Al-PC bilaminates were utilized. The thickness of each Al and PC layer is 0.125 mm. In the first experiment the laminate comprised 4 alternating layers of Al and PC with a total laminate thickness of 0.5 mm. For the second experiment 8 alternating layers of Al and PC with a total laminate thickness of 1.0 mm were utilized. For the third experiment 12 alternating layers of Al and PC with a total laminate thickness of 1.5 mm were utilized. In each case the Al-PC laminate was sandwiched by high impedance steel plates. A schematic of the experimental configurations for this series of experiments is shown in Figure 3.12. Figure 3.13 shows experimental results on the Al-PC laminates. The impact velocities for the three experiments, LT19, LT18, and LT20 were 81 m/s, 74 m/s and 75 m/s, respectively. The abscissa shows the time after impact while the

ordinate shows the normalized particle velocity. It is seen that in each case, the normalized particle velocity (or the stress) builds up to the impact velocity in a series of steps. Each step represents one reverberation of the stress wave between the CH steel plates. As expected the time duration of each step is longest for the laminate with the greatest thickness, i.e. Shot LT18 with 12 alternating layers of PC and Al. Also, it is interesting to note the oscillatory nature of the particle velocity profile at each loading step. The sudden increase in particle velocity at approximately $8 \mu s$ is consistent with the arrival of the release wave from the lateral boundary. Full simulations of the experiments utilizing finite element methods are required to adequately model the observed velocity versus time profiles for the three sandwiched laminates.

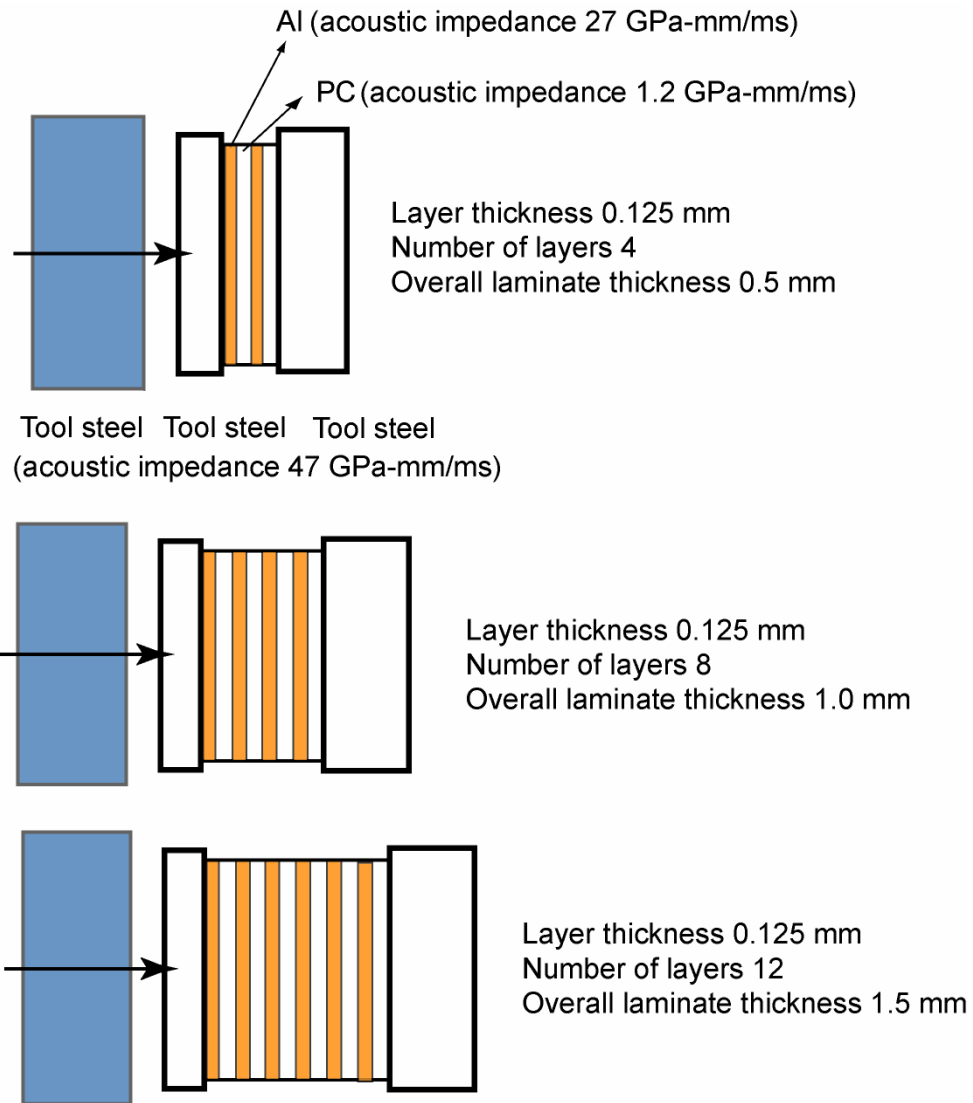


Figure 3.12: Schematic of the laminate architecture employed to conduct the fourth series of plate-impact experiments.

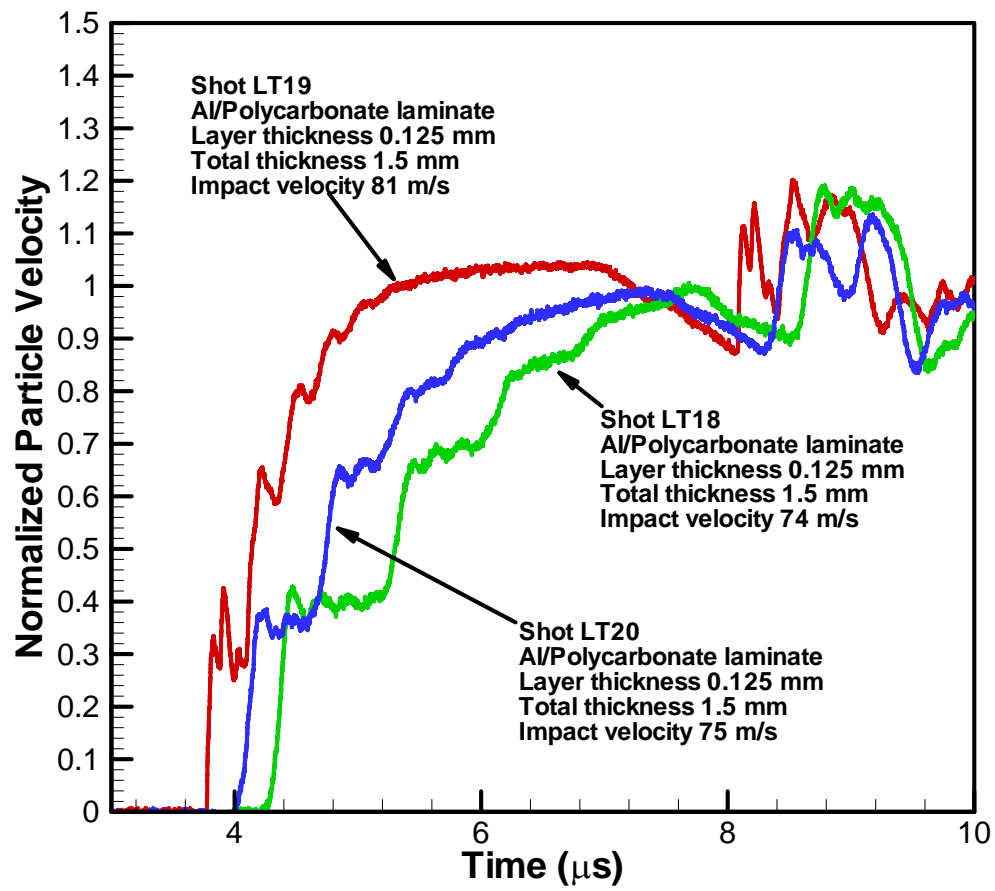


Figure 3.13: Results from plate impact experiments on thin Al-PC laminates sandwiched between two hard CH tool steel plates.

3.4 SUMMARY

In the present study normal plate-impact experiments are conducted on 2-D layered material targets to understand the role of material architecture and material inelasticity in governing the elastic precursor decay and late-time wave dispersion. The particle velocity at the free surface of the target plate is measured by using a multi-beam VALYN VISAR. In order to understand the effects of layer thickness and the distance of wave propagation on elastic precursor decay and late-time dispersion several different targets with various layer and target thicknesses are employed. Moreover, in order to understand the effects of material inelasticity both elastic-elastic and elastic-viscoelastic bilaminates are utilized.

The results of these experiments are interpreted by using asymptotic techniques to analyze propagation of acceleration waves in 2-D layered material systems as discussed in chapter 2. The results of the study indicate that the structure of acceleration waves is strongly influenced by impedance mismatch of the layers

constituting the laminates, density of interfaces, distance of wave propagation, and the material inelasticity. The speed of the elastic precursor is independent of the impedance mismatch of the individual laminae constituting the bilaminates and is equal to the average wave speed within the bilaminates. The speed of late-time dispersion wave is observed to decrease with an increase in impedance mismatch; however, it is found to be independent of the density of interfaces, i.e. the number of layers in a given thickness laminate. The decay in elastic precursor is observed to increase with an increase in impedance mismatch, the density of interfaces, and the distance of wave propagation. The rise-time of the late-time dispersion wave increases with an increase in impedance mismatch; however, it is observed to decrease with an increase in the density of interfaces. The frequency of oscillations of the late-time dispersive wave is observed to decrease with an increase in impedance mismatch; however, it is observed to increase with an increase in the density of interfaces.

REFERENCES

- Achenbach J. D., 1973. Wave Propagation in Elastic Solids. North-Holland, Amsterdam.
- Barker L. M., Lundergan C. D., Chen P. J. and Gurtin M. E., 1974. Nonlinear viscoelasticity and the evolution of stress waves in laminated composites: a comparison of theory and experiment. *Journal of Applied Mechanics* 41, 1025-.
- Benson D. J. and Nesterenko V. F., 2001. Anomalous Decay of shock impulses in laminated composites. *Journal of Applied Physics* 89(7), 3622-3626.
- Betheney W., DeLuca E., Prifti J. and Chou S. C., 1998. Ballistic impact damage of S2-glass reinforced plastic structural armor. *Composites Science and Technology* 58, 1453-1461.
- Cerrillo M V, 1950. Technical Report No.55, 2a, Research Laboratory of Electronics MIT, Cambridge, MA.
- Chen C. C. and Clifton R. J., 1974. Asymptotic Solutions for Wave Propagation in Elastic and Viscoelastic Bilaminates. In: *Developments in Mechanics, Proceedings of the 14th Mid-Eastern Mechanics Conference*: 26, 8., pp. 399-417.
- Clifton R. J., 1972. Solution of wave problems in inelastic materials. In: *Summer Course on Dynamics of Inelastic Materials* Jablonna, Poland.
- Fink B., 2000. Performance metrics for composite integral armor. *Journal of Thermoplastic Composite Materials* 13(5), 417-431.
- Hegemier G. A., 1972. On a theory of interacting continua for wave propagation in composites. In: *Dynamics of Composite Materials*. ed(s): E. H. Lee. ASME, pp. 70-121.
- Hemsing W. F., 1979. Velocity sensing interferometer (VISAR) modification. *Review of Scientific Instrumentation* 50(1), 73-78.

Hill W H and Shimmin K D, 1961. Elevated Temperature Dynamic Elastic Moduli of Various Metallic Materials. WADD Twchnical report 60-438. Wright-Patterson Air force base, Ohio.

Laptev V. I. and Trishin Y. A., 1976. The increase of velocity and pressure under impact on inhomogeneous target. Journal of Applied Mechanics and Technical Physics, 837-841.

Lundergan C D and Drumheller D S, 1971. Dispersion of shock waves in composite materials. Shock Waves and the Mechanical Properties of Solids. Syracuse University Press, New York, p 141-.

Nesterenko V F, Fomin V M and Cheskidov P A, 1983. Attenuation of strong shock waves in laminate materials. Nonlinear Deformation Waves. Springer Verlag, Berlin, pp 191-7.

Nesterenko V. F., Fomin V. M. and Cheskidov P. A., 1984. Damping of strong waves in laminar materials. Journal of Applied Mechanics and Technical Physics, 567-575.

Oved Y., Luttwak G. E. and Rosenberg Z., 1978. Shock wave propagation in layered composites. Journal of Composite Materials 12, 84-.

Peck J. C. and Gurtman G. A., 1969. Dispersive pulse propagation parallel to the interfaces of a laminated composite. Journal of Applied Mechanics, 479-484.

Sherby O. D., Lee S., Koch R., Sumi T. and Wolfenstine J., 1990. Multilayered composites based on ultrahigh carbon steel and brass. Materials and Manufacturing Processes 5, 363-376.

Stern M., Bedford A. and Yew C. H., 1970. Wave propagation in viscoelastic laminates. Journal of Applied Mechanics 70-WA/APM-40, 1-7.

Sun C.-T., Achenbach J. D. and Herrmann G., 1968. Time-harmonic waves in a stratified medium propagating in the direction of the layering. Journal of Applied Mechanics, 408-411.

Sve C., 1971. Thermo-elastic Waves in a Periodically Laminated Medium. International Journal of Solids Structures, 7, 1363-1373.

Sve C., 1972. Stress wave attenuation in composite materials. Journal of Applied Mechanics, 1151-1153.

Vaidya U. K., Hosur M. V., Kumar P., Mahfuz H., Haque A. and Jeelani S., 1999. Impact damage resistance of innovative functional sandwich composites. In: ASME 1999 Mechanics and Materials Conference Blacksburg, VA.

Zhuang S, 2002. Shock Wave Propagation in Periodically layered composites. PhD Dissertation, California Institute of Technology, Pasadena, CA.

Chapter 3

STRUCTURE OF WEAK SHOCK WAVES IN 2-D LAYERED HETEROGENEOUS MATERIAL SYSTEMS

3.1 Introduction

In view of the scientific and technological importance of heterogeneous materials in shock related applications and our current incomplete state of understanding of their performance under impact loading conditions, integrated experimental-analytical research is being conducted. In chapter 2, asymptotic solutions were established to explore the two-wave structure for selected elastic/elastic and elastic/visco-elastic bilaminate materials. The effects of layer density, impedance mismatch, propagation distance, and material in-elasticity to the elastic precursor and late-time oscillations were discussed. In this chapter, experiment results were presented to compare with the asymptotic solutions in chapter 2. Iron/titanium and aluminum/polycarbonate bilaminates were shock compressed to between 0.8

to 1.9 GPa and the free surface velocities were recorded using VISAR system.

The observed elastic precursors and late-time wave profiles showed good agreements with the asymptotic solutions. The effects of material in-elasticity were found to affect the two-wave structure dramatically.

3.2 Experimental Configuration

The experiments described in this paper are designed to illustrate the effect of impedance mismatch, layer thickness, and material inelasticity on the elastic precursor decay and late-time dispersion characteristics of weak shock waves in 2-D laminates. In view of this, normal plate impact experiments are conducted on laminates comprising alternating Ti-Fe (elastic-elastic) and the Al-PC (elastic-viscoelastic) layers. The experiments are conducted using the 82.5mm single-stage gas-gun at Case Western Reserve University. The experiments involve the impact of an elastic flyer plate with a target assembly at normal incidence. The target assembly is a sandwich in which the laminate under investigation is confined between two metal plates that remain elastic under impact. Impact takes place on the front target plate; the waves transmitted through the layered

specimen are monitored on the free surface of the rear target plate by means of laser interferometer. The measured motion at the free surface of the rear target plate and the known elastic properties of the front and the rear target plates are used to obtain the wave characteristics as the shock wave propagates through the layered specimen.

The schematic of the plate-impact experimental configuration is shown in Figure 3.1. A fiberglass projectile carrying the flyer plate is accelerated down the gun barrel by means of compressed nitrogen gas. The rear end of the projectile has sealing O-ring and a plastic (Teflon) key that slides in a key-way inside the gun barrel to prevent any rotation of the projectile. In order to reduce the possibility of an air cushion between the flyer and target plates, impact takes place in a target chamber that has been evacuated to 50 μm of Hg prior to impact. A laser based optical system utilizing a UNIPHASE Helium-Neon 5mW laser (Model 1125p) and a high frequency photo-diode is used to measure the velocity of the projectile. To ensure the generation of plane waves with wave-front sufficiently

parallel to the impact face, the flyer and the target plates are carefully aligned to be parallel to within 2×10^{-5} radians by using an optical alignment scheme. The actual tilt between the two plates is measured by recording the times at which four, isolated, voltage-biased pins, that are flush with the surface of the target plate, are shorted to ground. The acceptance level of the experiments is of the order of 0.5 mrad. A VALYN VISAR laser interferometer is used to measure the history of the normal particle velocity at the rear surface of the target plate. A COHERENT VERDI 5 Watt solid-state diode-pumped frequency doubled Nd:YVO₄ CW laser with wavelength of 532 nm is used to provide a coherent monochromatic light source.

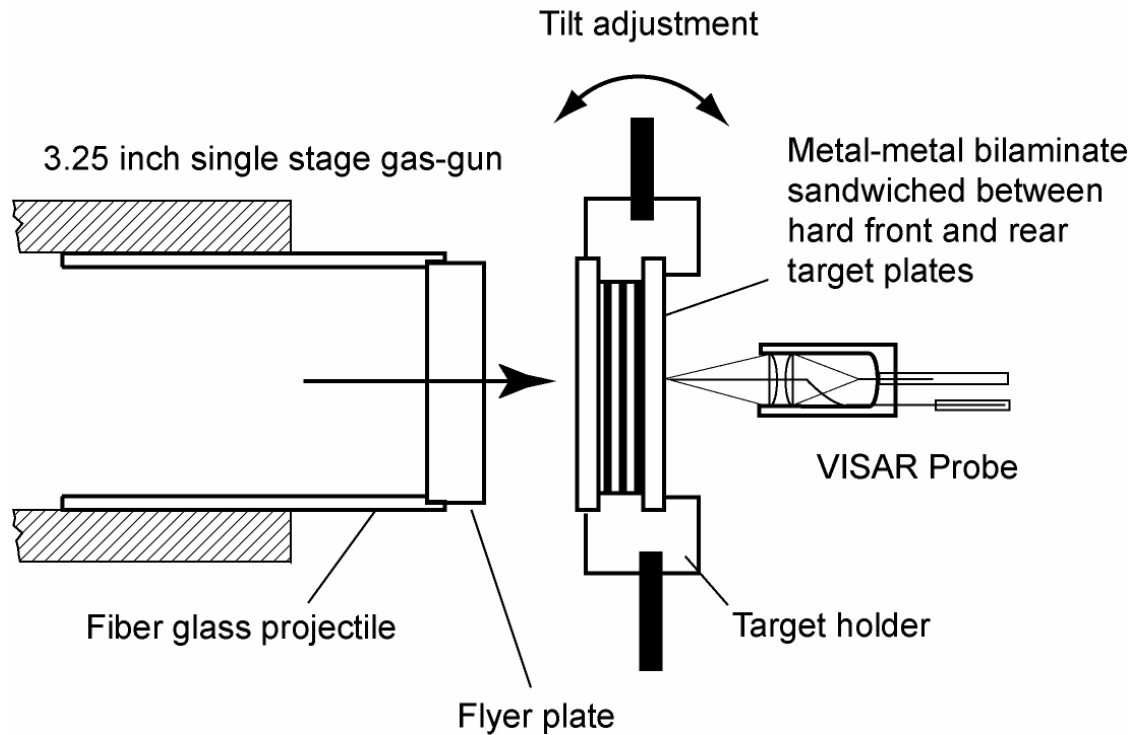


Figure 3.1: Schematic of the plate impact configuration employed in the present investigation. The layered specimen is sandwiched between two hard plates of the target assembly.

The schematic of the light path of the laser interferometer is shown in Figure 3.2.

The VALYN VISAR is based on the wide angle Michelson interferometer (WAMI) concept and capable of velocity measurements from either a spectrally or diffusely reflecting specimen surface. Using a laser light coupler, the light from the laser is coupled into an optical fiber of diameter $125\ \mu m$ which directs light onto the surface of the specimen. By an optical assembly called the optical fiber

probe, the reflected light is collected and coupled into an out-going fiber which has a diameter of $300\text{ }\mu\text{m}$. The laser light from the out-going fiber, which contains the Doppler shift effect due to the motion of the surface under shock loading, is collimated and then directed into the VISAR optical system to extract the interferometer information of particle velocity. In order to monitor any intensity change of the reflected laser beam resulting from self illumination due to shock compression, part of the light is sampled by a beam sampler and directed to a photomultiplier tube, which converts the light signal into an electric signal to be recorded on the oscilloscope. The 50/50 large beam splitter evenly splits the light from the main beam into two; one is sent to a PZAT mirror of the interferometer, while the other passes through a $1/8$ wave plate, etalon and then is returned by a mirror. One half of the returned light passing through the 50/50 large beam splitter is combined with the reflected part of the returned beam from PZAT mirror to form interference fringes. The other half of the returned light from the PZAT mirror is combined with the beam passing through the 50/50 large beam splitter and reflected from the mirror to form interference fringes.

The alignment of the interfering laser beams which give rise to the interference fringe pattern is optimized by monitoring the bull's eyes pattern. Each interference pattern then passes through two separate polarizing beam splitters, separating the S and P components of the laser light, which have a 90° phase angle difference due to the retardation of a $1/8$ wave plate to the phase angle of the P component of light. In order to increase the signal to noise ratios the two s -polarized beams and the two p -polarized beams, which are both 180° out of phase, are subtracted (Hemsing, 1979). This feature known as push-pull significantly reduces the noise level introduced by incoherent light entering the interferometer. The subtracted S and P components of the interference fringes are directed into two photomultiplier tubes. Separately recording the S and the P fringes (quadrature coding) eliminates the ambiguity in the sign of the acceleration and improves accuracy when data reduction is performed using the high resolution regimes of the traces. The electrical signals from the photomultipliers are amplified by 1.2 GHz bandwidth amplifiers before being sent to 1 GHz digital oscilloscope for recording.

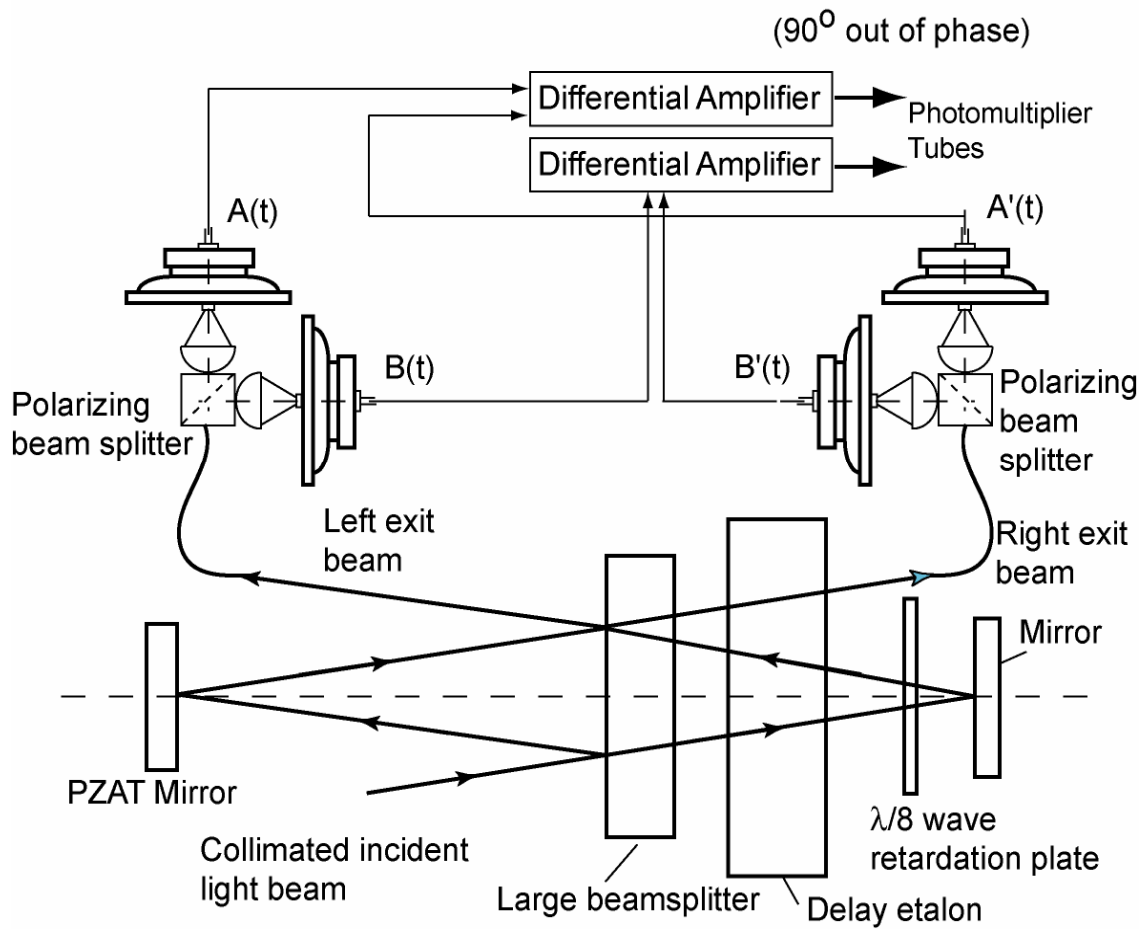


Figure 3.2 : Schematic showing the light path in a VISAR interferometer.

Figure 3.3 shows a typical oscillograph of the recorded VISAR signal (Shot LT24). The resonant oscillations induced by the multiple reflections of the shock wave at the material interfaces are clearly seen in the record. Part of the data reduction procedure involves plotting the amplitudes of the two fringe records

against each other at each data reading time, thereby forming a Lissajous plot of the data. This plot for Shot LT24 is shown in Figure 3.4. The Lissajous plot allows the user to judge whether certain corrections to the input data are warranted. The judgment is based in part on how nearly the Lissajous plot resembles a perfect circle, which would be the result if the fringe amplitudes of the two data sets were equal, and if the phase difference were 90 degrees. Judging from Figure 3.4, the Lissajous of this experiment is a near perfect circle, which confirms the high quality of the interference signal.

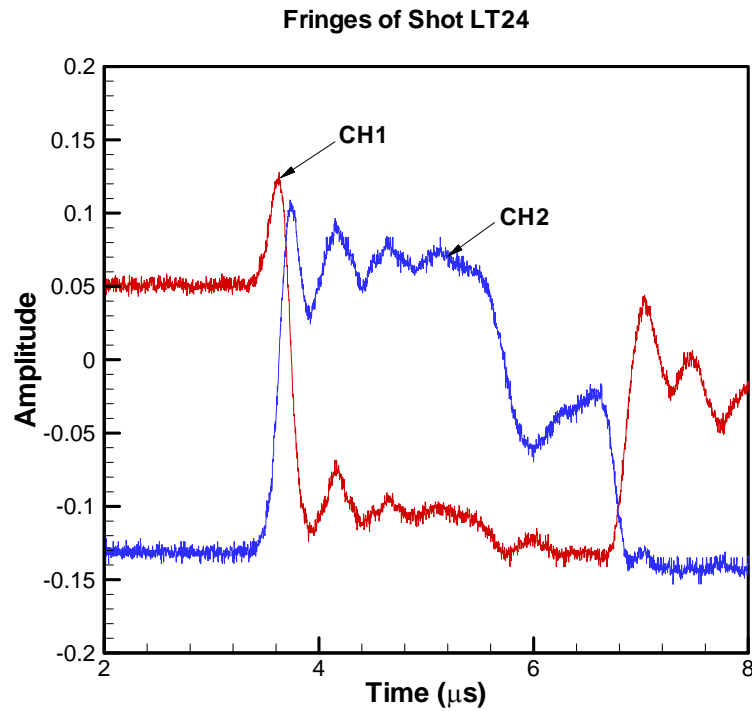


Figure 3.3: Oscillographs of VISAR signals for Shot LT24.

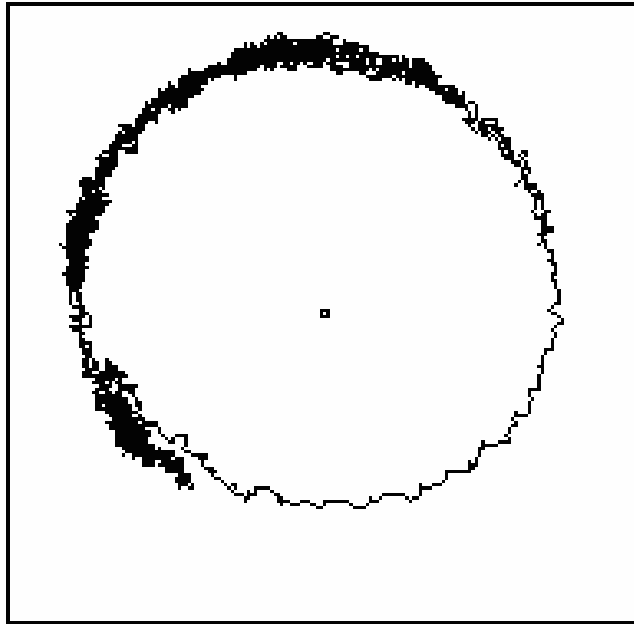


Figure 3.4: Lisajous showing the amplitude of the VISAR fringe records plotted against each other at each time data.

3.3 Results and Discussion

In the present study four series of experiments were designed and conducted. The first series of experiments involved the investigation of the effect of distance of propagation on elastic precursor decay and the late-time dispersion. The experiments were conducted using Fe-Ti laminates. The thickness of each Fe and Ti layer in the laminate was 0.75 mm. A schematic of the experimental configuration is shown in Figure 3.5. In the first experiment (Shot LT07) 12 alternating layers of Fe and Ti with a total laminate thickness of 9 mm were utilized. In the second experiment (Shot LT06) 4 alternating layers of Fe and Ti with a total laminate thickness of 3 mm were utilized. For both experiments the flyer plate was made from hardened CH tool-steel, and was approximately 16 mm in thickness. The thicknesses of the front and rear CH tool-steel plates that sandwich the laminate were 8.65 mm and 5.14 mm, respectively. The relatively large thickness of the flyer plate precludes any unloading waves from the back surface of the flyer plate to reach the flyer/target interface during the total window time of the experiment.

Figure 3.6 shows experimental results on the Ti-Fe laminates. The impact velocities for Shots LT07 and LT06 were 74 m/s and 79 m/s, respectively. In the figure the abscissa represents the time after impact while the ordinate represents the normalized particle velocity measured at the free surface of the target plate. For both experiments the impact velocity is used as the normalization factor for the y axis. The elastic precursor arrives at the free surface of the target plate at approximately $4.2\mu s$ for Shot LT06 and at $5.65\mu s$ for Shot LT07. The later arrival of the elastic precursor in the case of Shot LT07 is consistent with the larger thickness of the laminate employed in Shot LT07. The precursor decay is much higher for Shot LT07 indicating that the decay increases with distance of propagation. The late-time dispersion arrives after the arrival of the elastic precursor. The highest particle-velocity attained observed in the measured wave profiles is approximately 1.2 times the impact velocity and the late-time dispersive wave is observed to oscillate about a mean level 1.0. As expected, the frequency of the oscillations is not affected by the distance the wave propagates into the laminates and is essentially the same for the two experiments. Also, the

amplitude of these oscillations is observed to decay with time. It is interesting to note that the general characteristics of the wave structure are strikingly similar to the analytical predictions for wave front and late time dispersive waves as shown in chapter 2.

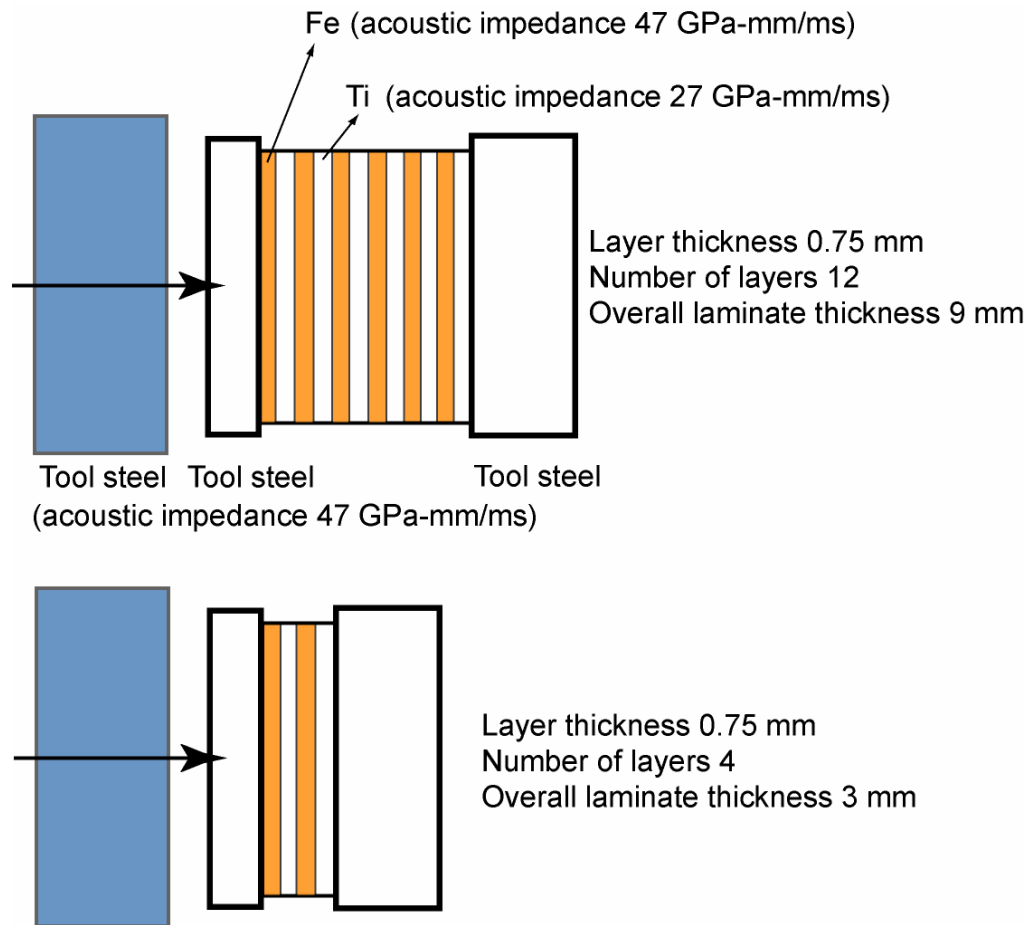


Figure 3.5: Schematic of the laminate architecture employed to conduct the first series of plate impact experiments.

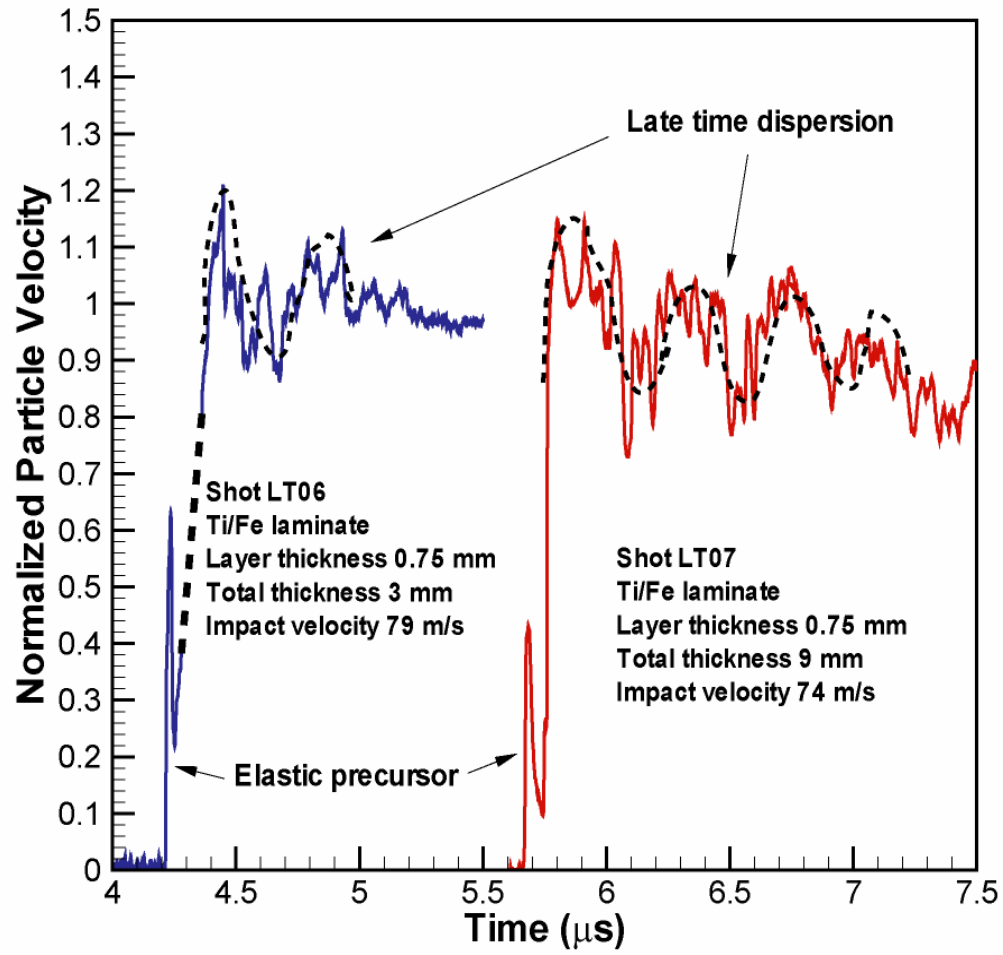


Figure 3.6: Results of plate impact experiments on Fe-Ti laminates showing the effect of distance of propagation on precursor decay and late time dispersion.

The second series of experiments was conducted to understand the effects of density of interfaces on the elastic precursor decay and late time dispersion. Again, in this series of experiments Fe-Ti laminates were utilized. A schematic of the layer architectures employed in this series of experiments is shown in Figure 3.7. For the two experiments the overall thickness of the laminate was 9 mm. In the first experiment (LT07) 12 alternating layers of Fe and Ti with an individual layer thickness of 0.75 mm were utilized. In the second experiment 6 alternating layers of Fe and Ti with an individual layer thickness of 1.5 mm were utilized. Figure 3.8 shows the results of the two experiments conducted in this series. The impact velocities for Shot LT07 and LT09 were 74 m/s and 71m/s, respectively. It can be seen that the precursor decay for Shot LT07 is much greater than that obtained for Shot LT09. Moreover, the rise-time associated with the late-time dispersive wave is shorter for Shot LT07 when compared with Shot LT09. The frequency of oscillations in the late-time dispersive wave is higher for the Shot LT07 when compared with Shot LT09. These results are all consistent with the analytical results shown in chapter 2 for Fe-Ti laminates.

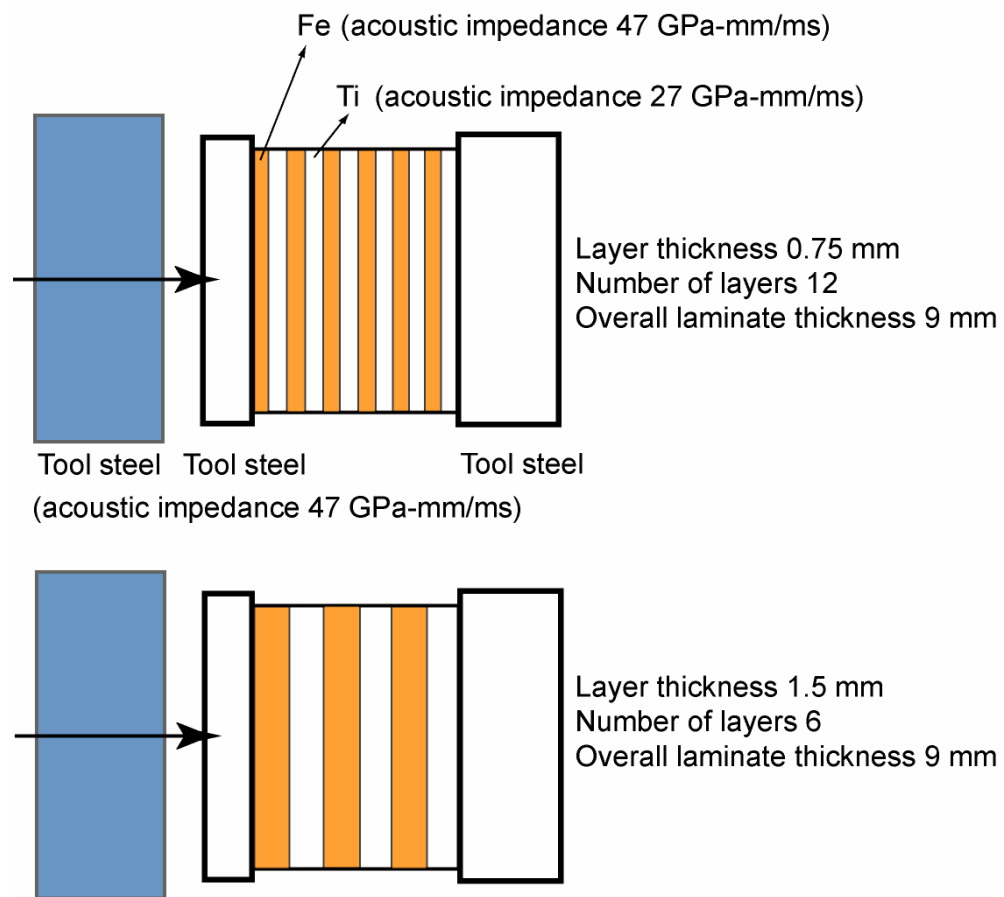


Figure 3.7: Schematic of the laminate architecture employed to conduct the second series of plate-impact experiments.

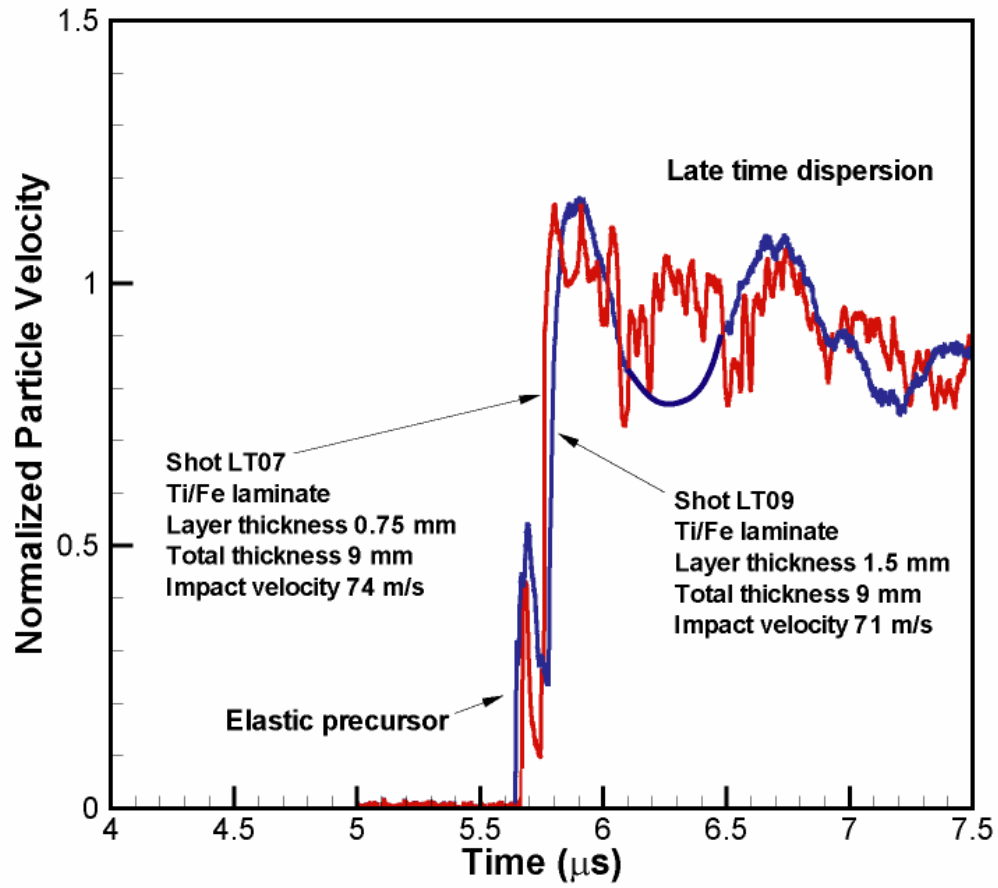


Figure 3.8: Results from plate impact experiments on Ti-Fe laminates, LT07 and LT09, showing the effects of layer thickness on elastic precursor decay and late time dispersion.

The objective of the third series of experiments was to understand the effects of impedance mismatch, density of interfaces, and the material inelasticity on precursor decay and late-time dispersion. These experiments were conducted by employing Al-PC laminates. A schematic of the laminate architectures used in the series of experiments is shown in Figure 3.9. For shot LT23 the thickness of the Al and PC layers were 0.75 mm and 0.8 mm, respectively. The total number of layers was 4 with an overall thickness of 3.1 mm. The laminate was sandwiched between impedance matched 7075-T6 Al front and rear target plates. Moreover, the layers in the laminate were bonded to each other by using a low viscosity epoxy. For shot LT24 the thickness of the Al and PC layers was 0.25 mm. A total of 12 Al and PC layers were used to make the laminate, with a total laminate thickness of 3.0 mm. Again, for this experiment the laminate was sandwiched between impedance matched 7075-T6 Al front and rear target plates. Also, the layers in the laminate were bonded to each other with a low viscosity epoxy.

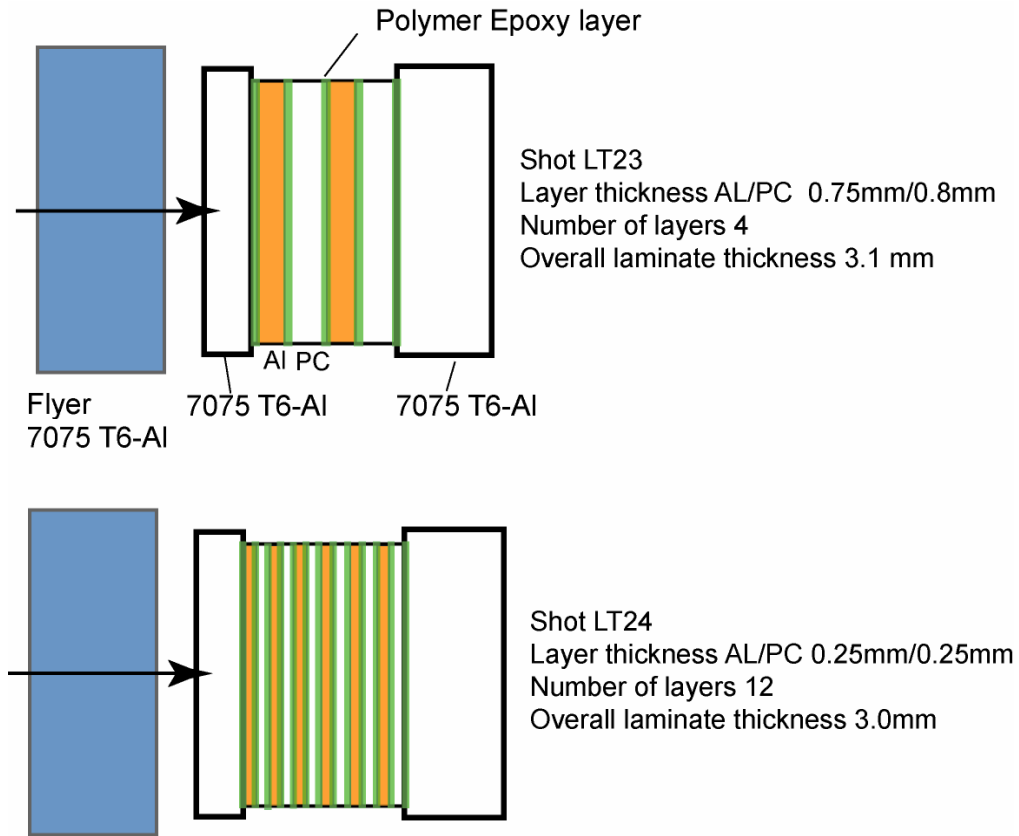


Figure 3.9: Schematic of the laminate architecture employed to conduct the third series of plate-impact experiments.

Figure 3.10 and Figure 3.11 show the experimental results obtained from the two experiments on the Al-PC laminates. The impact velocities for Shots LT23 and LT24 were 84 m/s and 82 m/s respectively. For both experiments the flyer plate and the front and rear target plates are made from 7075-T6 Al alloy. The relatively large thickness of the flyer plate precludes any unloading waves from the back surface of the flyer plate to reach the flyer-target interface during the

window time of the experiment. In both plots the abscissa represents the time after impact while the two ordinates represent the normalized particle velocity measured at the free surface of the target plate and the normalized stress obtained by using Eq (2.29), respectively. It is interesting to note that the velocity versus time profiles obtained in the experiments are much smoother when compared with the particle velocity profiles obtained for the elastic-elastic (Fe-Ti) bilaminates. In the case of the Fe-Ti bilaminates a high frequency oscillatory signal was observed to be riding on top of the particle-velocity profiles. The presence of air gaps of several microns between the Fe-Ti layers are understood to be the origin of the high frequency oscillations observed in the signal. The reason for the absence of these oscillations in the Al-PC laminates is understood to be due to the use of epoxy in preparing the Al-PC laminates. The use of epoxy to bond the individual layers precludes any air gaps in between the layers. The parameters of the visco-elastic material model for PC that are used in the simulations correspond to nearly elastic behavior, i.e. $\gamma \approx 1$. It is interesting to note that the predicted and the experimentally observed arrival

times of the late-time dispersive waves are very close. Also, the frequency of the oscillations contained in the late-time dispersive wave corresponds closely to the analytical predictions with $\gamma \approx 1$ for PC. It should be noted that the experimental results are for particle velocity on the rear surface of the target plate while the analytical solutions are for stress (shown on the Y2 axis).

It is also interesting to compare the experimental results for Shot LT06 and Shot LT23. For Shot LT06 experiments were conducted using Fe-Ti bilaminates with layer thickness of 0.75 mm. The total laminate thickness was 3 mm. For Shot LT23 the laminate comprises Al-PC layers with layer thickness of 0.75 mm and an overall laminate thickness 3 mm. The difference between the two architectures is the impedance mismatch at the layer interface. For the case of Al-PC laminates the impedance mismatch is 8.3, while for the case of the Fe-Ti laminates the impedance mismatch is 1.75. It is interesting to note the relatively long rise-time associated with the late-time dispersive waves for the case of the higher impedance mismatch Al-PC laminates. Also, as predicted by the

analytical results, the frequency of the late-time dispersive waves is much smaller for the case of the higher impedance Al-PC laminates as compared with the Fe-Ti laminates.

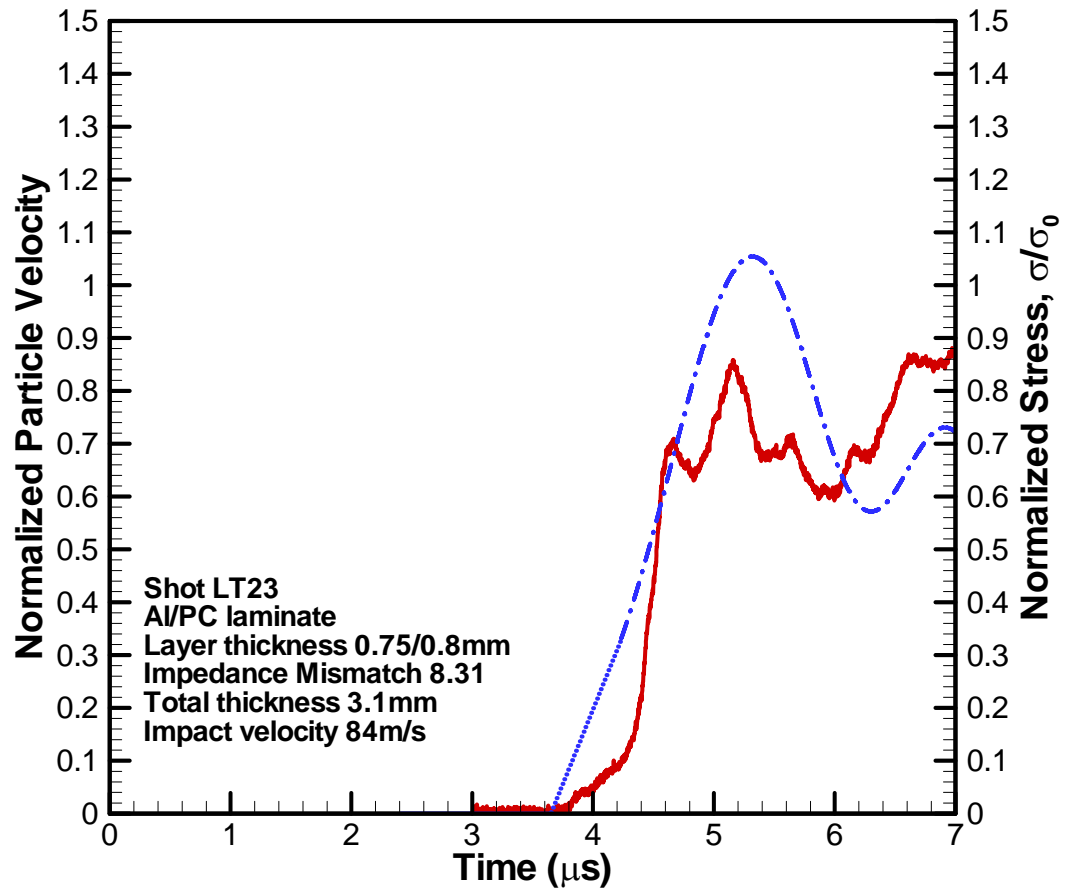


Figure 3.10: Results from plate impact experiments on Al-PC laminates showing the late time dispersion wave.

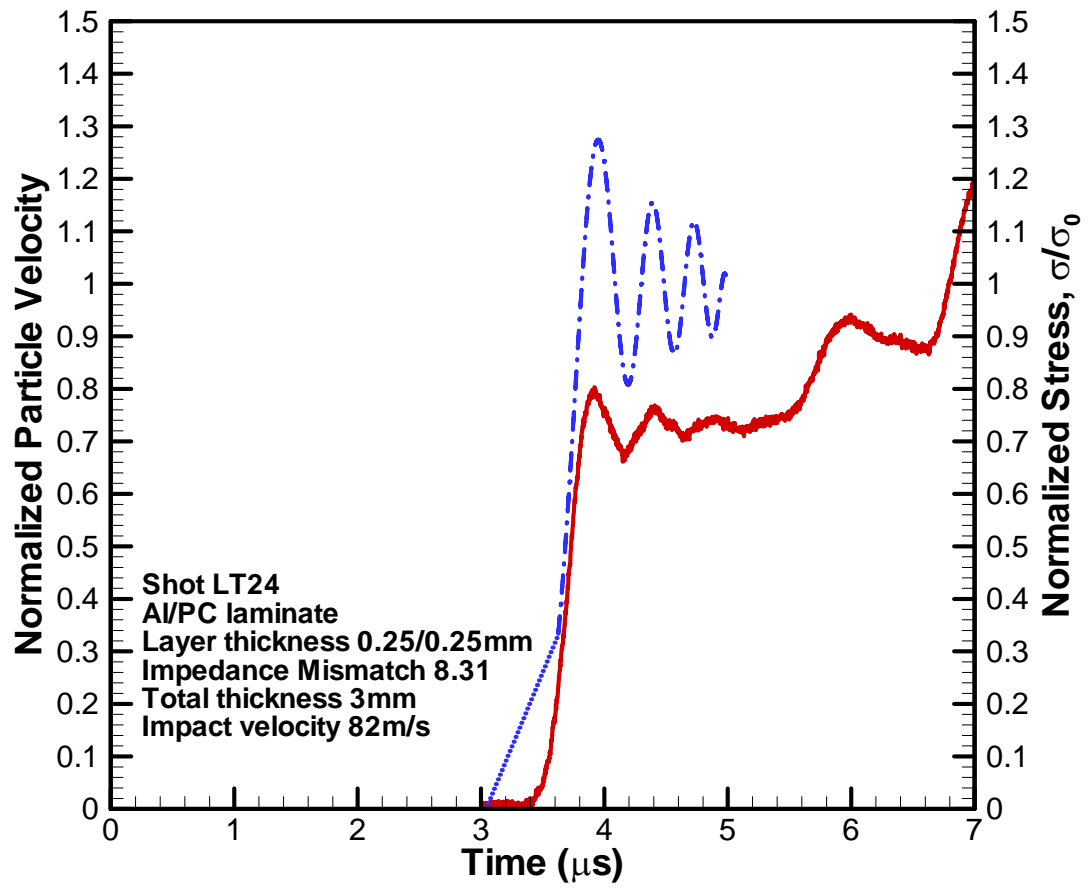


Figure 3.11: Results from plate impact experiments on Al-PC laminates showing the late-time dispersion wave.

The fourth series of experiments was conducted to understand wave propagation in elastic-viscoelastic laminates confined by high impedance elastic plates. The high impedance plates result in reverberation of stress waves within the relatively low impedance sandwiched laminate resulting in an incremental build up of stress with each reverberation of stress wave. In this series of experiments Al-PC bilaminates were utilized. The thickness of each Al and PC layer is 0.125 mm. In the first experiment the laminate comprised 4 alternating layers of Al and PC with a total laminate thickness of 0.5 mm. For the second experiment 8 alternating layers of Al and PC with a total laminate thickness of 1.0 mm were utilized. For the third experiment 12 alternating layers of Al and PC with a total laminate thickness of 1.5 mm were utilized. In each case the Al-PC laminate was sandwiched by high impedance steel plates. A schematic of the experimental configurations for this series of experiments is shown in Figure 3.12. Figure 3.13 shows experimental results on the Al-PC laminates. The impact velocities for the three experiments, LT19, LT18, and LT20 were 81 m/s, 74 m/s and 75 m/s, respectively. The abscissa shows the time after impact while the

ordinate shows the normalized particle velocity. It is seen that in each case, the normalized particle velocity (or the stress) builds up to the impact velocity in a series of steps. Each step represents one reverberation of the stress wave between the CH steel plates. As expected the time duration of each step is longest for the laminate with the greatest thickness, i.e. Shot LT18 with 12 alternating layers of PC and Al. Also, it is interesting to note the oscillatory nature of the particle velocity profile at each loading step. The sudden increase in particle velocity at approximately $8 \mu s$ is consistent with the arrival of the release wave from the lateral boundary. Full simulations of the experiments utilizing finite element methods are required to adequately model the observed velocity versus time profiles for the three sandwiched laminates.

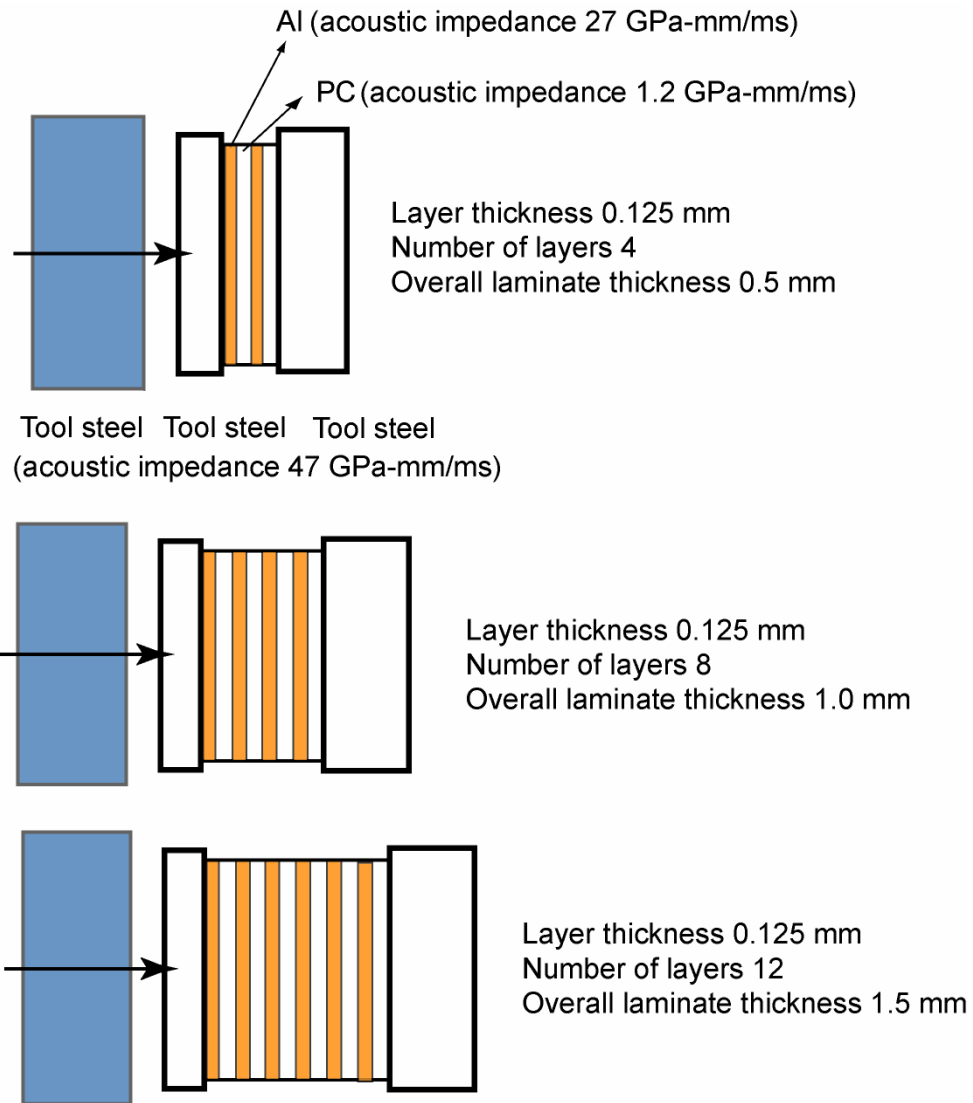


Figure 3.12: Schematic of the laminate architecture employed to conduct the fourth series of plate-impact experiments.

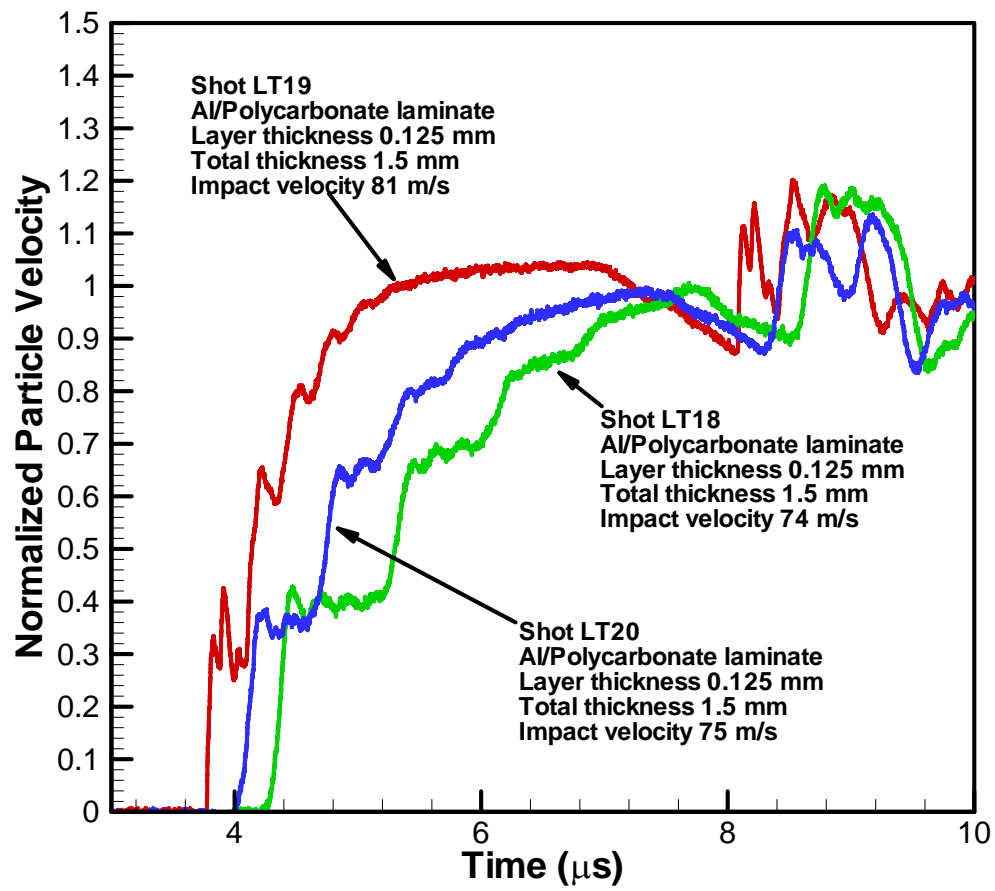


Figure 3.13: Results from plate impact experiments on thin Al-PC laminates sandwiched between two hard CH tool steel plates.

3.4 SUMMARY

In the present study normal plate-impact experiments are conducted on 2-D layered material targets to understand the role of material architecture and material inelasticity in governing the elastic precursor decay and late-time wave dispersion. The particle velocity at the free surface of the target plate is measured by using a multi-beam VALYN VISAR. In order to understand the effects of layer thickness and the distance of wave propagation on elastic precursor decay and late-time dispersion several different targets with various layer and target thicknesses are employed. Moreover, in order to understand the effects of material inelasticity both elastic-elastic and elastic-viscoelastic bilaminates are utilized.

The results of these experiments are interpreted by using asymptotic techniques to analyze propagation of acceleration waves in 2-D layered material systems as discussed in chapter 2. The results of the study indicate that the structure of acceleration waves is strongly influenced by impedance mismatch of the layers

constituting the laminates, density of interfaces, distance of wave propagation, and the material inelasticity. The speed of the elastic precursor is independent of the impedance mismatch of the individual laminae constituting the bilaminates and is equal to the average wave speed within the bilaminates. The speed of late-time dispersion wave is observed to decrease with an increase in impedance mismatch; however, it is found to be independent of the density of interfaces, i.e. the number of layers in a given thickness laminate. The decay in elastic precursor is observed to increase with an increase in impedance mismatch, the density of interfaces, and the distance of wave propagation. The rise-time of the late-time dispersion wave increases with an increase in impedance mismatch; however, it is observed to decrease with an increase in the density of interfaces. The frequency of oscillations of the late-time dispersive wave is observed to decrease with an increase in impedance mismatch; however, it is observed to increase with an increase in the density of interfaces.

REFERENCES

- Achenbach J. D., 1973. Wave Propagation in Elastic Solids. North-Holland, Amsterdam.
- Barker L. M., Lundergan C. D., Chen P. J. and Gurtin M. E., 1974. Nonlinear viscoelasticity and the evolution of stress waves in laminated composites: a comparison of theory and experiment. *Journal of Applied Mechanics* 41, 1025-.
- Benson D. J. and Nesterenko V. F., 2001. Anomalous Decay of shock impulses in laminated composites. *Journal of Applied Physics* 89(7), 3622-3626.
- Betheney W., DeLuca E., Prifti J. and Chou S. C., 1998. Ballistic impact damage of S2-glass reinforced plastic structural armor. *Composites Science and Technology* 58, 1453-1461.
- Cerrillo M V, 1950. Technical Report No.55, 2a, Research Laboratory of Electronics MIT, Cambridge, MA.
- Chen C. C. and Clifton R. J., 1974. Asymptotic Solutions for Wave Propagation in Elastic and Viscoelastic Bilaminates. In: *Developments in Mechanics, Proceedings of the 14th Mid-Eastern Mechanics Conference*: 26, 8., pp. 399-417.
- Clifton R. J., 1972. Solution of wave problems in inelastic materials. In: *Summer Course on Dynamics of Inelastic Materials* Jablonna, Poland.
- Fink B., 2000. Performance metrics for composite integral armor. *Journal of Thermoplastic Composite Materials* 13(5), 417-431.
- Hegemier G. A., 1972. On a theory of interacting continua for wave propagation in composites. In: *Dynamics of Composite Materials*. ed(s): E. H. Lee. ASME, pp. 70-121.
- Hemsing W. F., 1979. Velocity sensing interferometer (VISAR) modification. *Review of Scientific Instrumentation* 50(1), 73-78.

Hill W H and Shimmin K D, 1961. Elevated Temperature Dynamic Elastic Moduli of Various Metallic Materials. WADD Twchnical report 60-438. Wright-Patterson Air force base, Ohio.

Laptev V. I. and Trishin Y. A., 1976. The increase of velocity and pressure under impact on inhomogeneous target. Journal of Applied Mechanics and Technical Physics, 837-841.

Lundergan C D and Drumheller D S, 1971. Dispersion of shock waves in composite materials. Shock Waves and the Mechanical Properties of Solids. Syracuse University Press, New York, p 141-.

Nesterenko V F, Fomin V M and Cheskidov P A, 1983. Attenuation of strong shock waves in laminate materials. Nonlinear Deformation Waves. Springer Verlag, Berlin, pp 191-7.

Nesterenko V. F., Fomin V. M. and Cheskidov P. A., 1984. Damping of strong waves in laminar materials. Journal of Applied Mechanics and Technical Physics, 567-575.

Oved Y., Luttwak G. E. and Rosenberg Z., 1978. Shock wave propagation in layered composites. Journal of Composite Materials 12, 84-.

Peck J. C. and Gurtman G. A., 1969. Dispersive pulse propagation parallel to the interfaces of a laminated composite. Journal of Applied Mechanics, 479-484.

Sherby O. D., Lee S., Koch R., Sumi T. and Wolfenstine J., 1990. Multilayered composites based on ultrahigh carbon steel and brass. Materials and Manufacturing Processes 5, 363-376.

Stern M., Bedford A. and Yew C. H., 1970. Wave propagation in viscoelastic laminates. Journal of Applied Mechanics 70-WA/APM-40, 1-7.

Sun C.-T., Achenbach J. D. and Herrmann G., 1968. Time-harmonic waves in a stratified medium propagating in the direction of the layering. Journal of Applied Mechanics, 408-411.

Sve C., 1971. Thermo-elastic Waves in a Periodically Laminated Medium. International Journal of Solids Structures, 7, 1363-1373.

Sve C., 1972. Stress wave attenuation in composite materials. Journal of Applied Mechanics, 1151-1153.

Vaidya U. K., Hosur M. V., Kumar P., Mahfuz H., Haque A. and Jeelani S., 1999. Impact damage resistance of innovative functional sandwich composites. In: ASME 1999 Mechanics and Materials Conference Blacksburg, VA.

Zhuang S, 2002. Shock Wave Propagation in Periodically layered composites. PhD Dissertation, California Institute of Technology, Pasadena, CA.

Chapter 4

DYNAMIC RESPONSE OF S2 GLASS FIBER REINFORCED POLYMER COMPOSITE

4.1 Introduction

The understanding of behavior of materials under dynamic loading conditions is vital to many areas of both civil and military applications. Better understanding of dynamic response has important practical implications connected with impact and blast mitigation, design of lightweight armor, as well as optimal design of other engineered structures with potential danger of shock loading. Currently, a variety of material systems ranging from metal, ceramics, and polymers, in both monolithic and composite forms, are being used to achieve a combination of characteristics to meet the desired goals. Some of the recent examples highlighting the success of these systems include woven composites and functionally graded materials (Neubrand *et al.*, 1997).

The fiber reinforced composite materials are widely considered as the new revolution in materials (Sierakowski and Chaturvedi, 1997). These material systems can be engineered to have the same strength and stiffness as high-strength steels, yet they are 70% lighter. There are basically three major advantages in the use of fiber-reinforced composite materials: relatively high specific strength and stiffness, cost, and near net processability (Jones, 1999). Because of these key factors, glass-fiber reinforced composite materials have been designated to be a large part of a composite integral armor system, as was discussed in Chapter 1.

A large body of knowledge currently exists in the literature on the propagation of acceleration waves and finite amplitude shock waves in heterogeneous materials. For such systems, scattering, dispersion and attenuation play a critical role in determining the thermo-mechanical response of the media. In particular, the non-linear behavior of the S2-glass fiber reinforced polymer composites (GRP) can be attributed to the complex material architecture, i.e. the impedance and geometric

mismatch at the various length scales, and damage evolution in the form of void nucleation and growth, glass fiber fracture, and delamination,. A two-wave shock response was reported in Chapters 2 & 3 due to its layered structure. The elastic precursor was found to decrease with increasing material impedance mismatch, inelasticity, and shock wave propagation distance, whereas the amplitude of the late-time oscillations was found to decrease with increasing material inelasticity.

In this chapter, results of plate-impact experiments conducted with various different thicknesses of GRP plates impacted by Al 7075-T6 and D7 tool-steel flyer plates over a range of impact velocities are discussed. The shock compression experiment data by Dandekar *et al.* (1998, 2003) on the same batch of GRP are also discussed for a more complete analysis at higher impact stress levels. From this data, the attenuation of shock front, the dispersion of shock waves, Hugoniot Elastic Limit (HEL), and the Equation of State (EOS) for the GRP are determined. The shock responses of GRP were also compared with the findings in Chapter 2 & 3.

4.2 Experiment Configuration

The experiments were conducted using the 82.5mm single-stage gas-gun at Case Western Reserve University, as described in detail Chapter 3. The experiments involve the impact of a flyer plate with the GRP target at normal incidence. The waves transmitted through the GRP are monitored at the free surface of the target by means of a laser interferometer (Multi-beam VISAR system). The measured motion at the free surface is then used to obtain the wave characteristics as the shock wave propagates through the GRP specimen.

The schematic of the plate-impact experimental configuration is shown in Figure 4.1. A fiberglass projectile carrying the flyer-plate is accelerated down the gun barrel by means of compressed Helium gas. Rear-end of the projectile has sealing O-ring and a plastic (Teflon) key that slides in a key-way inside the gun barrel to prevent any rotation of the projectile. In order to reduce the possibility of an air cushion between the flyer and target plates, impact is made to occur in a target chamber that has been evacuated to 50 μ m of Hg prior to impact. A laser-based optical system, utilizing a UNIPHASE Helium-Neon 5mW laser (Model 1125p)

and a high frequency photo-diode, is used to measure the velocity of the projectile. To ensure the generation of plane-waves, with wave-front sufficiently parallel to the impact face, the flyer and the target plates are aligned carefully to be parallel to within 2×10^{-5} radians by using an optical alignment scheme. The actual tilt between the two plates is measured by recording the times at which four, isolated, voltage-biased pins, that are flush with the surface of the target plate, are shorted to ground. The acceptance level of the experiments is of the order of 0.5 mrad. A VALYN VISAR laser interferometer is used to measure the history of the normal particle velocity at the rear surface of the target plate. A COHERENT VERDI 5W solid-state diode-pumped frequency doubled Nd:YVO₄ CW laser with wavelength of 532 nm is used to provide a coherent monochromatic light source.

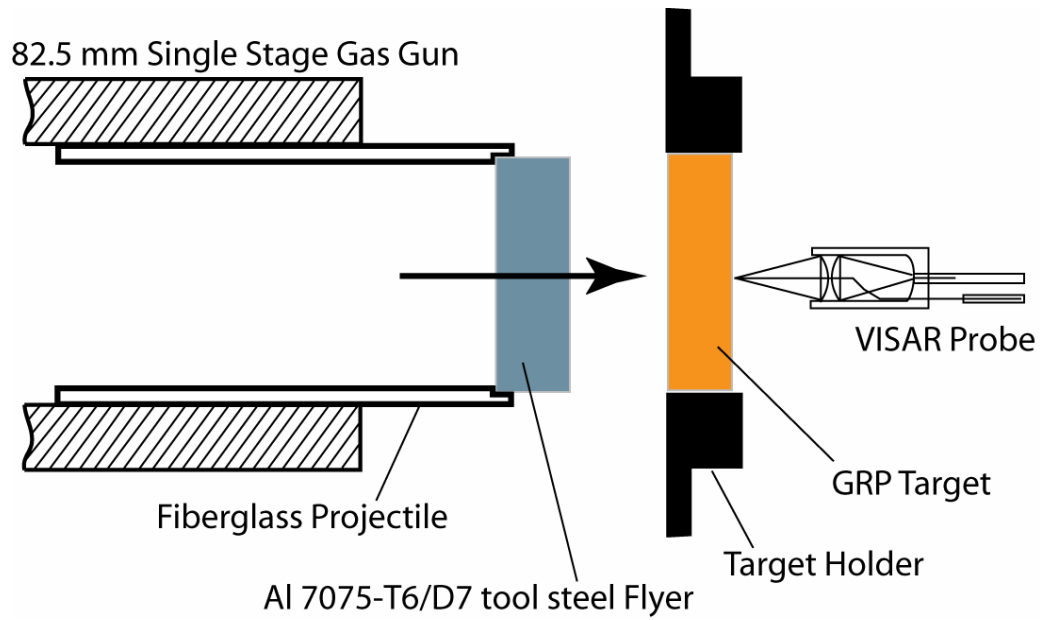


Figure 4.1: Schematic of the plate impact configuration employed in the present investigation.

4.2.1 Target Assembly

A typical target holder assembly with the GRP specimen is shown in Figure 4.2.

The target holder was made of aluminum to also double up as ground for the trigger and the tilt measurement systems. One ground pin and four trigger pins were mounted near the periphery of the GRP specimen, all the way through the thickness of the target holder. The GRP specimen, ground pin, and the trigger pins were all glued in place by epoxy and lapped to be flush with the impact surface, which is shown with the face down in the figure. For all the GRP

experiments, a thin (60~125 nm) aluminum coating was applied to the rear free-surface of the GRP specimen to enhance the reflection for VISAR measurement.

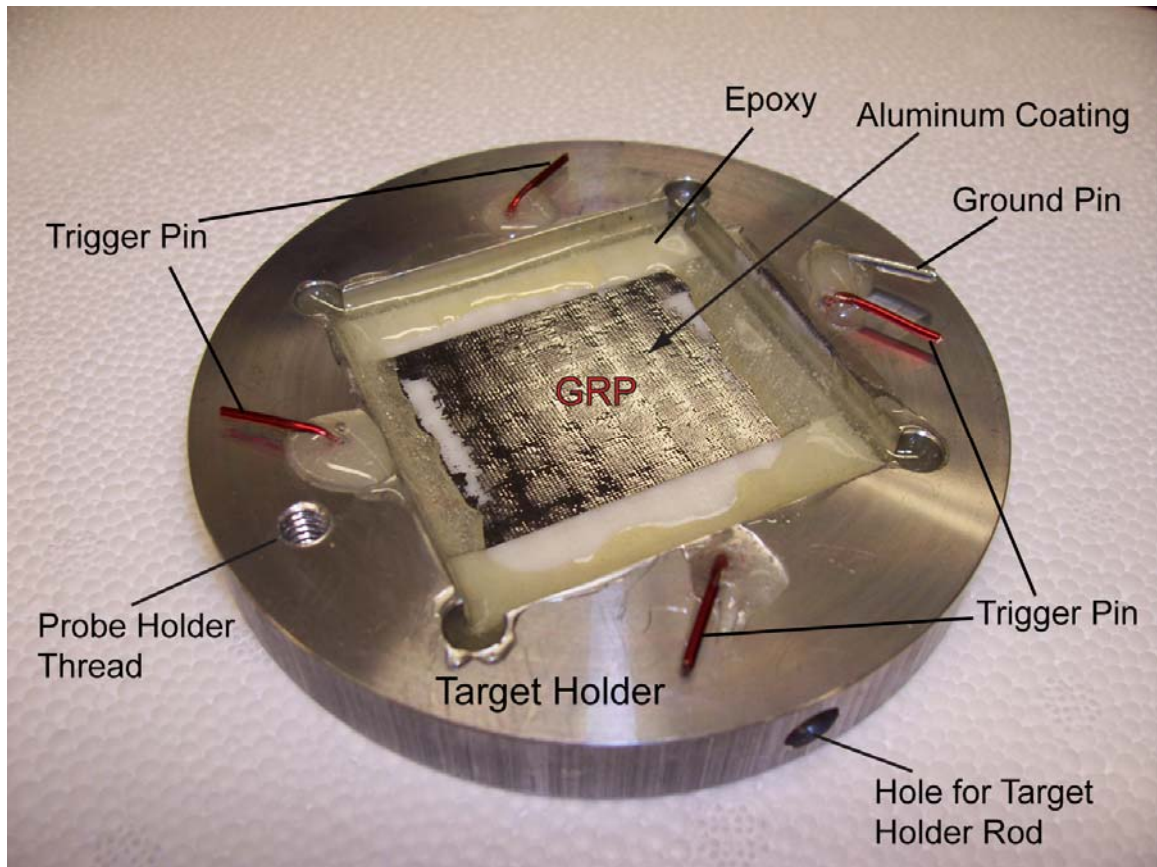


Figure 4.2: Photograph of one of the target assembling for GRP specimens.

4.2.2 t-X diagram (Time vs. Distance) & S-V diagram (Stress vs. Velocity)

The t-X diagram for normal impact gas gun experiments on GRP is shown in Figure 4.3. The abscissa represents the distance from impact surface; the positive axis denotes the distance into the target (GRP) and negative axis denotes the

distance into the flyer (Al 7075-T6 or D7 tool steel). The ordinate represents the time after impact. The solid lines indicate the propagation of the compressive waves while dashed-lines indicate the propagation of the tensile waves. Figure 4.4 shows the stress and particle velocity diagram, referred to as the S-V diagram from here onwards, for the same experiment. The S-V diagram provides the locus of all the stress and particle velocity states that can be attained during a typical experiment. The abscissa represents the particle velocity in the target and the flyer plates, while the ordinate represents the stress in the target and flyer. The positive direction on the ordinate corresponds to compressive stresses while the negative represents the tensile stress. In order to eliminate the possibility of spall (delamination) during the experiment, tensile stress condition inside target must be avoided. In order to avoid the tensile stress inside the GRP target, the tensile wave reflected from flyer free surface, and the release wave reflected from the free surface of the target plate should not meet within the GRP target plate during the time duration of the experiment. In order to achieve this the thickness of the flyer-plate is chosen such that the time at which the release wave from the free

(back) surface of the flyer plate arrives at the impact surface is later than the time of the arrival of the release wave from the free (back) surface of the target plate, i.e. $t_3 > t_2$.

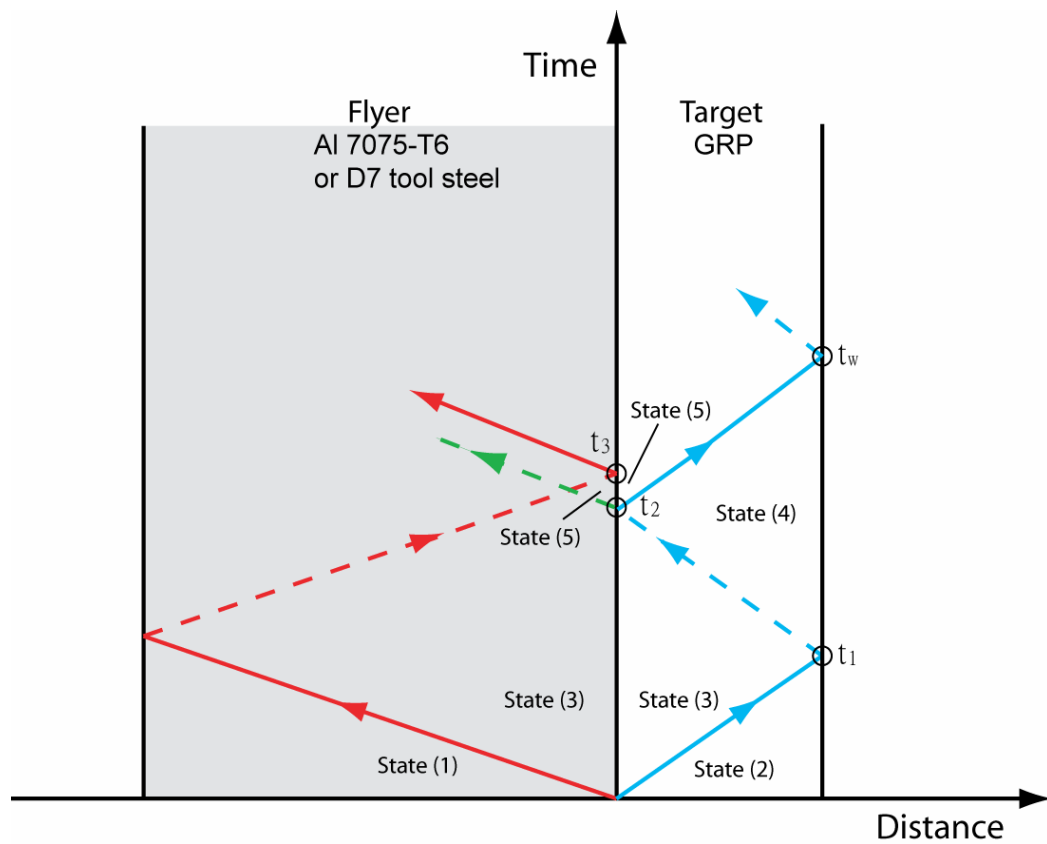


Figure 4.3: t-X diagram for normal impact gas gun experiments on GRP.

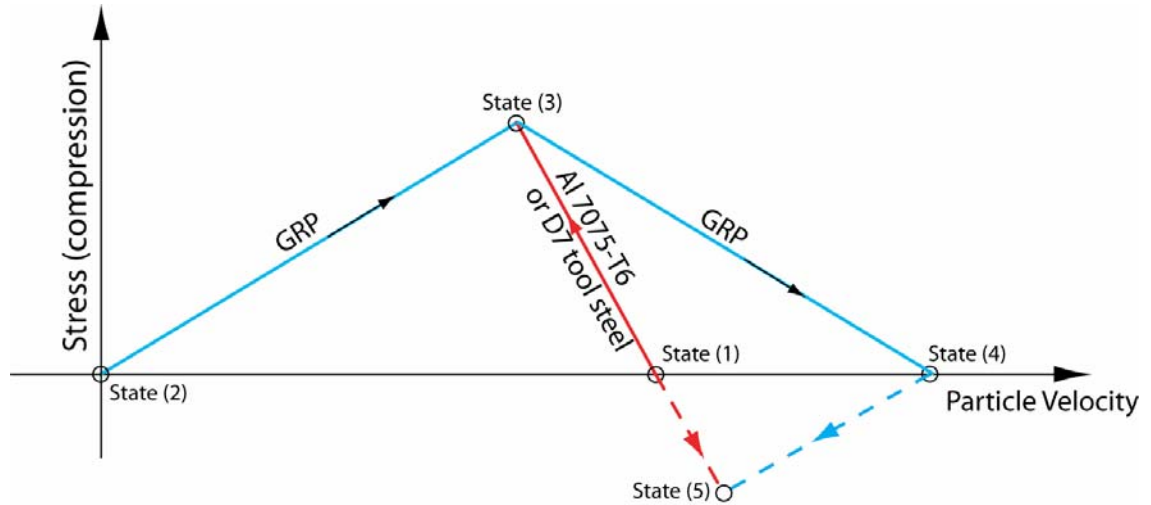


Figure 4.4: S-V diagram for normal impact gas gun experiments on GRP.

4.3 Experimental Results and Discussion

In the present study a series of plate impact experiments were conducted to develop a comprehensive understanding of the structure of compressive shock waves in the GRP. Four different thicknesses of GRP specimens with dimensions of 54mm X 54mm, and thicknesses of 3mm, 7mm, 13.5mm, and 20mm, were utilized for characterization. In the experiments the amplitude of the shock waves was made to vary from 0.03 to 2.6GPa. The GRP specimens were machined from large 510mm X 510mm GRP plates to their 54 mm X 54 mm square size. Table 4.1 details the flyer material, impact velocity, GRP target thickness, free surface particle velocity, and shock wave arrival time for each

experiment. The measured free-surface particle-velocity versus time profile for each experiment is listed in Appendix A.

The first section of this chapter is focused on the structure of the shock waves in GRP targets as a function of increasing impact velocity, as obtained from measurements of the free surface particle velocity at a fixed target thickness. The second section discusses the dispersion and attenuation characteristics of finite amplitude shock waves in GRP as a function of target thickness and subjected to a fixed amplitude shock wave loading. From these experimental results, the shock velocities and free surface particle velocities were obtained and used to estimate the Equation of State (Shock Velocity vs. Particle Velocity) in the third section. The fourth section focuses on the loci of the Hugoniot Stress versus Hugoniot strain obtained in the GRP specimens under shock compression including the data from Dandekar *et al.* (2003). The fifth section provides an estimate for the Hugoniot Elastic Limit (HEL) of GRP based on the data acquired in this research and those from Dandekar *et al.* (2003).

Exp No.	Flyer Material	Impact Velocity (m/s)	Target Thickness (mm)	Free Surface Particle Velocity (m/s)	Shock Wave Arrival Time (μ s)
LT25	AL7075-T6	184.29	6.88	276.54	2.347
LT27	AL7075-T6	187.65	20.2	277.46	6.317
LT28	AL7075-T6	183.98	2.94	286.18	1.078
LT29	AL7075-T6	191.49	12.37	284.97	3.597
LT30	AL7075-T6	111.69	6.75	171.12	2.155
LT31	AL7075-T6	312.70	6.55	456.26	1.952
LT32	AL7075-T6	113.71	19.35	165.80	5.970
LT33	AL7075-T6	312.72	19.25	437.98	5.669
LT35	AL7075-T6	52.5	13.35	76.99	4.454
LT36	AL7075-T6	43.9	12.95	65.85	4.136
LT37	AL7075-T6	39.13	13.07	56.58	4.155
LT38	AL7075-T6	8.5	13.23	12.47	4.817
LT40	AL7075-T6	108.1	13.10	155.31	3.774

Exp No.	Flyer Material	Impact Velocity (m/s)	Target Thickness (mm)	Free Surface Particle Velocity (m/s)	Shock Wave Arrival Time (μ s)
LT41	AL7075-T6	212.38	13.59	307.92	4.247
LT42	AL7075-T6	104.7	13.46	150.82	4.228
LT43	AL7075-T6	42.36	13.51	59.97	4.707
LT44	AL7075-T6	68.96	13.26	99.91	4.063
LT45	AL7075-T6	47.36	13.61	71.38	4.449
LT46	D7 tool steel	329.13	6.95	575.34	2.060
LT47	D7 tool steel	367.88	6.8	661.98	1.897
LT48	D7 tool steel	417.96	6.76	807.16	1.978
LT49	D7 tool steel	416.96	6.85	780.61	1.958
LT50	AL7075-T6	188.17	0	265.51	3.983
LT51	AL7075-T6	172.76	0	257.83	3.942
LT52	AL7075-T6	138.86	0	195.98	4.101
LT53	AL7075-T6	133.23	0	207.47	4.306
LT54	AL7075-T6	140.64	0	219.51	3.938

Exp No.	Flyer Material	Impact Velocity (m/s)	Target Thickness (mm)	Free Surface Particle Velocity (m/s)	Shock Wave Arrival Time (μ s)
LT55	AL7075- T6	82.86	15.0	114.13	4.453
LT56	AL7075- T6	75.75	12.0	105.89	4.449
LT57	AL7075- T6	59.98	12.0	85.65	4.162
LT58	AL7075- T6	43.48	15.0	61.52	4.244
LT59	AL7075- T6	31.95	20.0	45.10	4.797
LT60	AL7075- T6	48.41	12.0	70.26	4.981
LT61	AL7075- T6	68.17	12.0	95.97	4.510

Table 4.1: GRP plate impact experiments data table.

4.3.1 Structure of Shock Waves in Compression in GRP

In the present work a series of plate impact experiments were conducted on GRP at stress levels between 0.03 to 2.6 GPa. The measured free surface particle velocity profiles from experiments with nearly the same GRP thickness were used to establish the relationship between the shock stress and the structure of shock waves in the GRP. Figure 4.5 shows the free surface velocity profiles at five different levels of shock stress for a 7 mm thick GRP specimen. The abscissa represents the time after the arrival of the shock waves at the free surface of the target plate and the ordinate represents the free-surface particle-velocity. Experiments LT30, LT25, and LT31 were shock loaded to 519 MPa, 824 MPa, and 1461 MPa, respectively, using 7075-T6 aluminum flyer plates. Experiments LT47 and LT48 were shock loaded to 2022 MPa and 2611 MPa, respectively, using D7 tool-steel flyer plates. It should be noted that in experiments with impact stresses less than 1.5 GPa the shock front is not observed. On the other hand, in experiments with impact stresses greater than 2.0 GPa, the presence of shock front is clearly evident. Moreover, it is to be noted that the slope of initial wave front increases with the increasing impact stress. Barker *et al.* (1974)

proposed the idea of a “critical amplitude”, which represents the specific shock stress for a clear shock-front to appear during shock loading for a variety of materials of interest. In this regards, the critical stress amplitude for GRP is estimated to be between 1.5 and 2.0 GPa.

In Chapter 2, the late-time shock wave profiles for the elastic-elastic bilaminates were determined to be oscillatory, with the frequency of oscillations related to the density of interfaces. However, this oscillatory behavior is not observed for the S2 glass fiber reinforced composites, as shown in Figure 4.5. Some oscillations were seen in the shock profile for Shot LT30, but for all other experiments the late-time shock wave profiles were relatively flat. This absence of the oscillatory behavior is understood to be due to the development of a complex wave interference patterns within the composites because of the impedance mismatch between the S2-glass fiber woven layers and the thin polymer layers, and also the inelasticity of the polymer interlayer that tends to increase the wave dispersion and hence the rise time of the wave profiles. Also, in agreement with the analysis

presented for the elastic-viscoelastic bilaminates in Chapter 2, the elastic precursor was not observed-- this is primarily understood to be because of the inelasticity of the epoxy layer and the complex polymer/S2-glass interfaces. In Figure 4.5, the black circular markers indicate the position at which the slope of the particle velocity profiles changes during the rise-time. It should be noted that these markers do not indicate the Hugoniot Elastic Limit of the composites and the origin of the change of slope at the black markers is likely due to the viscoelastic response of the polymer layers. Moreover, because of the layered architecture of the composite and the inelasticity of polymer matrix, the shock waves do not develop a sharp fronted wave. Rather, the wave profiles gradually approach the equilibrium level -- like in experiments LT30, LT31, and LT48 -- or overshoot the equilibrium level then settle down to the equilibrium level -- like in experiments LT25 and LT47. Whether the wave fronts approach the equilibrium level gradually or over-shoot the equilibrium level depends on the relative importance of two competing attenuation mechanisms. When the inelasticity in polymer layers is the dominant factor the shock front approaches the equilibrium

level gradually; otherwise, when the layered structure is the dominant factor the shock front over shoots the equilibrium level (Sve, 1972).

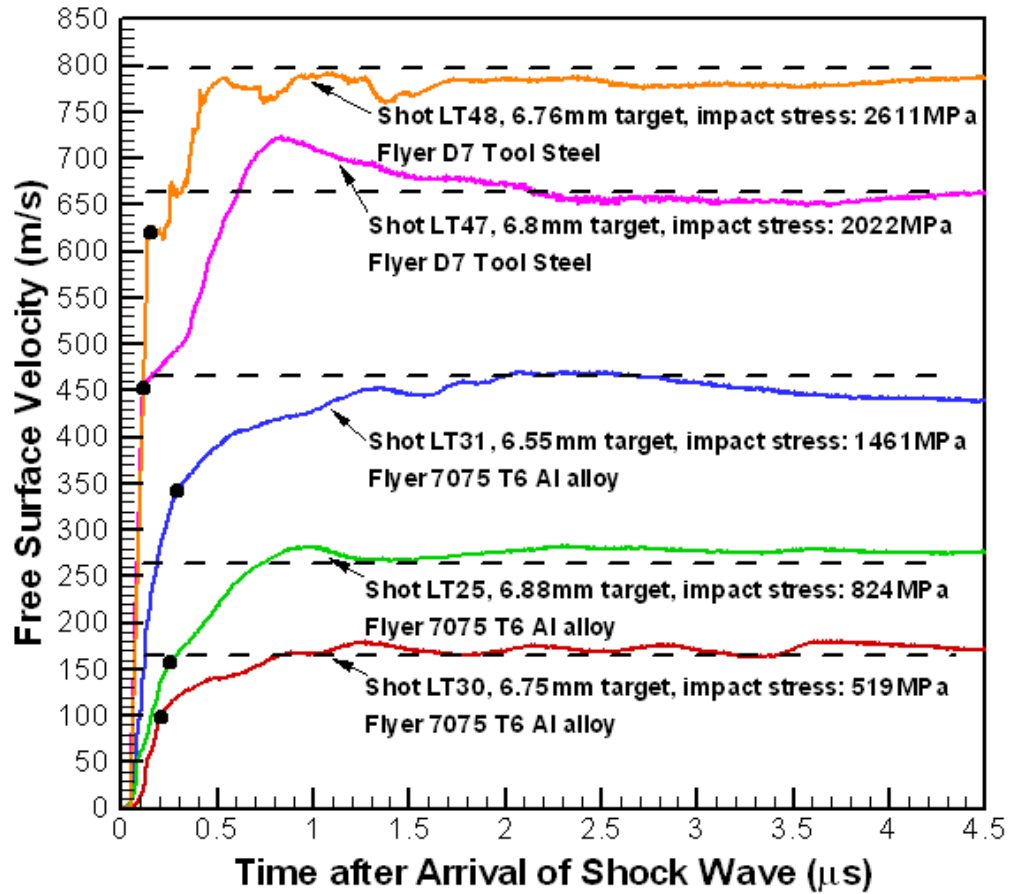


Figure 4.5: Free surface velocity profiles during five different shock-loading on 7 mm GRP specimens and the dashed lines represent the elastic estimate level.

Error! Reference source not found. shows all the free-surface particle-velocity profiles from experiments conducted at the various impact velocities on the 13mm thick GRP specimens. The dashed lines indicate the elastic prediction for the experiments assuming the flyer plate and the GRP composite to remain elastic. The change in slope of wave front with increasing shock compression is quite evident. Moreover, the oscillatory nature of the shock wave profile can be clearly observed in the experiments. Besides the experiment with lowest compression stress, i.e. Shot LT38, the experiments shown in Figure 4.6 can be categorized into three main groups based on the level of the shock stress imparted to the composite: experiments with shock stresses below 350MPa, shock stress between 350 and 700MPa, and shock stresses above 700MPa and less than 1GPa. The particle-velocity versus time profiles for these experiments are shown in Figure 4.7, Figure 4.8, and Figure 4.9, respectively. None of the experiments show a clear shock front; however, the change in slope of the wave front with increasing impact stress is quite evident from the figures. Besides the increase in slope at the wave-front, the difference in the number of oscillations in the late-

time particle velocity versus time profiles in the three impact velocity regimes is quite evident. From Figure 4.7, it can be seen that the oscillations in the wave profiles have an amplitude between 7~10% of the equilibrium level. From Figure 4.8, it can be seen that the oscillations in the wave profiles were about 5~8% of the equilibrium level, while from Figure 4.9 the oscillations in the wave profiles are seen to be about 3% of the equilibrium level.

Thus, in summary, the results of the present experiment indicate that with increasing levels of shock stress the slope of shock wave front increases continuously. Also, the amplitude of the oscillations in the wave profiles decrease with increasing levels of shock stress. In this regards, it could be argued that at lower impact stresses the layered structure dominates the late-time wave profiles, but at higher impact stresses the inelasticity of constituent materials dominate the GRP's shock response.

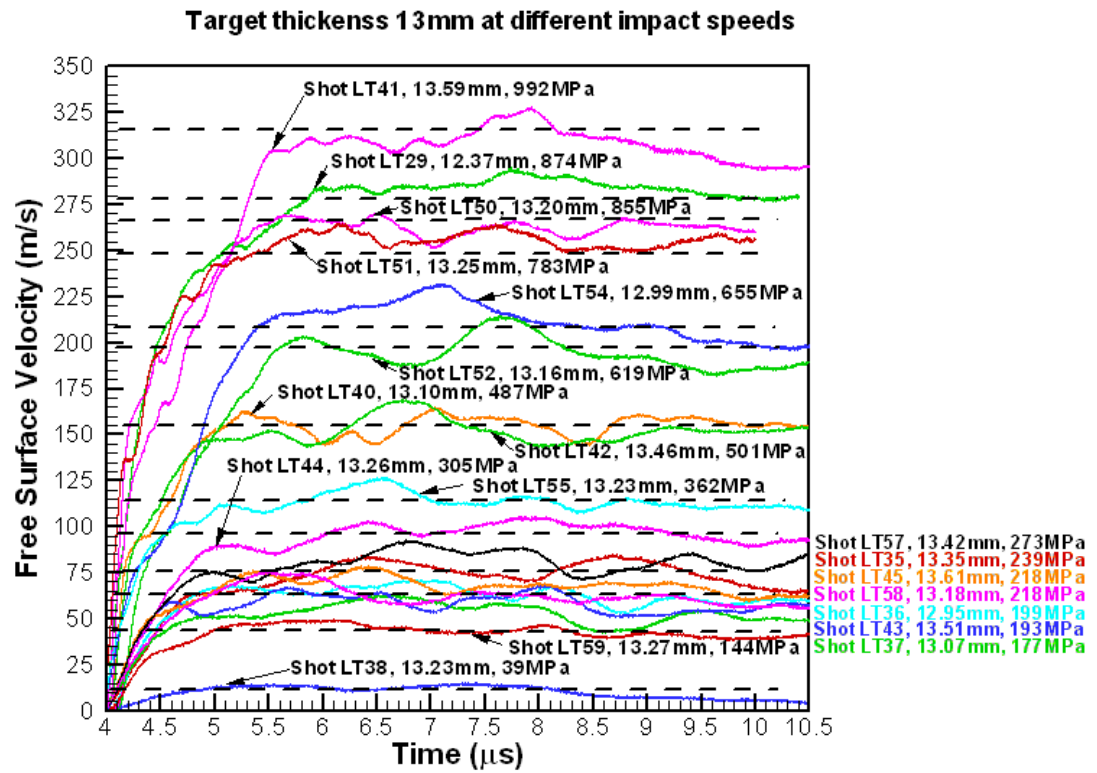


Figure 4.6: Free surface profiles for 13.5 mm GRP plates under different shock compressions.

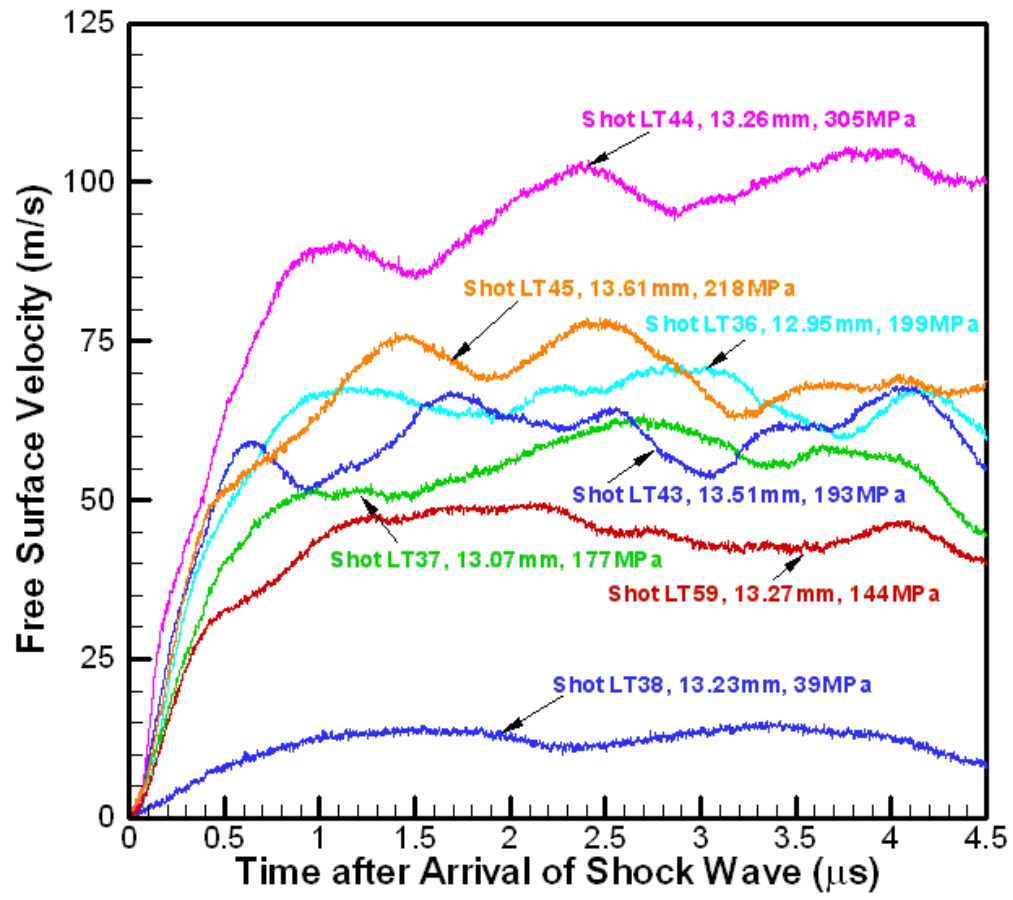


Figure 4.7: Free surface velocity wave profiles for 13 mm GRP specimens at lower stress range.

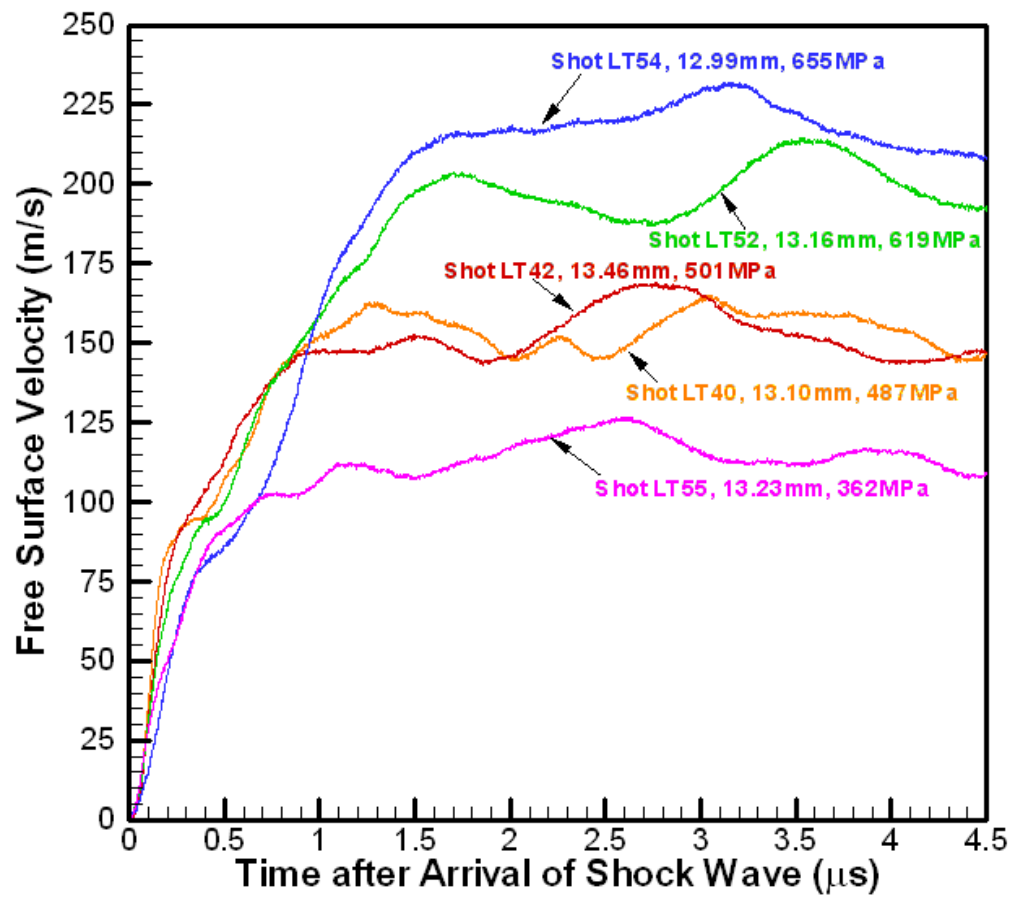


Figure 4.8: Free surface velocity wave profiles for 13 mm GRP specimens at medium stress range.

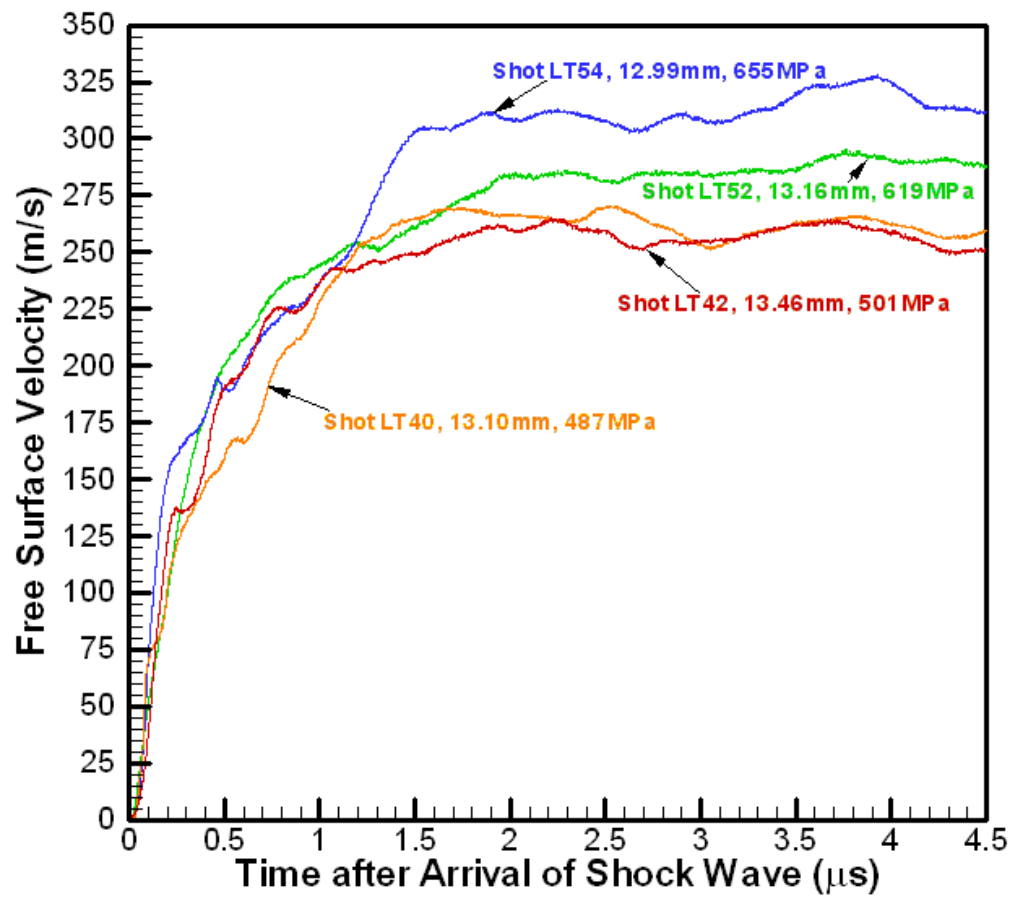


Figure 4.9: Free surface velocity wave profiles for 13 mm GRP specimens at higher stress range.

4.3.2 Structure of Shock Waves in Compression in GRP as a Function of Shock Wave Propagation Distance

The effect of the amplitude of shock wave loading on the dynamic response of GRP was the focus of attention in the experiments described in Section 4.3.1. In this section, we will focus on characterizing the shock response of GRP with various different thicknesses under shock wave loading conditions. Figure 4.10 shows the free-surface particle-velocity versus time profiles obtained from experiments on four different thicknesses of GRP specimens, i.e. experiments LT28, LT25, LT29, and LT27 with GRP target thickness of 2.94mm, 6.88mm, 12.37mm, and 20.2mm, respectively. In these experiments the amplitude of the impact stresses were 865 MPa, 824 MPa, 874 MPa, and 842 MPa, respectively. From the experiments it is clearly evident that during the rise-time a distinct knee in the velocity time profile is observed in each of the four experiments. This knee is denoted by a black filled symbol on each particle velocity profile and the slope of the velocity time profiles after this knee decreases with the thickness of the GRP target, i.e. with distance of wave propagation. It is interesting to note that the stress level at which the slope change occurs (i.e. the stress levels of

black markers) decreases with increasing GRP thickness. This phenomenon is similar to the elastic-precursor decay observed in elastic-viscoplastic materials, and is understood to be a result of both material and geometric dispersion in the case of the S2-glass reinforced polymer composites. The effect becomes more prominent as the thickness of the GRP target increases. It is interesting to note that the equilibrium stress level for the four experiments are fairly close to each other, and the equilibrium level is observed to decrease a little for the thickest GRP specimen, i.e. Experiment LT27. However, the time corresponding to the decrease in particle velocity observed is very close to the arrival of the release waves from the boundary of the specimen.

These measured stress wave profiles are quite different from those observed in the study by Boteler *et al.* (1999) at ARL, Aberdeen, MD, on the same batch of GRP. In their experiments, Boteler *et al.* (1999) employed embedded PVDF piezoelectric gages to investigate the attenuation and dispersion characteristics of shock wave propagation in the GRP specimens. Figure 4.11 shows the experiment

configuration for their experiment Shot -- 9919. The PVDF gauges were mounted between four GRP plates; the thicknesses of the Al 6061-T6 flyer plate A, and GRP target plates B, C, D, and E were 6.471 mm, 3.061 mm, 3.288 mm, 6.928 mm, and 20.398 mm, respectively. Figure 4.12 shows the experimental data from the Shot -- 9919. Shock wave attenuation with increasing distance of wave propagation can be clearly observed, which is very different from the results shown in Figure 4.10. A possible reason for this behavior can be attributed to the relatively thin flyer plate (6.471mm) used in the experiment by Boteler et al. (Shot-9919), as opposed to the 25.4mm thick flyer plate utilized in experiments LT28, LT25, LT29, and LT27 in Figure 4.10. The relatively thin flyer plate allowed release wave from the back of the flyer plate to overtake the propagating shock front, resulting in a “hydrodynamic decay” of the shock-wave amplitude with the distance of wave propagation.

Using the assumption of simple hydrodynamic response of materials, the average rate of release wave can be represented as

$$\dot{P} = \frac{dP}{dt} = P_m \left[d_0 \left(\frac{\rho_0}{\rho(u_p + C)} - \frac{1}{C_0} \right) \right]^{-1}. \quad (4.1)$$

In Equation (4.1), P_m indicates the shock pressure, d_0 is the thickness of the flyer plate, u_p is the particle velocity, C is the sound velocity at a particular pressure, C_0 is sound velocity at wave front, ρ_0 is the density of flyer, and ρ is the flyer density at a particular pressure. This equation explained that as the thickness of flyer becomes smaller the rate of release wave is increased leading to a faster decay of the peak pressure of the shock wave as they propagate through the target, as illustrated in Figure 4.13 (Meyers, 1994). For the experiments shown in Figure 4.10, the flyer plates were designed to be thick such that the release waves did not arrive in the target plate during the time duration of the interest in the experiment, and so did not lead to any hydrodynamic attenuation of the shock wave with distance of stress wave propagation.

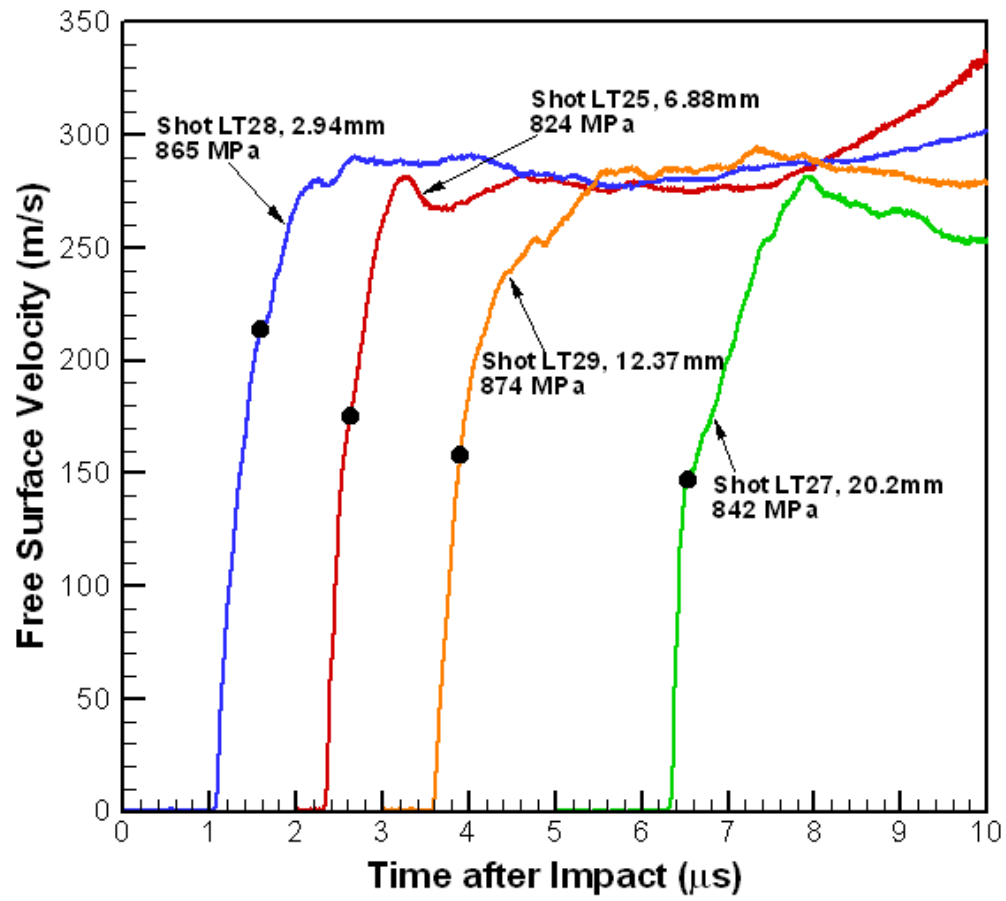


Figure 4.10: Free surface velocity profile for four different thicknesses GRP composites under same shock loading condition.

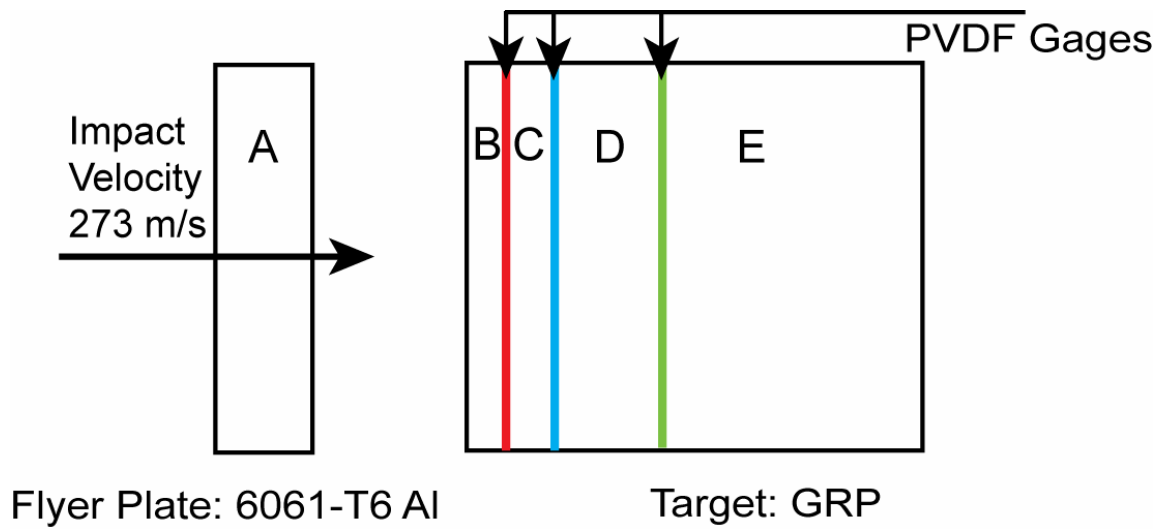


Figure 4.11: Experiment setup of Shot-9919 from Boteler et al. The PVDF gauge was mounted between four GRP plates and the thicknesses of flyer plate A, GRP plates B, C, D, and E are 6.471 mm, 3.061 mm, 3.288 mm, 6.928 mm, and 20.398 mm, respectively.

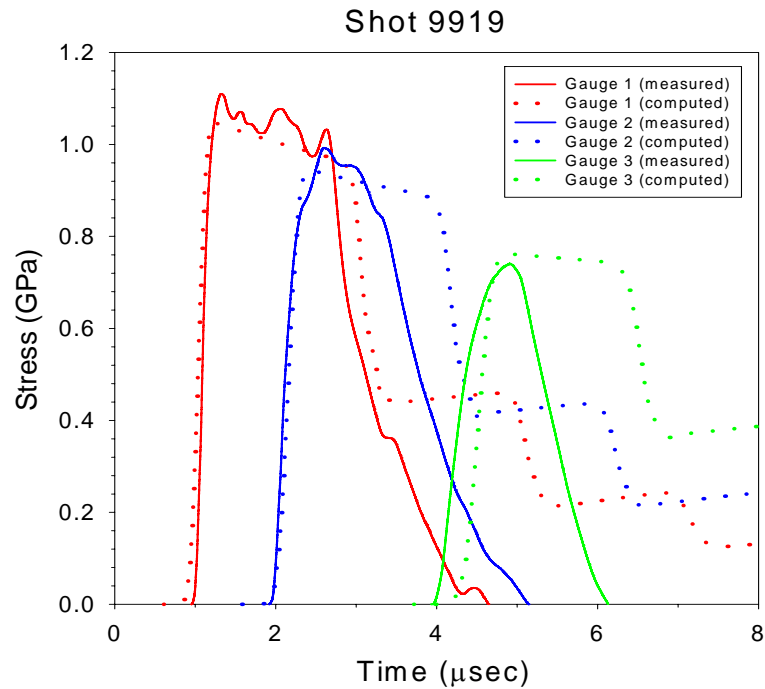


Figure 4.12: Shock response of GRP at different thickness using PVDF gauges by Boteler et al. in 1999.

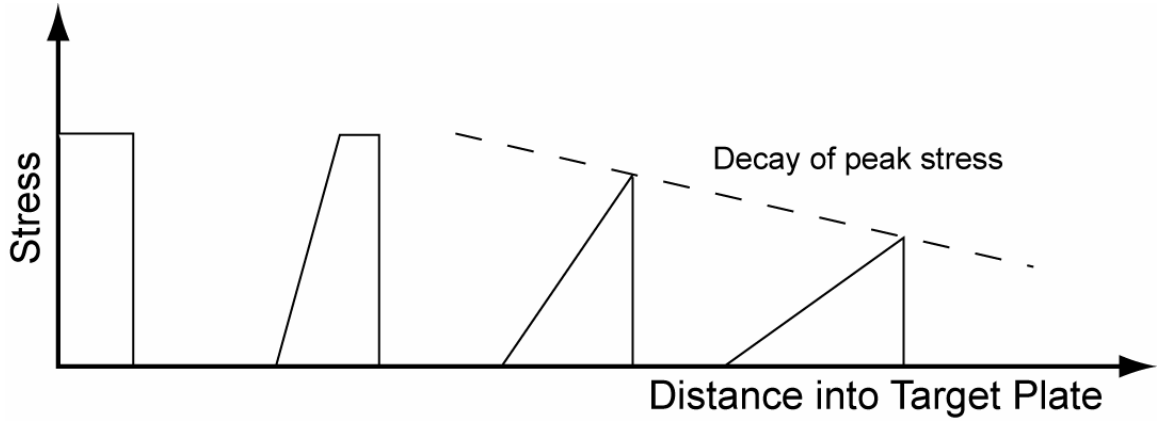


Figure 4.13: Propagation of shock wave through material, release wave front steadily overtakes shock front.

4.3.3 Equation of State (Shock Velocity vs. Particle Velocity)

The Rankine-Hugoniot conservation equations for shock waves in solids are derived under the assumption of a hydrodynamic state of stress within a solid.

These equations, also referred to as the conservation of mass, momentum and energy relations, represent three equations that relate the five variables: pressure

(P), particle velocity (u_p), shock velocity (U_s), density (ρ), and energy (E)

(The Rankine-Hugoniot equations were listed in Appendix B). Hence, an

additional equation is needed to determine all parameters as a function of one of

them (Kinslow, 1970). This fourth equation, which can be conveniently expressed

as the relationship between shock and particle velocities, has to be experimentally determined.

This relationship between shock velocity (U_s) and particle velocity (u_p) can be described by a polynomial equation of the form

$$U_s = C_0 + S_1 u_p + S_2 u_p^2 + \cdots, \quad (4.2)$$

where, S_i are experimental determined parameters and C_0 is the sound velocity in the material at zero pressure. For most materials, the Equation of State (EOS) can be approximated as a linear relationship between the shock velocity and the particle velocity (U_s vs. u_p) given by

$$U_s = C_0 + S u_p. \quad (4.3)$$

It is important to note that if there is porosity or phase transitions in the material, or if material underwent large elastic-plastic deformations the linear EOS is no longer applicable and has to be modified (Meyers, 1994).

For the GRP, the shock velocity vs. particle velocity data obtained from a series of plate impact experiments conducted on the GRP specimens in the present study, are shown in Figure 4.14. The shock velocity was estimated from the thickness of the GRP specimens and the shock arrival times. In Figure 4.14 the abscissa represents the particle velocity while the ordinate represents the shock velocity. The white circles represent the data points before taking experiments' tilt data into consideration in the calculation of the shock velocity while the black squares represent the data points after the tilt adjustments have been applied. The effect of tilt on the shock velocity calculations is quite evident, especially at lower impact velocities where the tilt time measurements are relatively larger. The linear fit for the EOS for the GRP under investigation in the present study is determined to be

$$U_s = 3.224 + 0.960u_p . \quad (4.4)$$

Figure 4.15 shows the EOS data for GRP specimens from this research and from Dandekar *et al.* (2003). It also shows the EOS data for the GRP constituent materials, S2-Glass and polyester. The data from this work and Dandekar *et al.*

(2003) showed that when the shock stresses are below 3.0 GPa, the EOS is essentially linear and lies between the EOS of S2-Glass and the polyester. The slope of the shock velocity vs. particle velocity line in the present study is not as steep as that obtained by Dandekar *et al.* (2003). Moreover, the slope of the EOS for GRP is smaller than the EOS for the two constituents, i.e. the S2-Glass and polyester. This is probably because in monolithic materials, i.e. in S2-Glass and polyester, there are much fewer defects (e.g. voids, complex polymer/glass interfaces etc.) when compared to those in the GRP. Hence, during propagation of shock waves, the GRP is not able to carry the same level of shock stress when compared to the S2-Glass or polyester as the particle velocity is increased.

In an effort to estimate GRP's Equation of State for a larger range of shock stresses, the data points from Dandekar and Hall *et al.* (2003) were combined with the data from the present study, as shown in Figure 4.16. The linear fit for the three sets of experiments showed that the relationship between shock

velocities and particle velocities in GRP for shock stresses from 0.04 GPa to 20 GPa was

$$U_s = 3.228 + 0.996u_p. \quad (4.5)$$

In equation (4.5), $C_0 = 3.228$ km/s, which is close to the ultrasonic wave-velocity measurement of 3.21 ± 0.012 km/s in the GRP by Dandekar *et al.* (1998) along the impact direction. The shock velocities, particle velocities, and tilt time data from the present study are listed in Table 4.2.

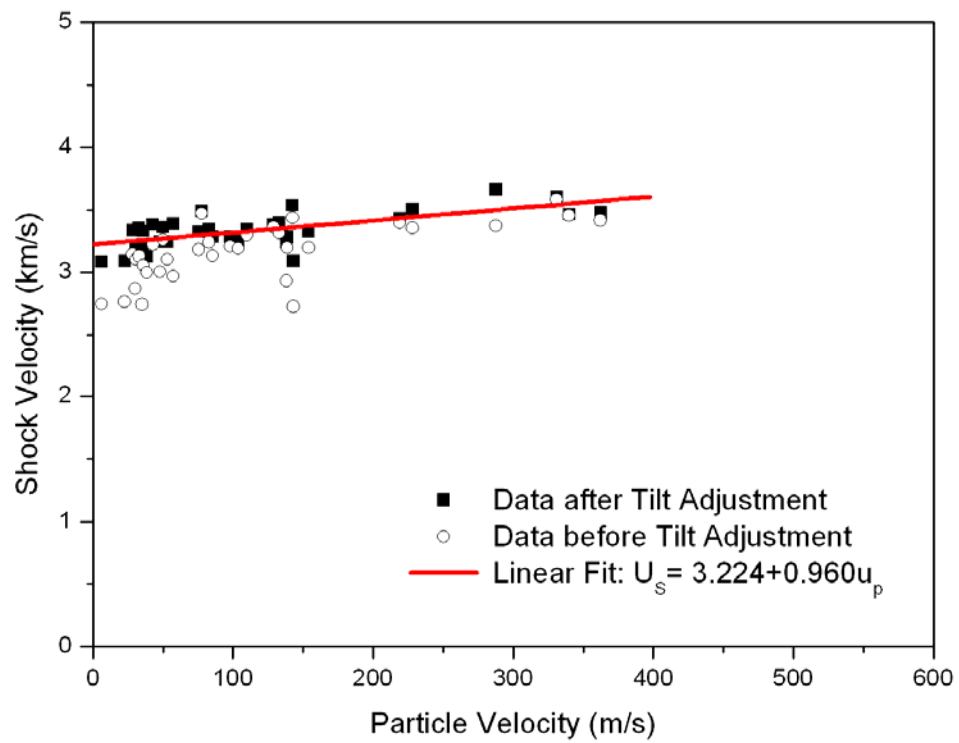


Figure 4.14: Shock velocity vs. Particle velocity of GRP materials for this work. The effect of tilt to shock velocity during impact is quite clear especially at lower impact velocity.

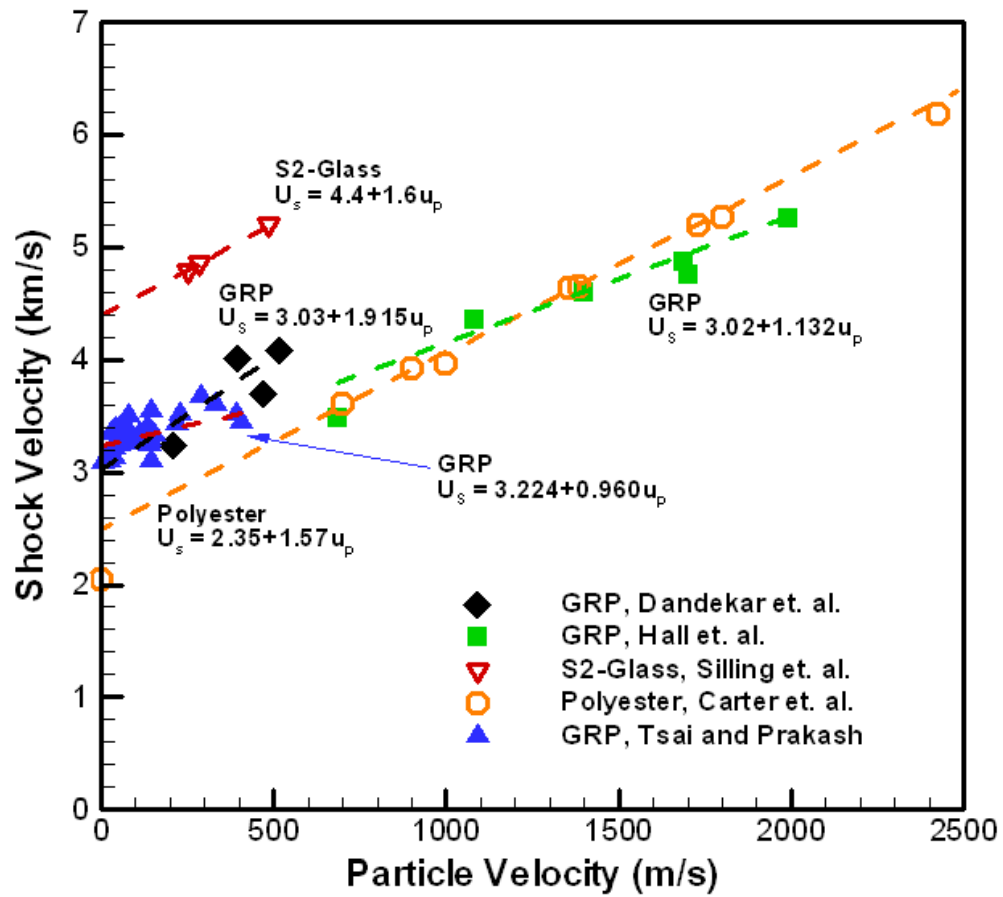


Figure 4.15: Shock velocity vs. Particle velocity for GRP and its component materials: S2 glass and polyester.

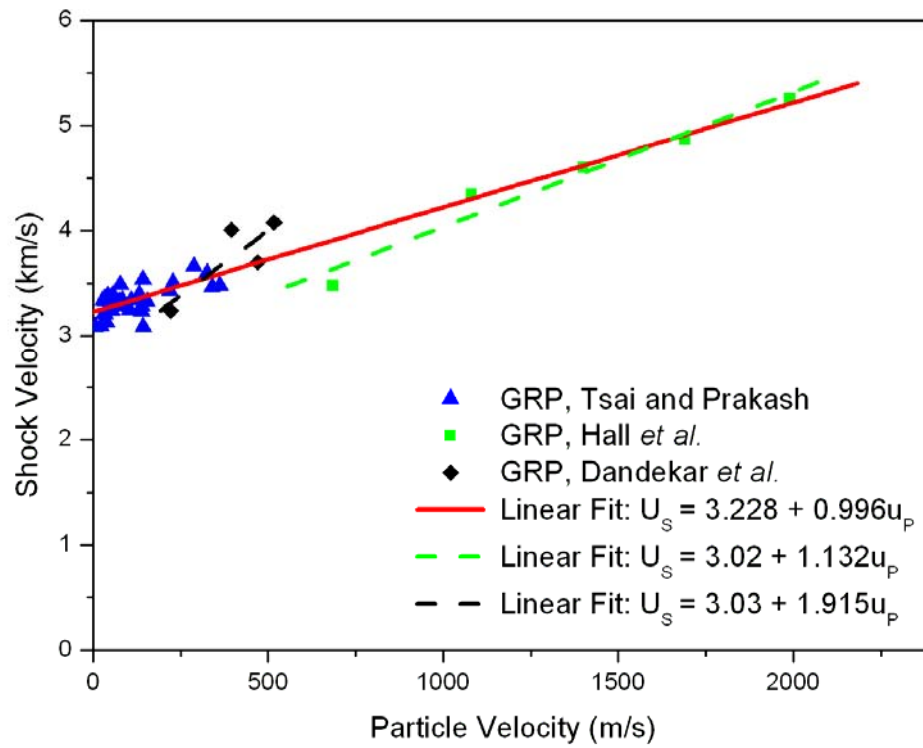


Figure 4.16: Shock velocity vs. Particle velocity for GRP composites.

Exp No.	Free Surface Particle Velocity (m/s)	Calculated Shock Velocity (km/s)	Impact Tilt Time (ns)	Adjusted Shock Velocity (km/s)
LT25	276.54	3.237	184.29	3.237
LT27	277.46	3.283	187.65	3.283
LT28	286.18	3.090	183.98	3.090
LT29	284.97	3.539	191.49	3.539
LT30	171.12	3.285	111.69	3.285
LT31	456.26	3.509	312.70	3.509
LT32	165.80	3.341	113.71	3.341
LT33	437.98	3.430	312.72	3.430
LT35	76.99	3.129	52.5	3.129
LT36	65.85	3.358	43.9	3.358
LT37	56.58	3.339	39.13	3.340
LT38	12.47	3.086	8.5	3.086
LT40	155.31	3.489	108.1	3.489
LT41	307.92	3.327	212.38	3.327
LT42	150.82	3.327	104.7	3.327
LT44	99.91	3.364	68.96	3.364
LT45	71.38	3.331	47.36	3.331
LT46	575.34	3.663	329.13	3.663
LT47	650.28	3.585	367.88	3.602
LT48	679.69	3.453	417.96	3.467
LT49	724.65	3.465	416.96	3.480
LT50	265.51	3.395	188.17	3.395
LT51	257.83	3.385	172.76	3.385
LT52	195.98	3.283	138.86	3.283
LT53	207.47	3.252	133.23	3.252
LT54	219.51	3.341	140.64	3.341
LT55	114.13	3.389	82.86	3.389

Exp No.	Free Surface Particle Velocity (m/s)	Calculated Shock Velocity (km/s)	Impact Tilt Time (ns)	Adjusted Shock Velocity (km/s)
LT56	105.89	3.242	75.75	3.242
LT57	85.65	3.386	59.98	3.386
LT58	61.52	3.212	43.48	3.212
LT59	45.10	3.091	31.95	3.091
LT60	70.26	3.207	48.41	3.207
LT61	95.97	3.244	68.17	3.244

Table 4.2: Shock velocity vs. Particle velocity data for GRP experiments.

4.3.4 Hugoniot Stress vs. Hugoniot Strain (Hugoniot)

From the Rankine-Hugoniot conservation relations, the relationship between stress and strain immediately behind wave front can be established. This stress vs. strain relationship is generally referred to as the Rankine-Hugoniot equation, or simply as the “Hugoniot” (Meyers, 1994). For this reason, the stress and strain immediately behind shock wave front are also referred to as the Hugoniot stress and Hugoniot strain.

A “Hugoniot” is the locus of all the shock states in a material and essentially describes the shock response of a material. As mentioned in previous section, the Hugoniot of a material can be determined as long as its Equation of State is known. From the Rankine-Hugoniot conservation relationships given in Appendix B, the Hugoniot stress σ_H , can be determined from shock velocity U_s and particle velocity u_p , as

$$\sigma_H = \rho_0 U_s u_p. \quad (4.6)$$

Also, the Hugoniot strain, ε_H , can be expressed as

$$\varepsilon_H = 1 - \frac{\rho_0}{\rho}. \quad (4.7)$$

Using the Rankine-Hugoniot conservation of mass, the relationship between mass density, shock velocity, and particle velocity can be expressed as

$$\rho_0 / \rho = (U_s - u_p) / U_s. \quad (4.8)$$

Using Equations (4.7) and (4.8) the Hugoniot strain, ε_H , can be determined from shock velocity and particle velocity as

$$\varepsilon_H = \frac{u_p}{U_s}. \quad (4.9)$$

The Hugoniot stress and Hugoniot strain values, obtained by using the measured shock and particle velocities and Equations (4.6) and (4.9), are shown in Table 4.3 for the experimental data of Hall *et al.* (2003) and Dandekar *et al.* (2003) and Table 4.4 for the data obtained in the present study.

Combining Equations (4.6), (4.9), and the EOS (i.e. Equation (4.3)), the relationship between σ_H and ε_H can be expressed in terms of the sound velocity at zero pressure C_0 , and the empirical constant S , as

$$\sigma_H = \frac{\rho_0 C_0^2 \varepsilon_H}{(1 - S \varepsilon_H)^2} . \quad (4.10)$$

The Hugoniot stress and strain states, obtained using the data from the present experiments and Equations (4.6) and (4.9), are shown in Figure 4.17. The dashed line represents the linear fit to the Hugoniot stress vs. Hugoniot strain data, while the solid line represents the relationship between Hugoniot stress and Hugoniot strain calculated using Equation (4.10) and the EOS determined from Equation (4.5) in the previous section. The concave up shape of Hugoniot curve is more evident in Figure 4.18, which includes the shock data from Dandekar *et al.* and Hall *et al.* (2003) for the evaluation of Hugoniot in higher stress range. Although the data shows good agreement with the linear fit at the lower levels of stress, the calculated Hugoniot stress vs. strain curve more accurately describes the experimental data over the entire range of stress.

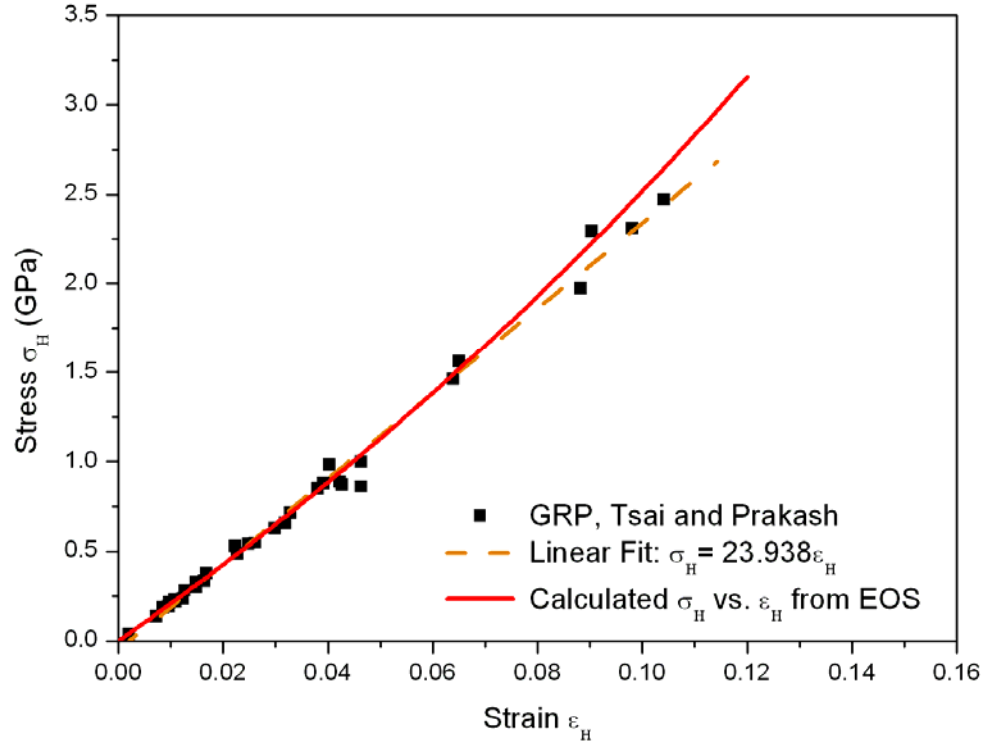


Figure 4.17: Hugoniot stress vs. strain of GRP in the present study. The linear fit indicates that the Hugoniot stress vs. strain follows a linear relationship in the test range.

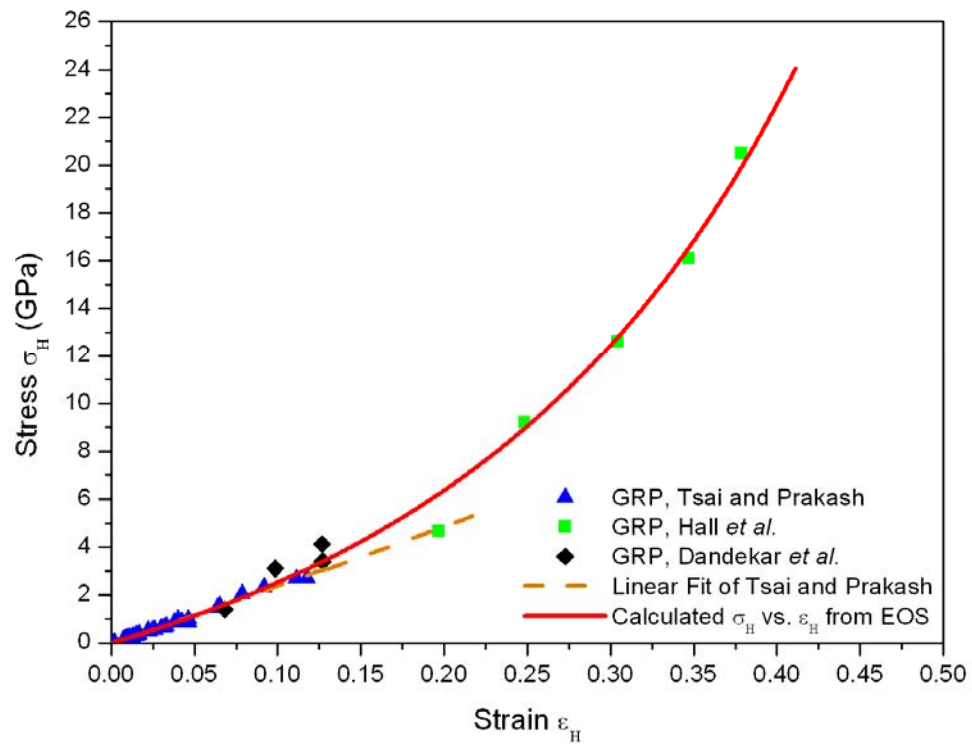


Figure 4.18: Hugoniot stress vs. strain for GRP composites with linear and third order polynomial fit.

Exp No.	Particle Velocity (km/s)	Shock Velocity (km/s)	Hugoniot Stress (GPa)	Hugoniot Strain (%)
Hall <i>et al.</i> in Sandia National Laboratories				
GRP-2	0.685	3.48	4.670	19.684
GRP-3	1.08	4.35	9.203	24.828
GRP-4	1.40	4.60	12.616	30.435
GRP-5	1.69	4.87	16.123	34.702
GRP-6	1.99	5.26	20.506	37.833
Dandekar <i>et al.</i> in Army research Laboratory				
448-1	0.211	3.24	1.403	6.821
438-1	0.395	4.01	3.103	9.850
503-1	0.5168	4.08	4.131	12.667
513	0.4695	3.70	3.403	12.690

Table 4.3: Calculated Hugoniot Stress and Hugoniot Strain for experiment data from Hall *et al.* and Dandekar *et al.*

Exp No.	Hugoniot Stress (GPa)	Hugoniot Strain (%)
LT25	0.877	4.272
LT27	0.892	4.226
LT28	0.866	4.631
LT29	0.988	4.026
LT30	0.551	2.260
LT31	1.568	6.501
LT32	0.543	2.481
LT33	1.471	6.385
LT35	0.236	1.230
LT36	0.217	0.981
LT37	0.185	0.847
LT38	0.038	0.202
LT40	0.531	2.226
LT41	1.003	4.628
LT42	0.491	2.267
LT44	0.329	1.485
LT45	0.233	1.072
LT46	2.064	7.854
LT47	2.294	9.027
LT48	2.308	9.802
LT49	2.470	10.412
LT50	0.883	3.911
LT51	0.855	3.808
LT52	0.630	2.984
LT53	0.661	3.190
LT54	0.718	3.285
LT55	0.379	1.684
LT56	0.336	1.633

Exp No.	Hugoniot Stress (GPa)	Hugoniot Strain (%)
LT57	0.284	1.265
LT58	0.194	0.958
LT59	0.137	0.730
LT60	0.221	1.095
LT61	0.305	1.479

Table 4.4: Hugoniot stresses and Hugoniot strains data for GRP experiments.

4.3.5 Hugoniot Stress vs. Particle Velocity

By utilizing the Rankine-Hugoniot relationship (4.6) and the EOS (Equation (4.3)), the relationship between Hugoniot stress and particle velocity can be written as

$$\sigma_H = \rho_0(C_0 + Su_p)u_p. \quad (4.11)$$

This curve can be determined as long as the sound velocity at zero stress C_0 , and the empirical constant S , in the EOS are known. Figure 4.19 shows the Hugoniot stress vs. particle velocity data from all the GRP experiments conducted in the present study, and from Hall *et al.* (2003) and Dandekar *et al.* (2003). The solid line represents the calculated Hugoniot stress vs. particle velocity curve obtained using Equation (4.11), while the dashed line represents the elastic prediction for the stress and particle velocity based on the elastic acoustic impedance of the GRP. The acoustic impedance was calculated from the sound velocity at zero stress multiplied the initial density of GRP (Dandekar *et al.*, 2003). As predicted, the Hugoniot stress vs. particle velocity curve obtained by using Equation (4.11), conforms well to the various data sets and has the regular concave-up profile observed previously in several other materials. The dashed-line was drawn to

identify the elastic-limit in GRP under the shock loading conditions. Based on their experimental results, Dandekar *et al.* (2003) estimated the HEL for GRP to lie between 1.3 to 3.1 GPa. The reason for the estimate can be better understood from Figure 4.20. It shows the data points from zero to 1 km/s particle velocity, and thus provides a better look at the data points in the lower stress range. The dashed line represents the elastic relationship between stress and particle velocity based on the acoustic impedance of GRP before impact, while the solid line represents the calculated Hugoniot stress vs. particle velocity curve. Because Dandekar *et al.* (2003) show a data point at ~ 1.3 GPa, which is consistent with the elastic estimate, and also a data point above 3.1 GPa that is considerably higher than the elastic estimate, they argued that the HEL for the GRP lies somewhere in between 1.3 and 3.1 GPa.

Combining experimental data from the present research with that of Dandekar *et al.* and Hall *et al.* (2003), the HEL can be identified as the deviation of the elastic

estimate (dashed line) with the Hugoniot stress vs. particle velocity curve, and is estimated to be approximately 1.6 GPa.

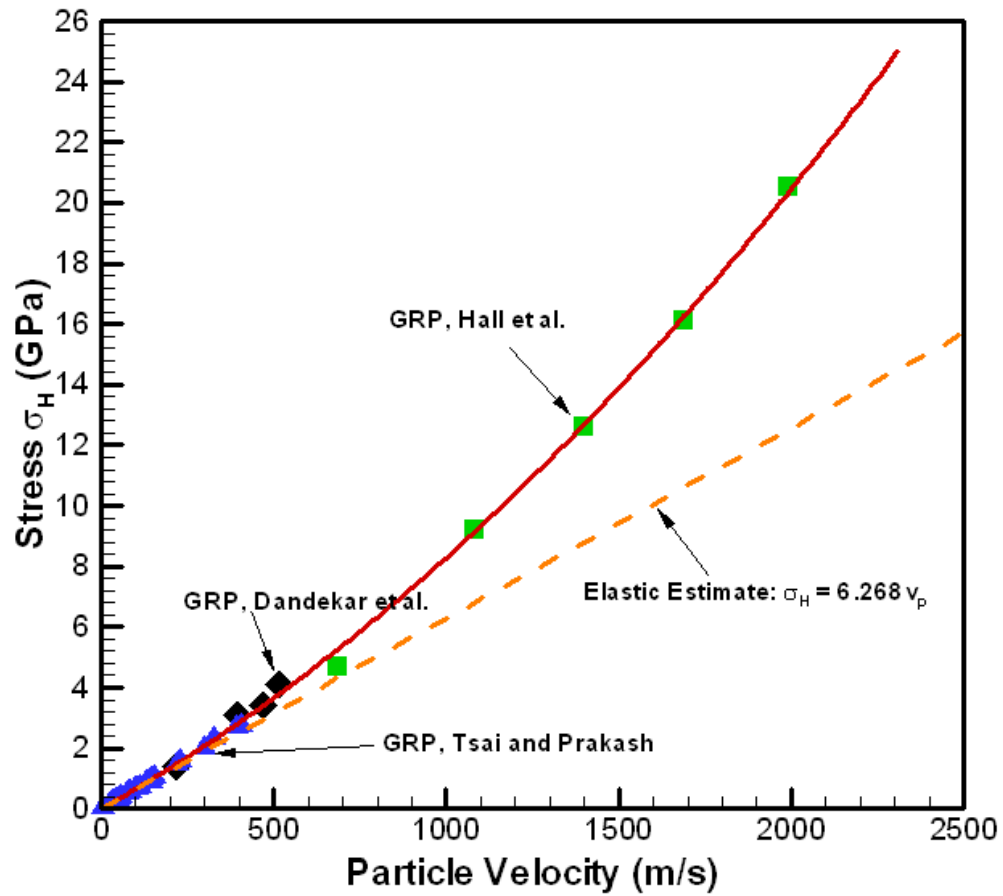


Figure 4.19: Hugoniot Stress vs. Particle Velocity data of GRP materials.

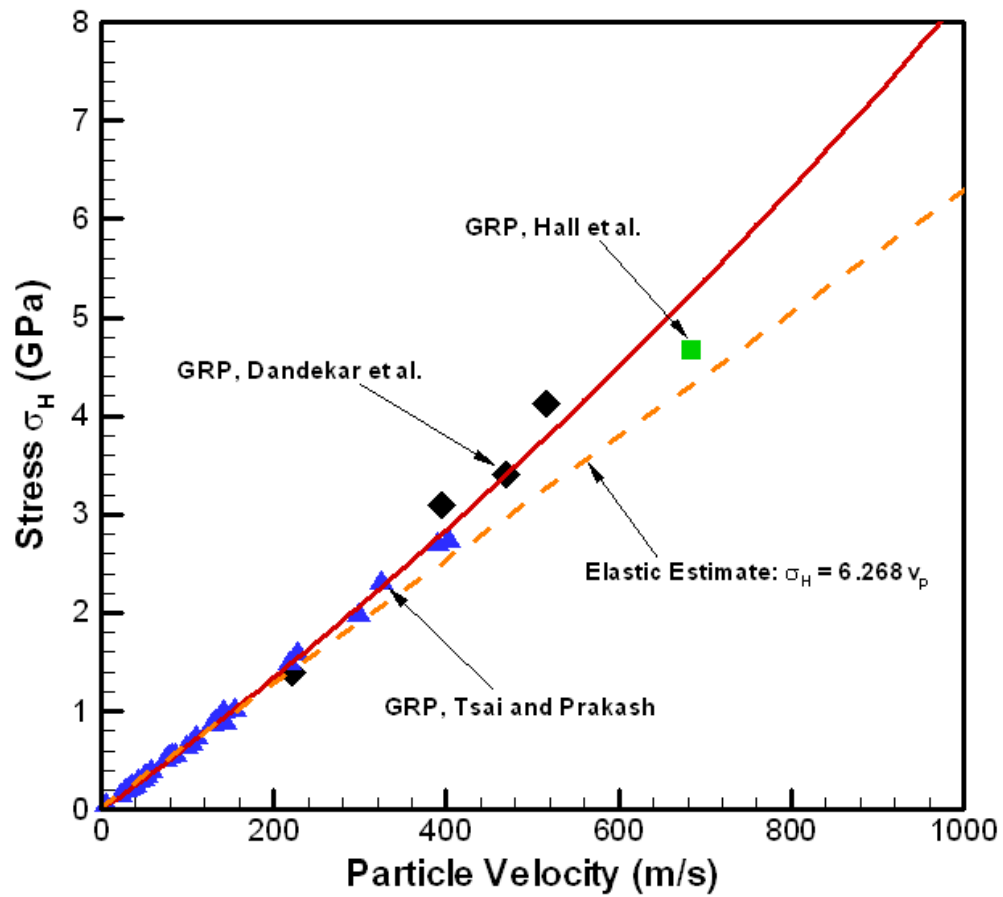


Figure 4.20: Hugoniot Stress vs. Particle Velocity data points of GRP experiments from Tsai and Prakash, Dandekar *et al.*, and Hall *et al.* Only particle velocity data below 1 km/s were shown here to have a better look of the data from this work.

4.4 Summary

A series of plate impact experiments were conducted on S2 glass fiber reinforced polymer composites. The shock response of GRP specimens with four different thicknesses were investigated in stress range between 0.04 ~ 2.60 GPa. The history of the free-surface particle velocity at the rear surface of the target plate was monitored using the VISAR system. Moreover, the dynamic response of the GRP to different shock stress levels was determined. The critical amplitude of the shock waves was found to be between 1.5 and 2.0 GPa. The effect of propagation distance on the structure of shock waves in GRP was found to have limited attenuation, not like the hydrodynamic attenuation effect that was observed by Boteler *et al.* (1999). The shock velocity vs. particle velocity data was gathered and compared with the data from Dandekar *et al.* (2003) and Hall *et al.* (2003); using this data a linear Equation of State for the GRP was determined. The Hugoniot of GRP was calculated using the Rankine-Hugoniot relationships. The Hugoniot of GRP was found to depart from linearity at approximately 1.6 GPa and increased nonlinearly with increasing Hugoniot strain.

The Hugoniot stress vs. particle velocity curve was also determined and the

Hugoniot Elastic Limit of GRP was approximated to be 1.6 GPa.

REFERENCES

Barker L. M., Lundergan C. D., Chen P. J., Gurtin M. E., 1974. "Nonlinear Viscoelasticity and the Evolution of Stress Waves in Laminated Composites: A Comparison of Theory and Experiment", *Journal of Applied Mechanics*, 1974, 1025-1030.

Boteler J. M., Rajendran A. M., and Grove D., 1999. "Shock Wave Profiles in Polymer Matrix Composite", *Shock Compression of Condensed Matter*, 1999, 563-566.

Dandekar D. P., Boteler J. M., and Beaulieu P. A., 1998. "Elastic Constants and Delamination Strength of a Glass-Fiber-Reinforced Polymer Composite," *Composite Science and Technology*, 58, 1397-1403.

Dandekar D. P., Hall C. A., Chhabildas L. C., Reinhart W. D., 2003. "Shock Response of a Glass-Fiber-Reinforced Polymer Composite," *Composite Structures*, 61, 51-59.

Jones R. M., 1999. *Mechanics of Composite Materials*, Taylor & Francis, Philadelphia.

Kaw A. K., 1997. *Mechanics of Composite Materials*, CRC Press, New York.

Kinslow R., 1970. *High-Velocity Impact Phenomena*, Academic Press, New York.

Meyers M. A., 1994. *Dynamic Response of Materials*, John Wiley & Sons, Inc, New York.

Neubrand A. and Roedel J., 1997. "Gradient materials: An overview of a novel concept," *Zeitschrift fuer Metallkunde*, 88, 358-371.

Sve C., 1972. "Stress Wave Attenuation in Composite Materials", Journal of Applied Mechanics, 1972, 1151-1152.

Chapter 5

SPALL STRENGTH OF S2 GLASS FIBER REINFORCED POLYMER COMPOSITE

5.1 Introduction

S2-Glass Fiber Reinforced Polymer Composite (GRP) represents a major component in the US Composite Integral Armor (CIA) for the Future Combat Systems (FCS) program of the US Army (DeLuca *et al.* 1998; Fink, 2000). Due to its light weight and good ballistic resistance, GRP has been chosen in composite integral armor as the main structural support behind the ceramic plates to reduce bending failure (Gama, 2001). However, although GRP has excellent strength along the glass fiber reinforcement directions, the cohesion between the glass layers and the resin matrix is not strong, and spall usually occurs during a typical impact process. Spallation is the failure of material due to the action of tensile stresses developed in the interior of a sample through the

interaction (overlap) of two release waves (Gray III, 2000) or more specifically the process of internal failure or rupture of continuum media through a mechanism of cavitation/decohesion due to stresses in excess of the tensile strength of the material (Grady and Kipp, 1993). It was first studied by Hopkinson in the beginning of the 20th century (Meyers, 1994). In the early 1950s Rinehart (1951) found that a critical level of tensile stress was required to produce spall in materials, which is now called the Spall Strength.

Plate impact experiments have been employed in the past to study the spall strength of engineering materials. The main advantage of these experiments is that plane-waves of tensile loading are employed in the estimation of spall strength. Consequently, the applied tensile loading is homogeneous in the central part of the specimen during the time duration of interest. Upon impact, dynamic failure is facilitated by the process of micro-crack formation and growth and/or void nucleation and coalescence. The maximum tensile stress that the material can withstand without failure is referred to its spall strength.

Spall strength of glass-fiber reinforced polymer composites tend to be low because of the weak bonding at the interfaces between the woven-glass-layer and the epoxy matrix. Plane impact experiments have been performed to obtain the spall strength of glass fiber reinforced polymer composite by Dandekar *et al.* (1998) and Zaretsky *et al.* (2004). Dandekar *et al.* (1998) utilized Al 6061-T6 flyer plate to impact S2 glass woven roving with Cycom 4102 polyester resin. Zaretsky *et al.* (2004) also utilized Al 6061-T6 flyer plates to conduct plate impact experiments on woven glass fiber reinforced composites with epoxy 7781 resin. The spall strength was observed to vary dramatically from 0.06GPa (Dandekar *et al.*, 1998) to about 0.19 GPa (Zaretsky *et al.*, 2004) with the resin content.

In the present study, a series of plate impact spall experiments were performed on a S2-glass fiber reinforced polymer composite (GRP). The GRP specimens were shock loaded by utilizing Al 7075-T6 flyer plates to around 1 GPa; the target thickness for each experiment was carefully designed to produce a state of tension near the center of the GRP target plates. Normal plate impact, and

combined pressure and shear experiments with skew angles ranging from 12° to 20° , were performed to study the effects of normal compression and combined compression and shear on the GRP's spall strength. The skew angle of impact resulted in a maximum shear strain of 0.615% during the combined pressure and shear loading. The measured spall strength as a function of the applied shear strain and the normal stress was used to develop a 3-dimensional failure surface.

5.2 Details of the Experimental Configuration and Setup

In the present study plate-impact experiments were conducted utilizing the 82.5mm bore single-stage gas gun facility at the D. K. Wright laboratory at Case Western Reserve University. The experiment involves the impact of a metallic flyer-plate (Al 7075-T6) with the GRP target material at both normal and oblique incidence. Figure 5.1 shows a schematic of the experimental setup. The fiberglass projectile carrying the Al 7075-T6 flyer plate was accelerated down the 82.5mm bore smooth gun barrel by means of compressed Helium gas to the desired impact velocity. The Al 7075-T6 plates were used as the flyer material for

all the shock compression experiments to ensure that the flyer plate remained elastic during impact. The GRP targets were held in aluminum target holders; these target holders are also designed to provide the trigger signal for the data recording systems, as shown in Chapter 4. In order to reduce the possibility of an air cushion between the flyer and target plates, impact takes place in a target chamber that has been evacuated to 50 μm of Hg prior to impact. A laser based optical system utilizing a UNIPHASE Helium-Neon 5mW laser (Model 1125p) and a high frequency photo-diode is used to measure the velocity of the projectile. To ensure the generation of plane waves with wave-front sufficiently parallel to the impact face, the GRP targets and the Al 7075-T6 flyer plates were carefully aligned to be parallel to within 2×10^{-5} radians by using an optical alignment scheme. The actual tilt between the two plates is measured by recording the times at which four, isolated, voltage-biased pins, that are flush with the surface of the target plate, are shorted to ground. The acceptance level of the experiments is of the order of 0.5 mrad. The free surface velocity profiles were recorded using A VALYNTM VISAR laser interferometer system with velocity per

fringe constant set to 99.2 for all the experiments. A COHERENT™ VERDI 5 Watt solid-state diode-pumped frequency doubled Nd:YVO₄ CW laser with wavelength of 532 nm is used to provide a coherent monochromatic light source. The flyer and target plates were lapped to be within 1 micron flatness and the thicknesses for the flyer and target plates were all kept to be about 13 mm.

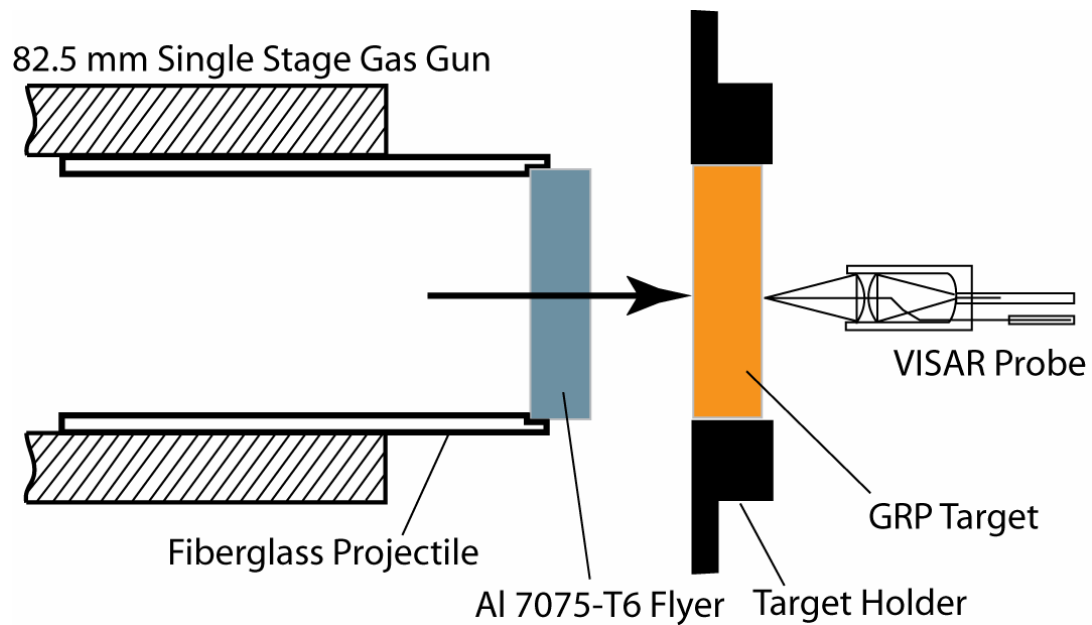


Figure 5.1: Gas Gun experiment setup for normal impact spall experiments with Al 7075-T6 flyer plate.

The Plate Impact Pressure-Shear Experimental Configuration and Set-up

In the present study plate-impact pressure-shear experiments were conducted to investigate the effects of combined normal and shear loading on the spall strength of the GRP. Figure 5.2 illustrates the experimental setup for the pressure-shear experiments. The flyer plates with a skew angle of 12° , 15° , or 20° were machined from a 3 in diameter Al 7075-T6 bar. These flyers were employed to subject the GRP specimens to various ratio of the normal to shear stress. The rear end of the projectile had a sealing O-ring, and a plastic (Teflon) key that slides in a key-way inside the gun barrel to prevent rotation of the projectile. The thickness of the flyer plates and the GRP target plates were carefully chosen so as to subject the center of GRP plate to a tensile state of stress following the combined pressure and shear loading.

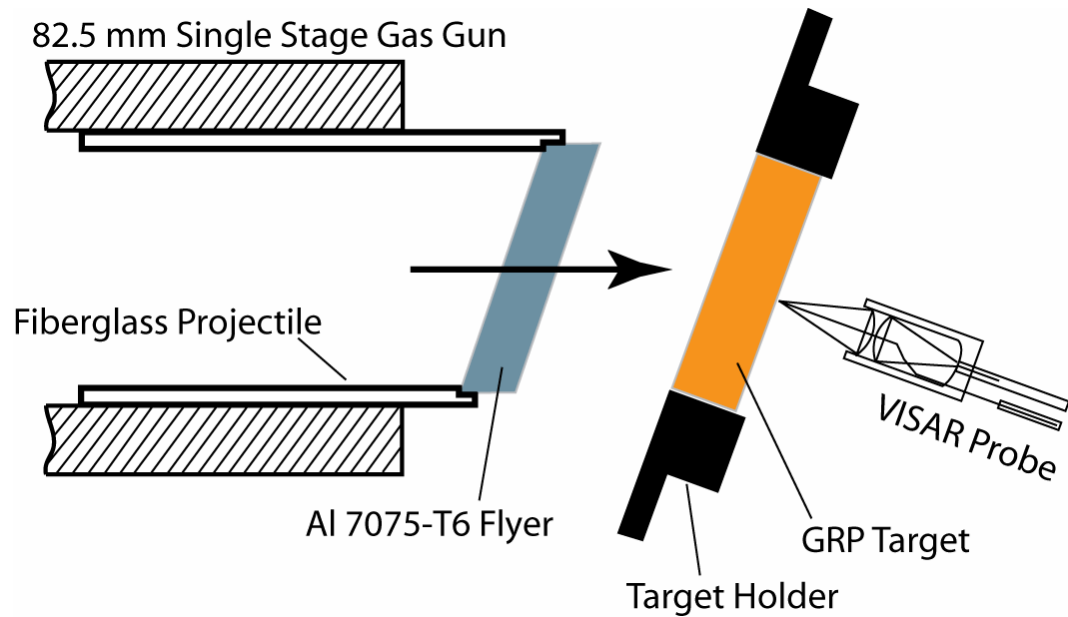


Figure 5.2: Pressure-shear experiment setup for spall experiments.

5.3 t-X diagram (Time vs. Distance) & S-V diagram (Stress vs. Velocity)

A schematic of the t-X (time vs. distance) diagram, which illustrates the propagation of compression waves and tensile waves through the target and flyer plates during the plate impact spall experiments, is shown in Figure 5.3. The abscissa represents the distance in the target and the flyer plates from the impact surface -- the positive direction represents the distance into the GRP target plate while the negative direction represents the distance into the Al 7075-T6 flyer. The ordinate represents the time after impact. The arrows indicate the direction of wave propagation; the letter "T" indicates a resulting tensile state of stress

while “C” indicates a compressive state of stress. When the release waves from the flyer and the target free surface meet, as shown, near the center of the GRP target, a tensile state of stress is developed (state(7)) that may lead to delamination of the GRP target.

The S-V (stress vs. velocity) diagram details the locus of all the stress and particle-velocity states that can be attained during a typical plate-impact experiment. It illustrates the stress and particle velocity in the various shock states depicted in Figure 5.3. The abscissa represents the particle velocity in the target and the flyer plates, while the ordinate represents the stress in the target and flyer. For the case in which the spall strength is greater than applied the tensile stress, the stress and particle velocity in the GRP moves along the dashed lines from State 5 to the no-spall state denoted by State 7. However, if the tensile stress is greater than the spall strength of the GRP (σ_{spall} indicated by the short dashed lines), the GRP will spall and the tensile stress in State (7) will unload to the stress free state denoted by State (7'). The compressive “end of spall” wave

from State (7') arrives at the free surface of the GRP, and brings the free surface velocity to State (10), which is the same as that in State (6) and also in State (7'). The free surface particle velocity in States (6,7', and 10) is referred to as V_{\max} , and the corresponding free surface particle velocity in State (8) is named V_{\min} . The spall strength (σ_{spall}) can then be calculated from the measured free surface particle velocities V_{\max} and V_{\min} by

$$\sigma_{\text{spall}} = Z_{\text{GRP}} (V_{\max} - V_{\min}) / 2. \quad (5.1)$$

In Equation (5.1), $Z_{\text{GRP}} = 6.268 \text{ GPa-mm}/\mu\text{s}$, which represents the acoustic impedance of the GRP in the zero stress condition.

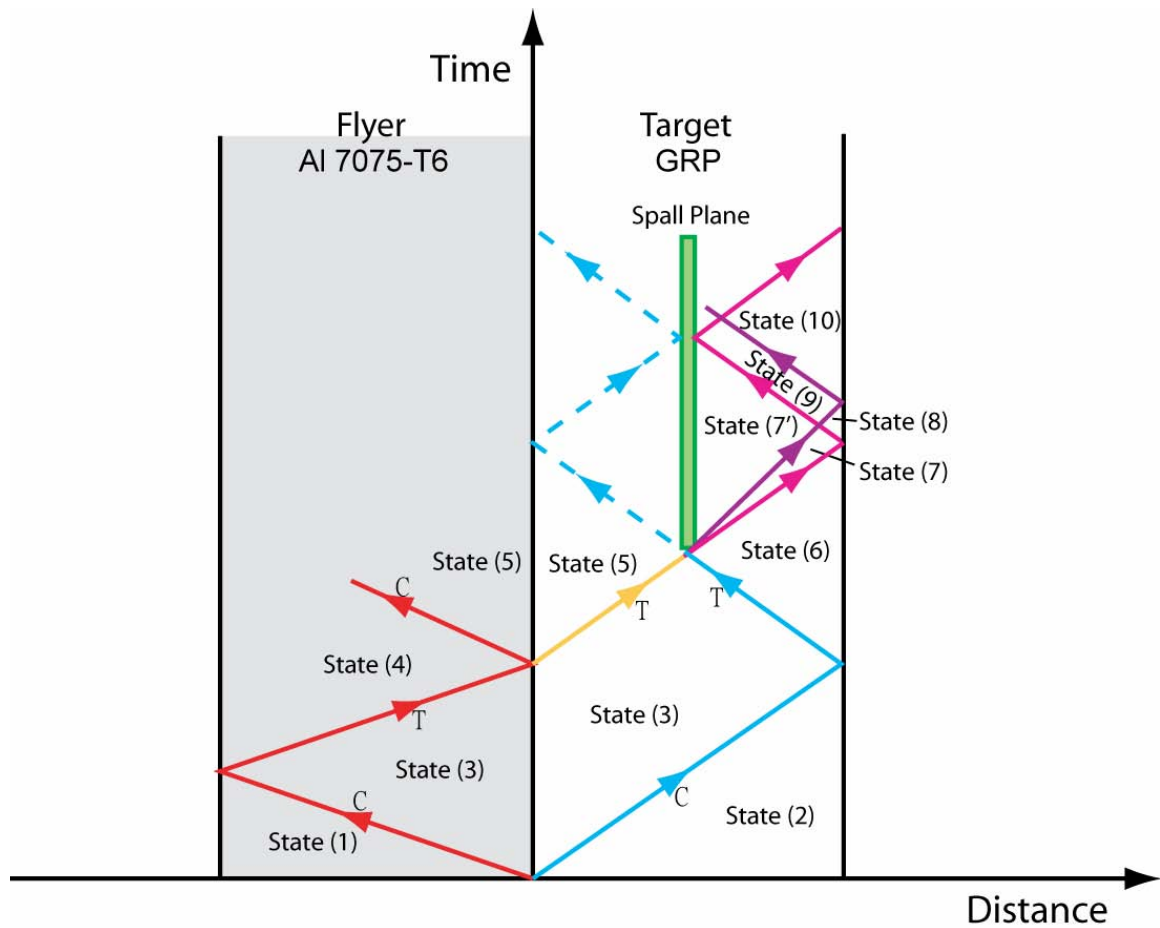


Figure 5.3: Time-distance diagram for spall strength experiments. State (7) indicates the tensile stress state after the tensile waves met at the spall plane and state (7') indicates the free surface state after the GRP targets completely separated at the spall plane.

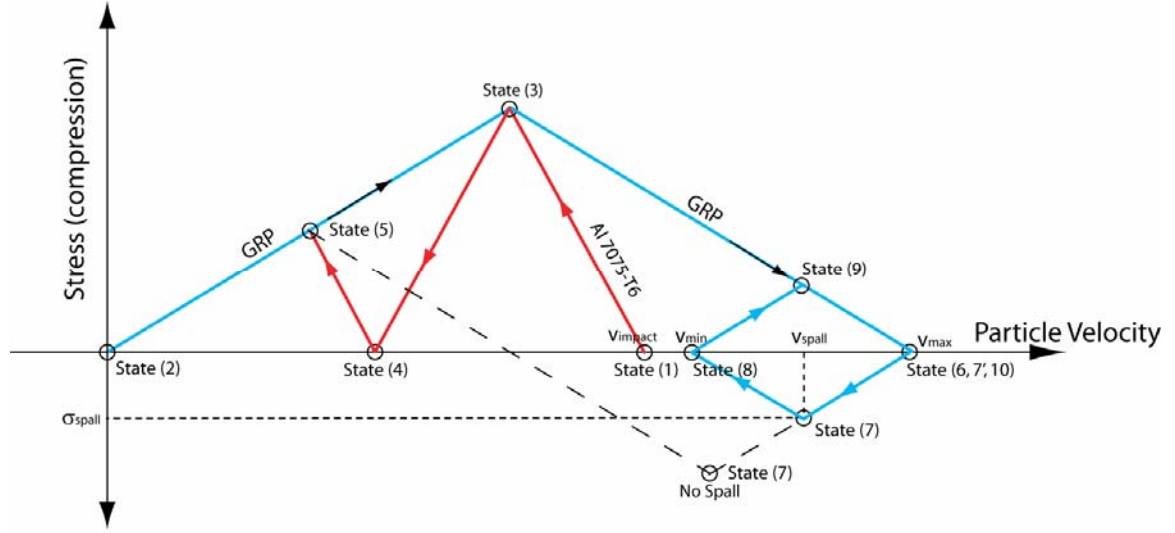


Figure 5.4: Stress-Velocity diagram for spall experiments with Al 7075-T6 flyer.

5.4 Experiment Results

In the present study, eleven normal plate impact experiments and eleven pressure-shear plate impact experiments were conducted to investigate the spall strength of GRP. The applied impact stresses ranged from 0.04 to 1GPa while the shear strain varied from 0 to 0.615%. Selected experimental data obtained from these experiments are described in the following section. The section provides details of the spall pull-back signal, the calculation of the spall strength, and the effects of normal stress and the shear strain on the spall strength.

5.4.1 Spall Pull-Back Signal

Figure 5.5 shows the measured free-surface particle velocity and the T-X diagram for Experiment LT36. The abscissa represents the time after impact while the ordinate represents the free surface particle velocity measured at the rear surface of the GRP target. At time T_1 , when the compression wave arrives at the free (rear) surface of the GRP plate, the particle velocity increases to a level of V_{\max} , which is consistent with the Hugoniot State corresponding to the impact velocity used in the experiment. At time T_2 , the release waves from the back of the target and the flyer plates intersect at the middle of the GRP plate; the corresponding “unloading tensile wave” and the “end of spall compressive wave” propagate and arrive at the free surface of the GRP plate at times T_3 and T_4 , respectively. At time T_3 , the particle velocity at the free surface of the GRP plate starts to decrease, and at time T_4 , it reaches a level V_{\min} . Eventually the particle velocity recovers to its Hugoniot state level of V_{\max} . This decrease in the particle velocity followed by a recovery is also called the “pull-back” characteristic of the spall signal, and is useful in the calculation of the material’s spall strength, as detailed in the next section.

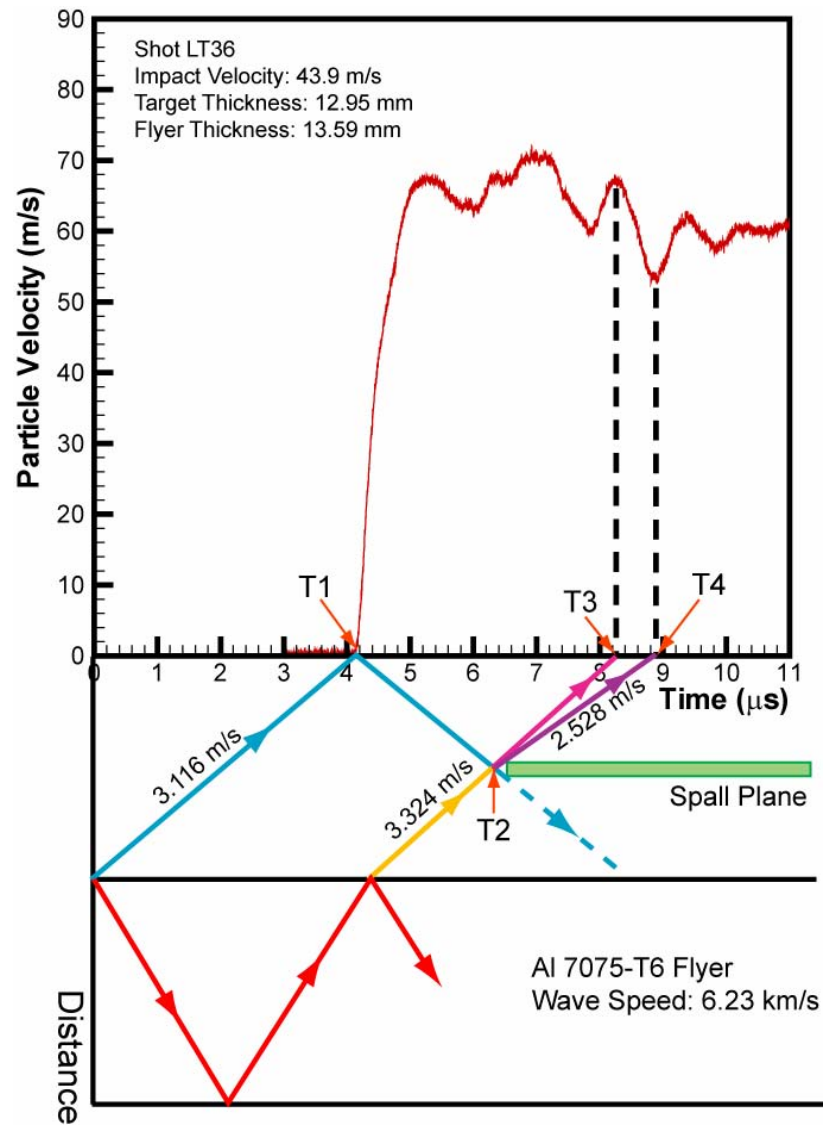


Figure 5.5: Time-Distance diagram paired with experiment LT36 to illustrate the “pull-back” phenomenon in free surface velocity profile.

5.4.2 Calculation of the Spall Strength

The calculation of the spall strength of the GRP from the measured free surface particle velocity requires the estimation of the magnitude of the pull back signal from the measured free-surface particle velocity profile. However, due to the inherent heterogeneity of the GRP, the free surface particle velocity profile is oscillatory, making it difficult to estimate the pull-back signal from the measured particle velocity profile. Hence, a data from a spall experiment was considered to be valid only when the pull back signal was stronger than the amplitude of the oscillations in the particle velocity versus time profile in the equilibrium state. The method applied for calculating the spall strength is illustrated in Figure 5.6. The free surface velocity data for experiment LT36 is used as an example. The abscissa represents the time after impact and the ordinate represents the free surface velocity measured by VISAR system. Due to the oscillatory nature of the Hugoniot particle velocity state in GRP, V_{\max} was taken as the average velocity during the Hugoniot state. After the spall event, the particle velocity dips to V_{\min} followed by a pull back to V_0 . In most of the spall experiments conducted in the present study, $V_0 = V_{\max}$; however in certain experiments V_0 was observed to be

smaller than V_{\max} , indicating the occurrence of partial spall (Shazly and Prakash, 2004). For the case in which there was no spall, the free surface particle velocity remained at its steady state level of $V_{\text{no-spall}}$. Thus, assuming elastic material behavior, the spall strength in the GRP could be estimated using Equation (5.1),

$$\begin{aligned}\sigma_{\text{spall}} &= Z_{\text{GRP}} (V_{\max} - V_{\min}) / 2 \\ \text{as:} \quad &= 6.237 (64.66 - 53.15) / 2 \\ &= 35.89 \text{ MPa}\end{aligned}$$

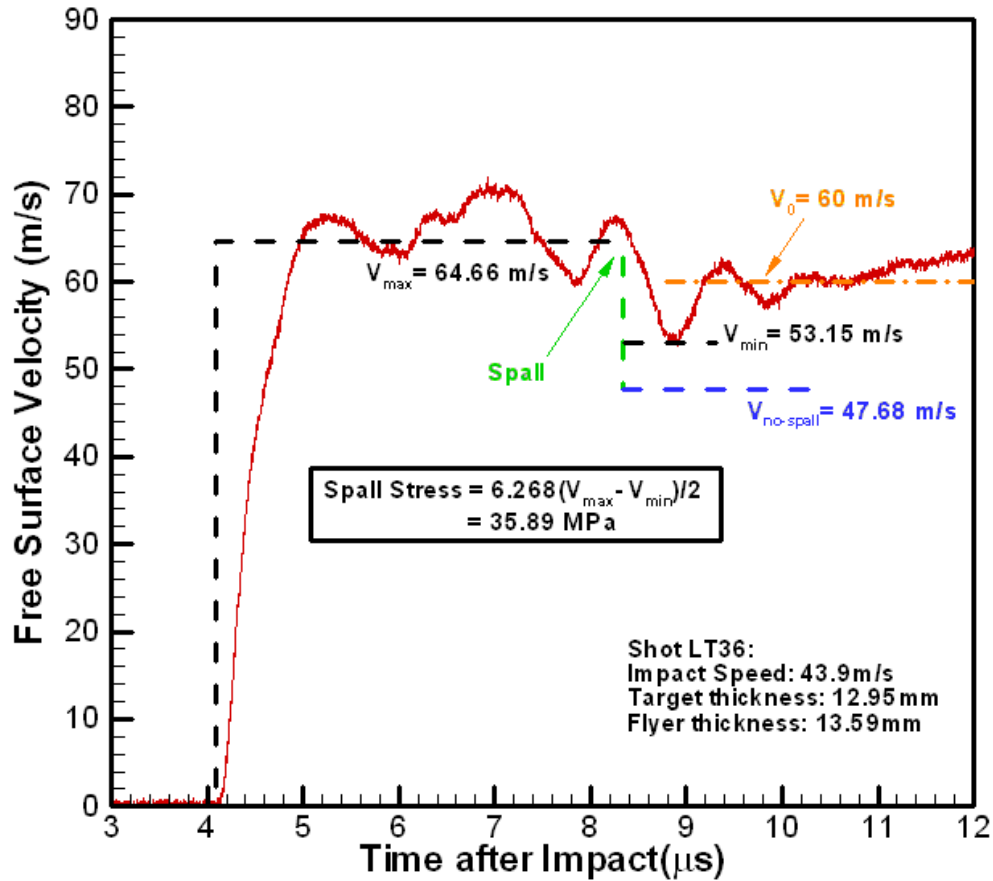


Figure 5.6: Free Surface Velocity data of experiment LT36. This figure specifically illustrated the method used to calculate the spall strength.

5.4.3 Effect of Normal Stress on the Spall Strength of GRP

To determine the effect of normal stress on the spall strength of GRP, a series of normal plate impact experiments were performed in the present study. Table 5.1 provides the details of these experiments along with the estimated spall strength for each experiment. Figure 5.7 shows the free surface velocity profiles of two typical normal plate impact experiments, LT36 and LT37. The abscissa represents the time after impact and the ordinate represents the free surface particle velocity. The impact velocities for Experiments LT36 and LT37 were 43.9m/s and 39.13m/s, respectively. The spall strength estimated for Experiments LT36 and LT37 were 35.89MPa and 46.09MPa, respectively. It is interesting to note that for such a relatively small change in impact velocity the effect on spall strength is quite dramatic. It is also noticed that the duration of the pull back signal is longer in the lower impact velocity experiment LT37 when compared to the experiment LT36. This can be explained by arguing that perhaps at lower impact velocities the time kinetics for the spall (material separation) process are slower when compared to that at the higher impact speeds.

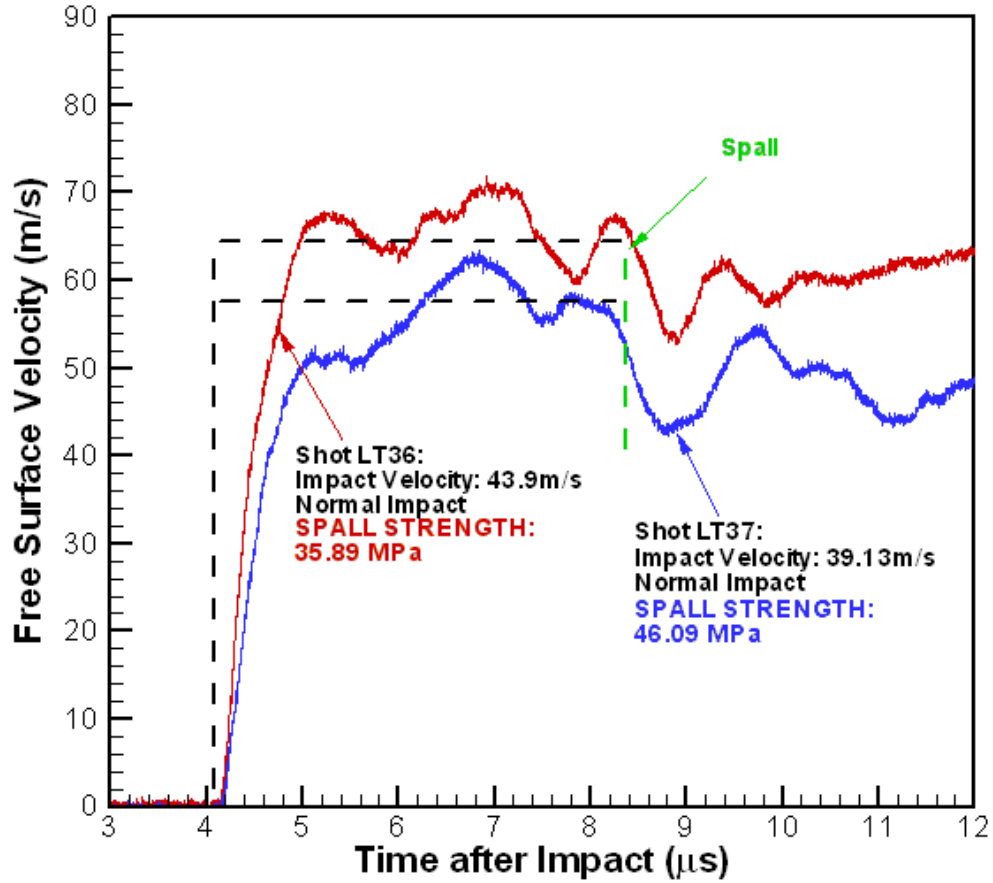


Figure 5.7: Free Surface Velocity data for experiments LT36 and LT37. The effect of normal stress to spall strength was compared between the two experiments.

5.4.4 Effect of Shear Stress on the Spall Strength

To determine the effects of shear stress on the spall strength of the GRP pressure-shear experiments at skew angles of 12° , 15° , and 20° were conducted at various impact velocities in the present study. Table 5.2 provides the details of

these pressure-shear experiments along with the estimated spall strength for each experiment. To illustrate the effect of shear stress on the spall strength, the results of one normal impact and one oblique impact are shown in Figure 5.8. The figure shows the free surface particle velocity profiles for a normal plate impact experiment LT37, and a 15° pressure-shear experiment LT43. The normal component of the stress generated by impact in the two experiments, LT37 and LT43, were 179.76MPa and 187.97MPa, respectively. The shear-strain in the pressure shear experiment LT43, was 0.245%. The shear strain were calculated by using the analysis presented by Dandekar *et al.* (1998)

$$\eta_{13} = \frac{\sigma_{33}'}{\frac{\rho_0}{\rho} \left\{ C_{11} \sin^4 \theta + C_{33} \cos^4 \theta + \left(\frac{1}{2} C_{13} + C_{44} \right) \sin^2 2\theta \right\}} \sin \theta \cos \theta. \quad (5.2)$$

In Equation (5.2), σ_{33}' is the impact stress along the gun barrel direction and is calculated from the impact velocity and the material impedance mismatch; ρ and ρ_0 are the density of GRP after and before impact, respectively; and the ratio ρ_0/ρ is calculated from the Hugoniot strain in the Hugoniot state; C_{ij} are the elastic constants of GRP and are taken from Dandekar *et al.* (1998); and θ is

the skew angle of pressure-shear experiments. The spall strengths estimated in the two experiments with and without the presence of shear strain, i.e. experiments LT37 and LT43, were 46.09MPa and 33.87MPa, respectively. From these results it is quite evident that the presence of shear-strain decreases the spall strength of GRP dramatically.

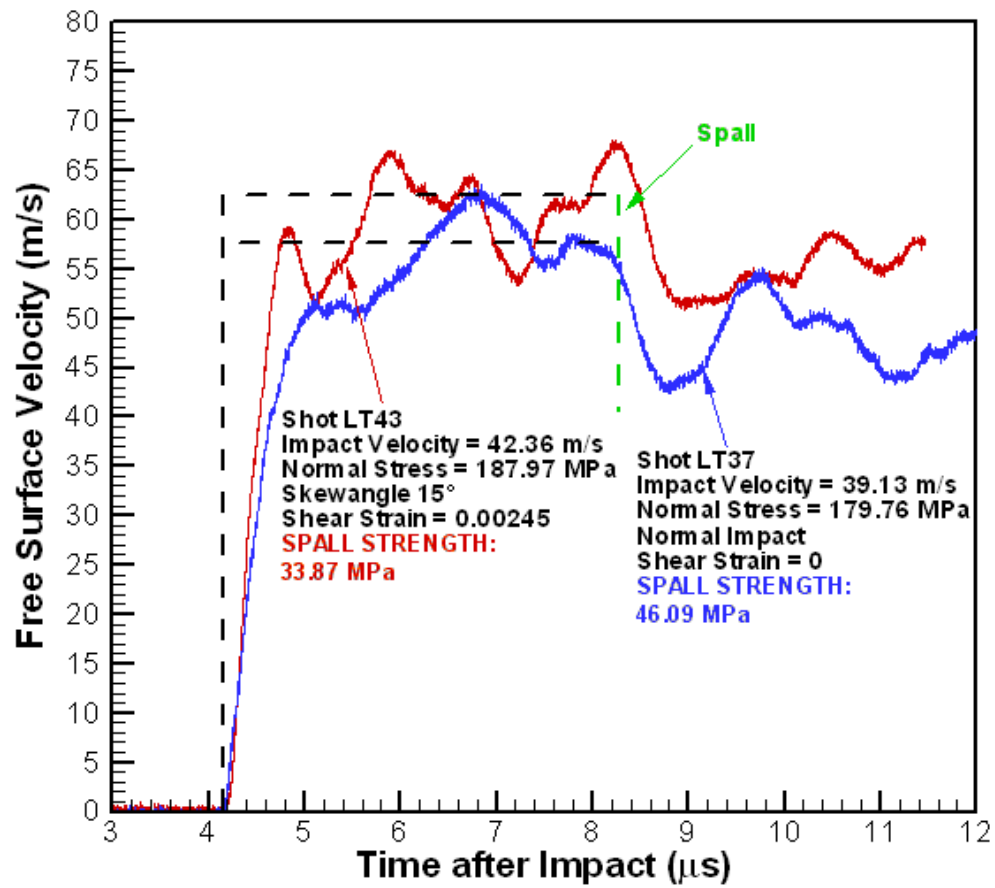


Figure 5.8: Free Surface Velocity profiles for experiments LT37 and LT43. The effect of shear strain on spall strength was emphasized between these two experiments.

5.4.5 Zero Spall Strength Condition

In a number of plate-impact experiments that were conducted at an impact velocity that was higher than a critical level, during shock compression the interface between the woven-glass fiber layers and the polymer resin were weakened to such an extent that the residual spall strength of the GRP was essentially reduced to zero. In these experiments, consistent with the zero spall strength, the pull-back signal was absent in the measured free surface particle velocity profiles. Figure 5.9 shows an example of the particle velocity versus time profiles as measured in a typical zero spall strength experiment and an experiment with a finite spall strength. The measured free-surface particle velocity profiles for the two experiments, one with a finite spall strength (experiment LT36) and the other with zero spall strength (experiment LT45), are shown by the solid blue and red lines, respectively. The impact velocities for experiments LT36 and LT45 were 43.9m/s and 47.36m/s, respectively. Moreover, the experiment LT36 was a normal plate impact experiment while experiment LT45 was conducted at a skew angle of 20° using the pressure-shear plate impact configuration. The impact velocities in the two experiments were controlled so as

to keep the normal stress in the GRP to be nearly the same; the normal stress in experiments LT36 and LT45 were 201.68MPa and 204.45MPa, respectively. The calculated shear-strain for Experiment LT45 was 0.353%. From the measured particle velocity profile of experiment LT45, it can be seen that when the spall signal arrives at the free surface of the GRP target plate, because of the presence of shear strain the spall strength of GRP was reduced to essentially zero, leading to the absence of the pull-back signal in the particle velocity profile. On the other hand, for experiment LT36, the spall strength estimated from the pull back signal and Equation (5.1) was 35.89 MPa.

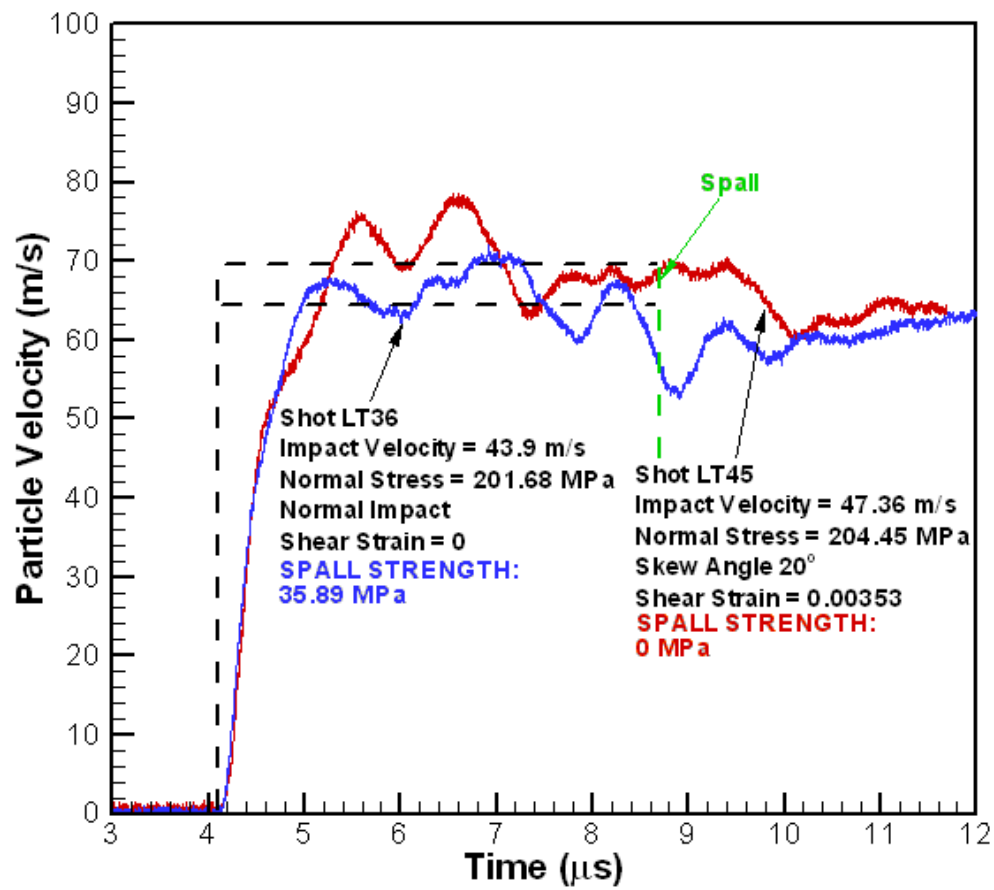


Figure 5.9: Free Surface Velocity profiles for experiments LT36 and LT45. The shear strain in LT45 dramatically decreases the spall strength in GRP.

Exp No.	Impact Velocity (m/s)	Normal stress	Shear Strain (%)	Spall Strength (MPa)
LT36	43.9	201.68	NA	35.89
LT37	39.13	179.76	NA	46.09
LT38	8.5	39.05	Na	NA
LT39	38.12	175.12	NA	NA
LT40	108.1	496.61	NA	45.78
LT41	212.38	975.67	NA	0
LT50	188.17	864.45	NA	0
LT51	172.76	793.66	NA	0
LT52	138.86	637.92	NA	0
LT53	133.23	612.06	NA	0
LT54	140.64	646.1	NA	0

Table 5.1: Summary of the normal impact spall experiments. The spall strength for LT38 and LT39 was not available because, instead of spall, unloading happened in these two experiments.

Exp No.	Impact Velocity (m/s)	Impact Angle (°)	Normal stress	Shear Strain (%)	Spall Strength (MPa)
LT42	104.7	15	464.6	0.615	0
LT43	42.36	15	187.97	0.245	33.87
LT44	68.96	20	297.7	0.516	0
LT45	47.36	20	204.45	0.353	0
LT55	82.86	15	367.69	0.484	0
LT56	75.75	12	340.4	0.359	0
LT57	59.98	12	269.53	0.283	53.7
LT58	43.48	15	192.94	0.252	18.37
LT59	31.95	20	137.93	0.237	22.73
LT60	48.41	12	217.54	0.229	39.64
LT61	68.17	12	306.33	0.323	0

Table 5.2: Summary of the pressure-shear spall experiments.

5.5 Results and Discussion

Figure 5.10 shows the spall strength data collected from all the normal plate impact experiments conducted in the present work and one data point from Dandekar *et al.* (1998). The abscissa represents the impact stress and the ordinate represents the spall strength. Amongst the eight normal plate-impact experiments conducted in the present study (with impact stresses ranging from 39.05 MPa to 975.67 MPa), in two experiments no spall was observed and the particle velocity profiles were observed to unload completely; three experiments showed spall with a finite spall strength.; in the other three experiments (with impact stress greater than 600 MPa), no pull-back signal was observed, indicating that during shock compression the GRP was damaged to such an extent that it could not support any tensile stress, and delaminated with negligible spall strength.

Based on these observations the normal plate-impact spall experiments were placed in three different categories. Experiments in the first category were

conducted at an impact stress between 0 and 175MPa, and the resultant tensile stress was too low to spall the GRP specimens. In these experiments no pull-back signal was observed and the free-surface particle velocity profiles were observed to unload completely after the arrival of the tensile wave. Experiments in the second category were conducted at sufficiently high tensile stress amplitudes so as to spall the GRP specimens (impact stress between 175MPa and 600MPa). In these experiments a clear pull-back signal was observed in the measured free-surface particle velocity profiles. The third category includes experiments in which the amplitude of the incident compression pulse was larger than 600MPa; these relatively high levels of compression stress resulted in enough damage in the GRP specimens such that no resistance to spall was registered in the experiments. The corresponding particle velocity profiles for these experiments show no signs of pull-back or unloading of the particle velocity and remain at the velocity level in the Hugonot state, V_{\max} , throughout the duration of the experiment.

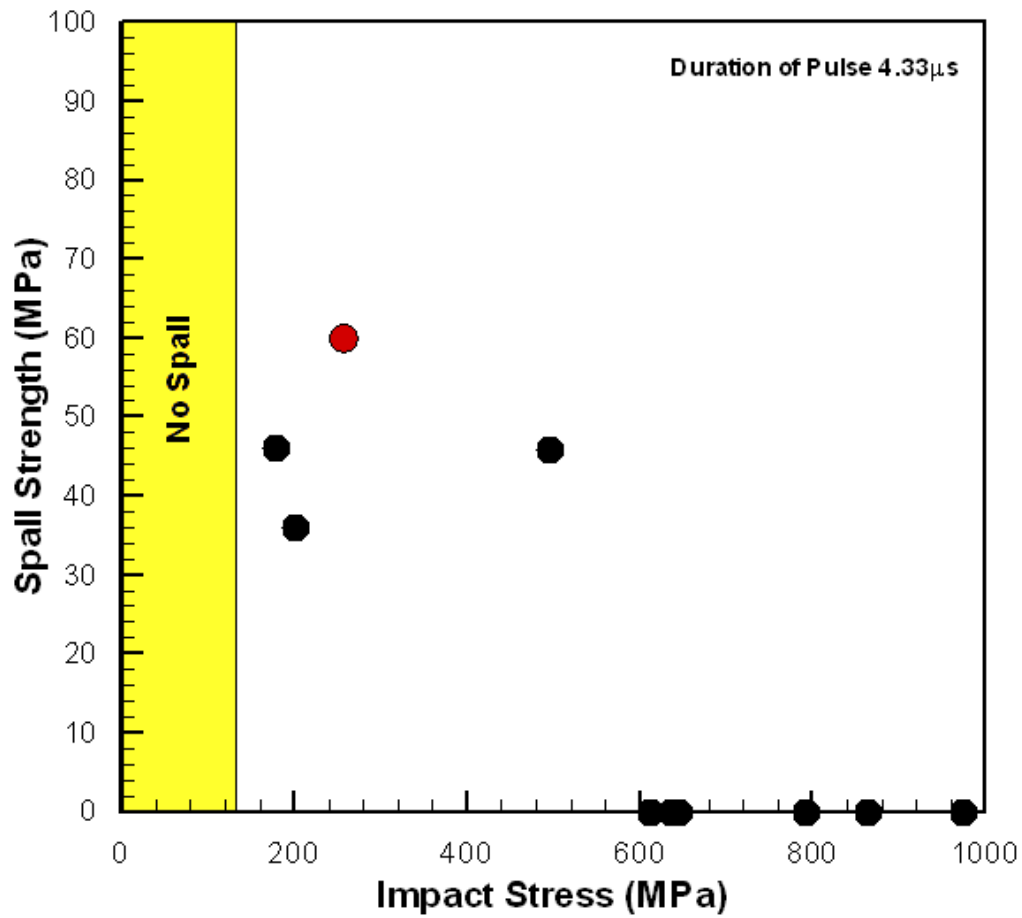


Figure 5.10: Impact stress vs. spall strength data points for normal impact experiments. The red point is from the data acquired by (Dandekar *et al.*, 1998).

Figure 5.11 shows a three-dimensional diagram for the spall strength obtained from all the experiments conducted in the present study as a function of the applied shear-strain and the normal stress. The X-axis represents the normal stress during impact while the Y-axis represents the shear-strain for each

experiment. The Z-axis represents the spall strength. The correlation surface was generated by ORIGINTM with a search radius of 2 and smoothness of 0.5 to illustrate the trend of the spall strength. The surface shows that the spall strength decreases with increasing shear-strain and with increasing normal stress. Moreover, the spall strength is observed to decrease very rapidly at normal stress around 600 MPa and a shear-strain of $\sim 0.3\%$. The maximum spall strength measured in the experiments was 53.7 MPa.

The spall strengths for experiments conducted with zero shear strain (normal impact experiments) are shown in Figure 5.10. Figure 5.12 shows the spall strength versus shear strain plot for the four plate impact spall experiments that were conducted at a normal stress of approximately 200MPa. The abscissa represents the shear-strain while the ordinate represents the spall strength. The experimental data for four different experiments -- LT43, LT45, LT58, and LT60, are shown. Normal stresses in these experiments were 187.97MPa, 204.45MPa, 192.94MPa, and 217.54MPa, respectively. As seen from the figure, the spall

strength in these experiments drops very rapidly from 39.46MPa to essentially zero as the shear strain is increased from 0.229% to 0.353%.

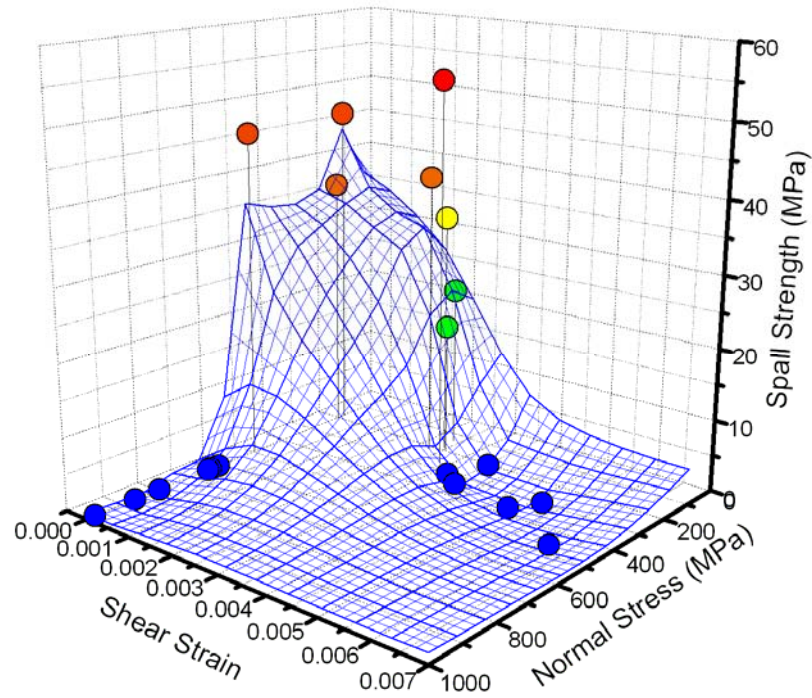


Figure 5.11: Spall Strength illustrated in relationship with normal stress and shear strain.

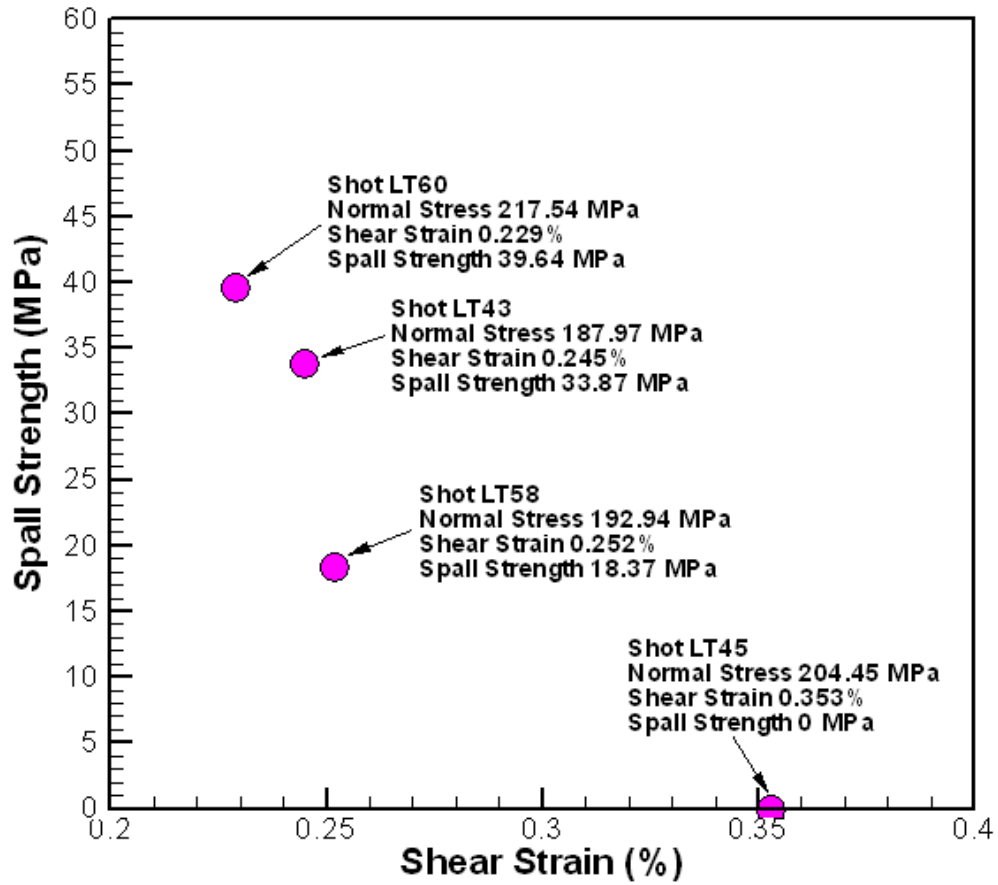


Figure 5.12: Spall strength vs. shear strain figure for selected experiments with normal stress about 200 MPa.

In order to estimate the dependence of the spall strength on the applied shear strain and the normal stress, a non-linear surface was fitted to the experimental spall strength data. The equation that was used for the surface fit was of the form

$$\sigma_{spall} = a \exp \left(-\frac{(x - x_c)^2}{2x_s^2} - \frac{(y - y_c)^2}{2y_s^2} \right). \quad (5.3)$$

The equation was acquired from the Fitting Multiple Independent Variables section of the OriginTM plotting software. The variables x and y represent the shear strain and the normal stress, respectively. The parameter a corresponds to the peak amplitude, and the parameters x_c and y_c represent the center of the peak along the shear strain and normal stress dimensions, respectively.

Parameters x_s and y_s represent the width of the peak along the shear strain and normal stress dimensions, respectively. These parameters were determined as

$$a = 65, x_c = 0.001, x_s = 0.002, y_c = 250, y_s = 250.$$

The result of the surface generated by using Equation (5.3) is shown in Figure 5.13. The surface fit adequately captures the general trend of the measured spall strength data in the present experiments as a function of the applied shear strain and the normal stress.

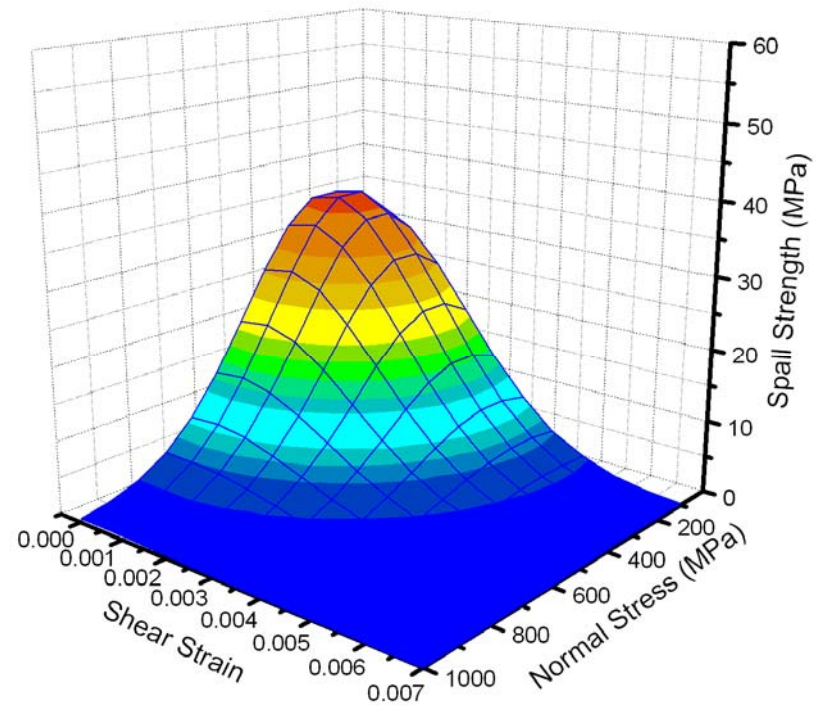


Figure 5.13: The dependence of shear and normal stress on spall strength is shown in this smoothed surface generated by equation(5.3).

5.6 Summary

A series of normal impact and pressure-shear plate experiments were conducted to study the spall strength of a S2-glass fiber reinforced polymer composite. The spall strength of GRP was found to decrease with increasing normal and shear stress. The effect of normal and shear stress on spall strength of GRP was illustrated as a three dimensional surface. The surface adequately describes the dependence of GRP's spall strength on the applied shear strain and the normal stress. More experiments at larger skew angles in pressure-shear plate impact experiments are recommended to refine the experimental results.

Reference

Dandekar, D. P., Boteler, J. M., Beaulieu, P. A., 1998. "Elastic Constants and Delamination Strength of a Glass-fiber reinforced Polymer Composite", Composites Science and Technology, 58, 1397-1403.

DeLuca E., Prifti J., Betheney W., Chou S. C., 1998. "Ballistic Impact Damage of S2 Glass Reinforced Plastic Structural Armor", Composites Science and Technology, 58, 1453-1461.

Fink B. K., 2000. "Performance Metrics for Composite Integral Armor", Journal of Thermoplastic Composite Materials, 13, 417-431.

Grady D.E., Kipp M.E., 1993. Dynamic Fracture and Fragmentation. In: High-Pressure Shock Compression of Solids, edited by: Asay J.R., Shahinpoor M., Springer-Verlag New York, 265-322.

Gray III G.T., 2000. Shock wave testing of ductile materials. ASM handbook, Mechanical Testing and Evaluation, 8, 10th ed., 530-559.

Zaretsky E., deBotton G., Perl M., 2004. "The Response of a Glass Fibers Reinforced Epoxy Composite to an Impact Loading", International Journal of Solids and Structures, 41, 569-584.

Chapter 6

SHEAR STRENGTH OF S2 GLASS FIBER REINFORCED POLYMER COMPOSITE UNDER SHOCK COMPRESSION

6.1 Introduction

For most materials, the yield strength is typically less than 1 GPa; when shock compressed to above 10 GPa, the stress normal to the shock front (which is an experimentally determined quantity) is often taken equal to the mean stress. This approximation is understood to be within experimental error in shock wave experiments. However, recent results of shock wave studies suggest this assumption may not be valid; the dynamic yield strength of a solid under shock compression is given by the difference between the dynamic compressibility curve obtained under uniaxial strain conditions, also referred to as the Hugoniot curve, and the hydrostat, which is either measured directly or determined by extrapolating the pressure volume behavior of the material determined at lower hydrostatic pressures. Based on von Mises yield criteria the difference between

the Hugoniot stress and the hydrostatic pressure curve is defined as two-thirds the dynamic yield strength. If this difference is (1) independent of the shock-loading stress then the material exhibits elastic-perfectly plastic behavior; (2) changing with increasing stress then the material exhibits a pressure-dependent yield strength. An increase in yield strength may be attributed to many factors such as rate-dependence and/or a pressure dependent yield behavior, while a decrease would be related to a softening behavior resulting from heterogeneous deformation process and or from damage resulting from shock compression. For an accurate application of this technique, the hydrostat has to be extremely well-defined, and therefore, has the potential for limited use at lower stresses. Alternately, a direct measurement of both longitudinal and transverse stress can be made. This technique has been used recently to determine the full stress state under shock compression in silicon carbide in excess of 20 GPa (Feng et al., 1997). This technique is exploratory and promising and may have limited applicability in the higher stress regimes.

Fowles (1961) determined the shear strength of annealed Al2024 when compressed to about 5 GPa by comparing the recorded shock impact stress with the predetermined hydrostat curve of annealed Al 2024. He successfully showed that at the same compression strain the stress normal to the shock front is larger than the hydrostatic pressure by an amount equal to its shear strength, i.e. two-thirds of the dynamic yield strength. But in Fowles' (1961) method, a predetermined hydrostat curve was required. Later, Asay *et al.* (1978) proposed a self-consistent technique for estimating the dynamic yield strength of a shock loaded material by utilizing shock-reshock and shock-release experimental data from a desired compression state. Asay and Chhabildas (1981) utilized this technique to study the variation of shear strength in Al 6061-T6 under shock compression stress ranging from about 8 GPa to 40 GPa. They found that the shear strength of Al 6061-T6 observed during shock compression increased with increasing shock stress.

In view of the importance of GRP in composite integral armor systems, in the present work, the aforementioned self-consistent technique described by Asay and Chabbildas (1981) is adopted to estimate the dynamic yield strength of GRP following shock compression. Using this procedure the shear strength of the shocked GRP was determined for impact stresses in the range of 1.0 to 2.0 GPa.

6.2 Self-Consistent Dynamic Yield Strength Determination Method

Plate impact experiments are often used to generate high-strain-rate uniaxial strain conditions in materials. For uniaxial strain in the x-direction, the state of stress during shock compression is given by

$$\tau = \frac{\sigma_x - \sigma_y}{2} = \frac{\sigma_x - \sigma_z}{2}, \quad (6.1)$$

where, τ is the resolved shear stress; σ_x represents the longitudinal stress; and σ_y and σ_z represent the lateral stresses in the specimen. In accordance to the von Mises yield criterion, if the stress state is on the yield surface, the shear stress attains its maximum value, τ_c , which is the shear strength. Since in plate impact experiments, under uniaxial strain conditions, the lateral stresses $\sigma_y = \sigma_z$, the mean stress in the shocked state can be expressed as

$$\bar{\sigma} = \frac{1}{3}(\sigma_x + 2\sigma_y). \quad (6.2)$$

From Equations (6.1) and (6.2), the longitudinal stress σ_x and the lateral stress

σ_y can be expressed in terms of the mean stress and the shear stress as

$$\sigma_x = \bar{\sigma} + \frac{4}{3}\tau, \quad (6.3)$$

$$\sigma_y = \bar{\sigma} - \frac{2}{3}\tau. \quad (6.4)$$

In most typical normal plate-impact gas gun experiments only the longitudinal stress is measured, and so it is necessary to infer the shear stress and/or material strength indirectly. For estimating the shear stress in the shocked state, it is often assumed that the mean stress can be approximated from low pressure quasi-static measurements. This procedure is not accurate at high pressures due to uncertainties in extrapolating low pressure response and also because thermal effects must be explicitly accounted for when estimating hydrostatic response. Conversely, if Hugoniot data are used to estimate the mean stress, $\bar{\sigma}$, the influence of a finite shear strength contribution to the Hugoniot requires evaluation.

A more direct approach is to estimate shear stress in the shocked state. Taking the derivative of Equation (6.3) with respect to engineering strain, ε , yields

$$\frac{d\sigma_x}{d\varepsilon} = \frac{d\bar{\sigma}}{d\varepsilon} + \frac{4}{3} \frac{d\tau}{d\varepsilon}. \quad (6.5)$$

As will be shown later in this section, the relation allows for the determination of the shear stress from shock wave measurement without recourse to other data.

Figure 6.1 illustrates graphically the response expected if a material is shocked to an initial longitudinal stress, σ_H . Initial yielding is assumed to occur at the Hugoniot Elastic Limit, HEL, and steady shock compression proceeds along the Rayleigh line to a point on the solid Hugoniot. At the Hugoniot stress σ_H , there is a deviatoric stress offset of $\frac{4}{3}\tau_H$ from the mean stress. In the idealized elastic-plastic theory, τ_H is equal to the maximum shear strength τ_C . However, due to possible transient softening effects during the initial compression process or to time-dependent hardening effects in the shocked state, the shear stress in the shocked state, τ_H , may differ from the maximum stress, τ_C , the material can support.

In view of Equation (6.3) the relation between the Hugoniot stress σ_H , mean pressure $\bar{\sigma}$, and shear stress τ_H is given by

$$\tau_H = \frac{3}{4}(\sigma_H - \bar{\sigma}). \quad (6.6)$$

Equation (6.6) yields the following relations

$$\sigma_H = \bar{\sigma} + \frac{4}{3}\tau_H \quad (6.7)$$

$$\sigma_{\max} = \bar{\sigma} + \frac{4}{3}\tau_c \quad (6.8)$$

$$\sigma_{\min} = \bar{\sigma} - \frac{4}{3}\tau_c \quad (6.9)$$

In Equations (6.8) and (6.9) σ_{\max} and σ_{\min} are the maximum and the minimum stresses at the common Hugoniot strain ε_H , and are estimated along with the shear-stress in the shocked state τ_H , and the shear strength, τ_c , by employing a combination of shock-release and shock-reshock experiments from approximately the same “First Hugoniot Shocked State.” If the material is released from the initial Hugoniot Shocked State σ_H , Equation (6.3) should apply continuously as the shear stress varies from its initial value τ_H , to a final value, $-\tau_c$, corresponding to reverse yielding. For the sake of discussion, reverse yielding is

assumed to occur at State 2 along the unloading path. Similarly, during reshocking from σ_H , the shear stress increases from its initial value $\tau_H < \tau_c$, to the shear strength.

Combining Equations (6.7) to (6.9), the following equations can be obtained

$$\tau_c + \tau_H = \frac{3}{4}(\sigma_H - \sigma_{\min}) \quad (6.10)$$

$$\tau_c - \tau_H = \frac{3}{4}(\sigma_{\max} - \sigma_h) \quad (6.11)$$

where the critical stress Y_C is defined as

$$Y_C = 2\tau_c = \frac{3}{4}(\sigma_{\max} - \sigma_{\min}). \quad (6.12)$$

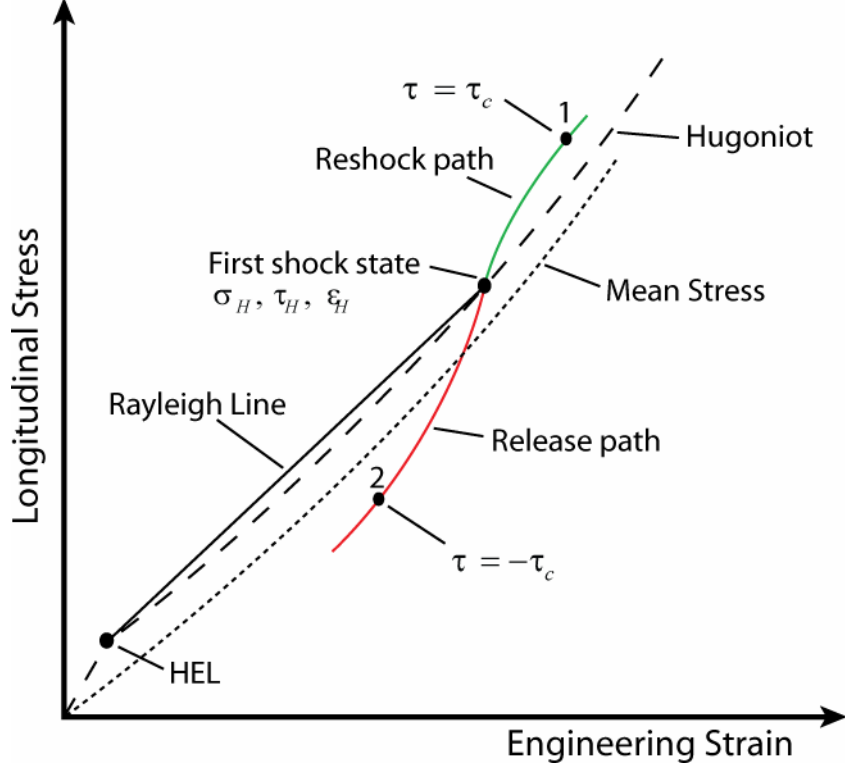


Figure 6.1: Stress vs. Strain states for a pair of reshock/release experiments loading or unloading from the same Hugoniot state.

Equation (6.5) is amenable to stress profile measurements which allow determination of wave velocities associated with a given increment of stress or strain. The Lagrangian velocity C_L , at any point in the profile, assuming rate-independent response, is related to the stress derivative by

$$\frac{d\sigma_x}{d\varepsilon} = \rho_0 C_L^2, \quad (6.13)$$

where ρ_0 represents the initial density.

Moreover, Lagrangian bulk velocity, C_B , can be defined as

$$\frac{d\bar{\sigma}}{d\varepsilon} = \rho_0 C_B^2. \quad (6.14)$$

Using Equations (6.13) and (6.14) in (6.5), yields

$$\frac{d\tau}{d\varepsilon} = \frac{3}{4} \rho_0 (C_L^2 - C_B^2). \quad (6.15)$$

By integrating Equation (6.15), the increment and decrease of shear stress to

States 1 and 2 following the reshock and release paths can be determined.

The increment in shear stress along the reshock path is given by

$$\tau_c - \tau_H = \frac{3}{4} (\sigma_{\max} - \sigma_H) = \frac{3}{4} \rho_0 \int_{\varepsilon_H}^{\varepsilon_1} (C_L^2 - C_B^2) d\varepsilon, \quad (6.16)$$

while the decrease in shear stress along the release path is given by

$$\tau_c + \tau_H = \frac{3}{4} (\sigma_H - \sigma_{\min}) = \frac{3}{4} \rho_0 \int_{\varepsilon_H}^{\varepsilon_2} (C_B^2 - C_L^2) d\varepsilon \quad (6.17)$$

In Equations (6.16) and (6.17)

τ_H = Hugoniot shear stress at first *Hugoniot* shock state, τ_c = shear strength,

ε_H = Hugoniot strain at first *Hugoniot* shock state,

ε_1 = strain at maximum shear stress state, ε_2 = strain at minimum shear stress state

The critical material strength, Y_C , can be deduced from (6.16) and (6.17) as

$$Y_c = 2\tau_c = \frac{3}{4}(\sigma_{\max} - \sigma_{\min}) = \frac{3}{4}\rho_0 \left[\int_{\varepsilon_0}^{\varepsilon_2} (C_L^2 - C_B^2) d\varepsilon - \int_{\varepsilon_0}^{\varepsilon_1} (C_L^2 - C_B^2) d\varepsilon \right] \quad (6.18)$$

6.3 Brief Description of the Experimental Configuration

The plate impact experiments conducted in the present study utilized an 82.5 mm smooth bore single stage gas gun facility in the D. K. Wright Laboratory at the Case Western Reserve University. An illustration of the experiment setup is shown in

Figure 6.2. In order to conduct these experiments a dual flyer plate assembly was utilized. The shock-resock experiments were conducted by using a projectile faced with GRP and backed with a relatively high shock impedance Al 6061-T6 plate; for the shock-release experiments the GRP was backed by a relatively lower impedance PMMA backup flyer plate. The target configuration in

Figure 6.2 will have a GRP disk similar to that mounted on the projectile and a PMMA window bonded with epoxy to the back of the GRP sample to prevent spall during the impact process. The PMMA is an optical quality disk, lapped and polished and is typically flat to within a few bands of sodium light. One surface of the PMMA is diffused and approximately 100 nm of aluminum is vapor

deposited on the lapped surface before being glued to the GRP disk. The in-material particle velocity history resulting from impact was measured at the GRP/PMMA window interface using a velocity interferometer, VALYNTM VISAR system (Barker and Hollenbach, 1972).

The details of the thicknesses of the front flyer plates, the flyer backing plates, the GRP target plates and the PMMA window are provided in Table 6.1. In all experiments square GRP target plates and square PMMA window plates with dimensions of 54 mm x 54 mm, were employed. The Al 6061-T6 flyer backup plate were 3 inch diameter disks. The adhesives used to bond each flyer/backing plate and target/window assembling were Tra-ConTM TRA-BOND 2115, which is a clear, low viscosity, low cure shrinkage epoxy.

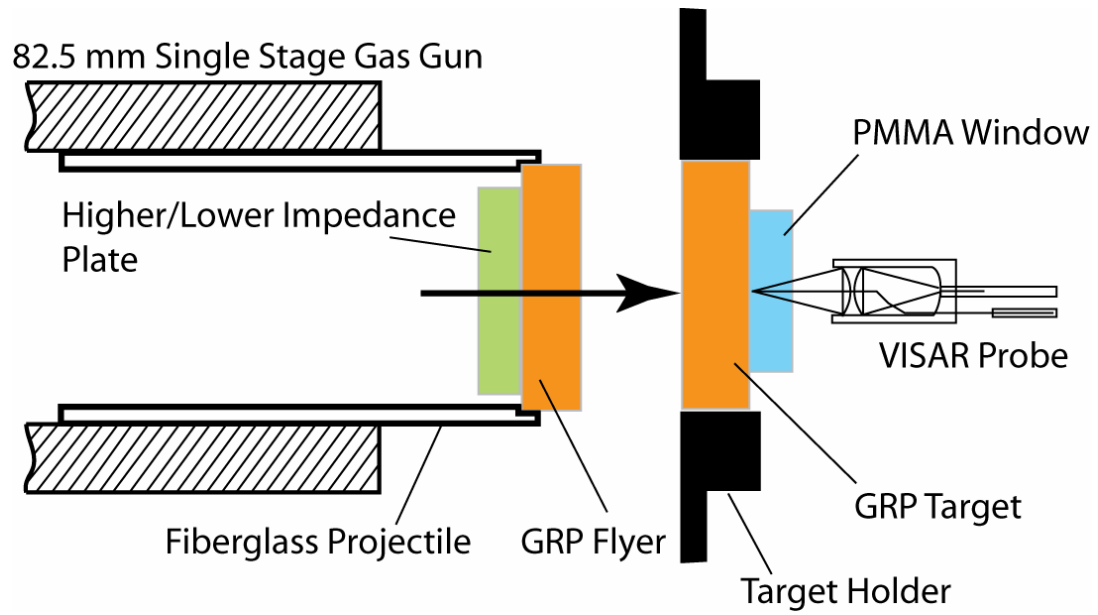


Figure 6.2: Experiment setup for shock-resock and shock-release experiments.

Exp No.	Flyer	Flyer thickness (mm)	Backing plate	Backing plate thickness (mm)	Target	Target thickness (mm)	PMMA Window thickness (mm)
LT 71	GRP	4.45	PMMA	12.13	GRP	9.53	12.35
LT 73	GRP	4.50	Al 6061-T6	12.08	GRP	9.67	12.37
LT 76	GRP	4.25	PMMA	12.05	GRP	9.43	12.28
LT 77	GRP	4.33	Al 6061-T6	12.16	GRP	10.35	12.53

Table 6.1: Plate arrangement and thicknesses in resock/release experiments.

6.4 t-X (Time vs. Distance) diagram & S-V diagram (Stress vs. Velocity)

6.4.1 Shock-Reshock Experiments

The experimental configuration for producing the shock-reshock loading in this study is illustrated in Figure 6.3 and Figure 6.4 in the t-X and the stress-particle velocity diagrams, respectively. Experimentally this is implemented using the projectile configuration shown in Figure 6.2. The initial shock in the impactor reflects from the GRP/Al6061-T6 interface as an loading (reshock) from material States 3 to 4, as shown in Figure 6.3, and will propagate towards the GRP/PMMA window interface resulting in State 5. As indicated in the t-X diagram, the GRP is shock loaded to State 3, re-shocked to State 4, which is recorded as State 5 and 7 at the GRP/PMMA window interface. In these experiments, the shock impedance of Al 6061-T6 determines the final shocked state of the GRP.

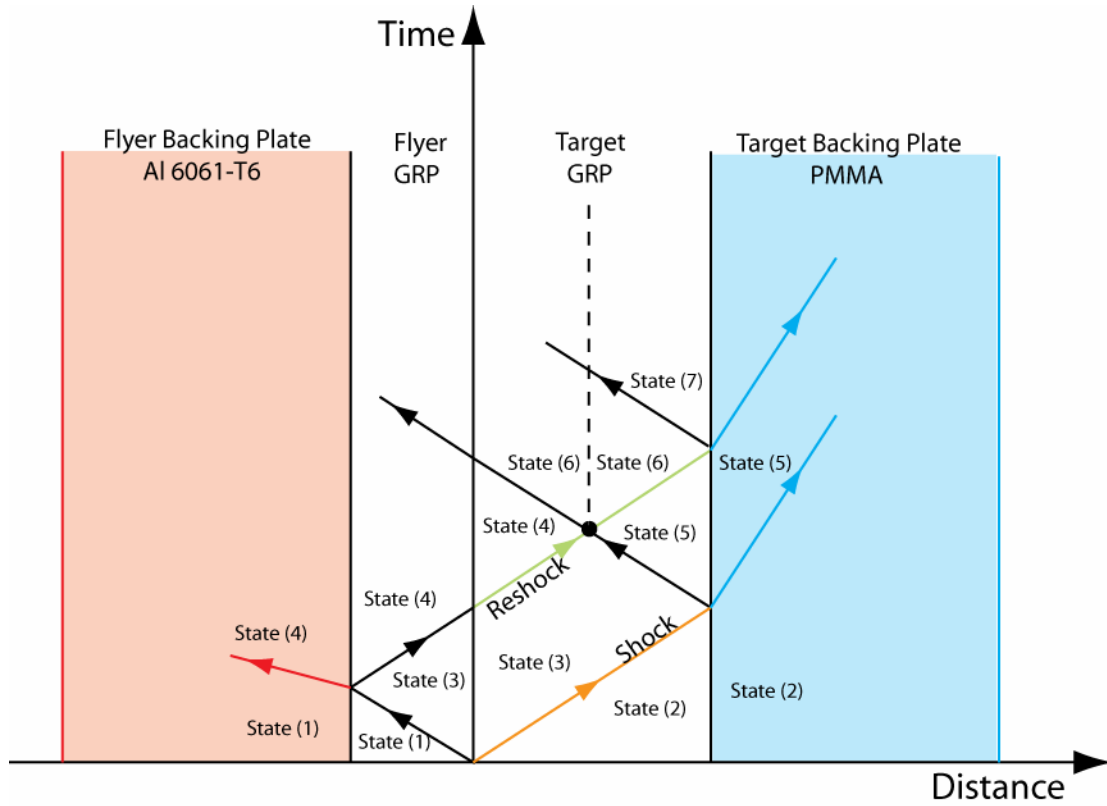


Figure 6.3: Time-Distance diagram for shock-res shock experiments.

Figure 6.4 shows the stress-particle velocity diagram for shock-res shock experiments. The abscissa represents the particle velocity for the shock states while the ordinate represents the normal stress for the shock states. The shock states 1 to 7 corresponds to the shock states presented in Figure 6.3. In the figure, the slopes of the S-V curves for the various materials are proportional to their shock impedance, given in

Table 6.2. The important shock states are States 5, 6, and 7. To avoid spall during the shock wave propagation, State 6 has to be under compressive stress; this condition is satisfied here for all impact velocities used in the present series of experiments. States 5 and 7 represent the particle velocity and the stress states at the free surface during the experiments. The desired particle velocity for State 3 was later calculated from the measured free surface particle velocity in State 5. After the re-shock wave arrives at free surface of the target plate (State 7), the stress and particle velocity increases to a higher level; the particle velocity is about 46% higher than the particle velocity in State 5. The particle velocities in State 5 and State 7 can be found in terms of the impact velocity u_1 , as

$$u_5 = \frac{Z_{GRP}}{Z_{GRP} + Z_{PMMA}} u_1 = 0.661 u_1, \quad (6.19)$$

where Z_{GRP} is the shock impedance for the GRP, and Z_{PMMA} is the shock impedance for PMMA.

Moreover,

$$u_7 = \frac{2Z_{GRP}Z_{Al}}{(Z_{GRP} + Z_{Al})(Z_{GRP} + Z_{PMMA})} u_1 = 0.967 u_1, \quad (6.20)$$

where, Z_{Al} is the shock impedance of Al6061-T6.

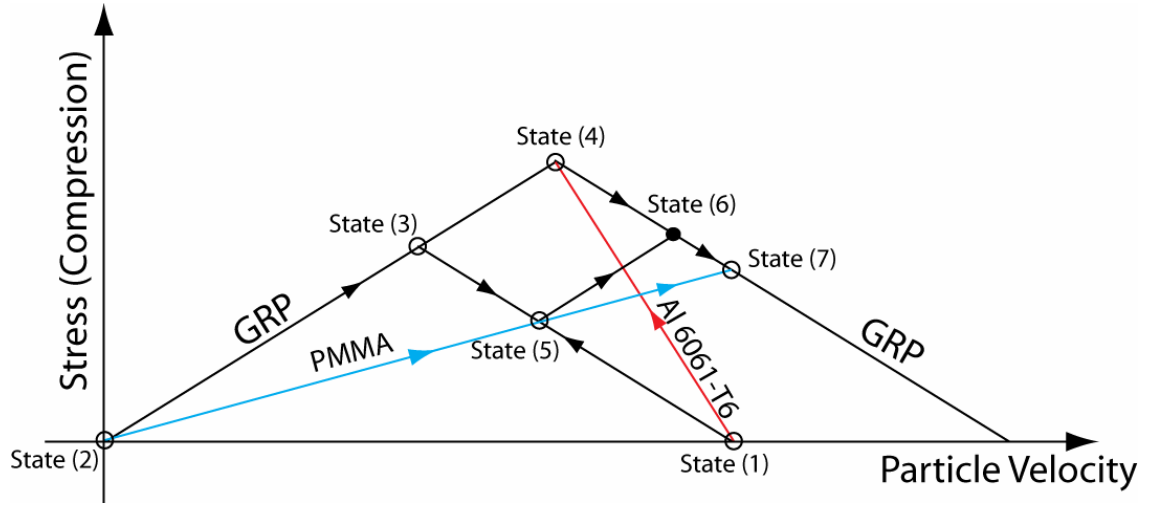


Figure 6.4: Stress-particle velocity diagram for shock-res shock experiments.

Based on the flyer and the target materials and their wave speeds given in

Table 6.2, the optimized thickness of the flyer, backing, target and window plates

were determined. The target thickness was determined to ensure that the

experiments would have the longest window time possible. To achieve this, the

time for shock wave to traverse three times in the target was set equal to the

time when boundary waves arrive at the monitoring point, i.e.

$$\frac{3h_T}{u_{GRP}} = \frac{\sqrt{h_T^2 + (l_T / 2)^2}}{u_{GRP}}. \quad (6.21)$$

In Equation (6.21) h_t represents target thickness; u_{GRP} represents the wave speed in the GRP; and l_t represents the target thickness. This resulted in a target thickness of 9.546 mm. The window time corresponding to this target thickness was 6 μs .

The flyer thickness was determined such that the first shock-wave and the re-shock/release waves have sufficient time to reach an equilibrium level (the rise time in GRP varied between 0.8 ~ 2 μs , depending on the shock stress level and the porosity of the tested GRP plates). In view of this, the flyer thickness was designed such that the reshock/release waves arrived 3 μs after the arrival of the first shock wave, which is about 4.5 mm in thickness. Moreover, the thickness of the Al 6061-T6 plate and PMMA window was kept large enough such that the wave reflections from the free surfaces of these plates do not interfere with the wave propagation in the target during the window time. In view of these constraints, the thickness of the Al 6061-T6 plate is chosen to be 12 mm and the thickness of PMMA window was chosen to be 12 mm as well. The GRP flyer and

the target plates were machined from 20 mm thick GRP plates to their desired thickness. All the impact surfaces were lapped to be within 1 micron flatness.

Material	Longitudinal wave velocity (km/s)	Density (g/cc)	Acoustic Impedance ($\text{Ggm}^{-2}\text{s}^{-1}$)	References
GRP	3.2	1.949	6.237	(Dandekar et. al, 2003a)
PMMA (polymethyl methacrylate)	2.69	1.191	3.204	(Kutz, 2002) Index of refraction: 1.4915 (Swalen, 1996)
Al 6061-T6	6.31	2.7	17.037	(Kutz, 2002)

Table 6.2: Wave speed, density and impedance of materials used in reshock/release experiments.

6.4.2 Shock-Release Experiments

The t-X diagram for the shock-release experiments on GRP materials is shown in Figure 6.5. The abscissa represents the distance from the impact surface; the positive direction represents the distance into the target assembly and the negative direction represents the distance into the flyer assembly. The ordinate indicates the time after impact. The PMMA backing plate material is the same as the PMMA window material and the thickness of the PMMA backing plate is 12 mm. The initial shock in the GRP impactor (flyer) reflects from the GRP/PMMA interface as an unloading (release) from material States 3 to 4, as shown in Figure 6.5, and will propagate towards the GRP/PMMA window interface resulting in State 5. As indicated in the t-X diagram, the GRP is shock loaded to State 3, released to State 4, which is recorded as State 5 and 7 at the GRP/PMMA window interface. In these experiments, the shock impedance of PMMA determines the final released state of the GRP.

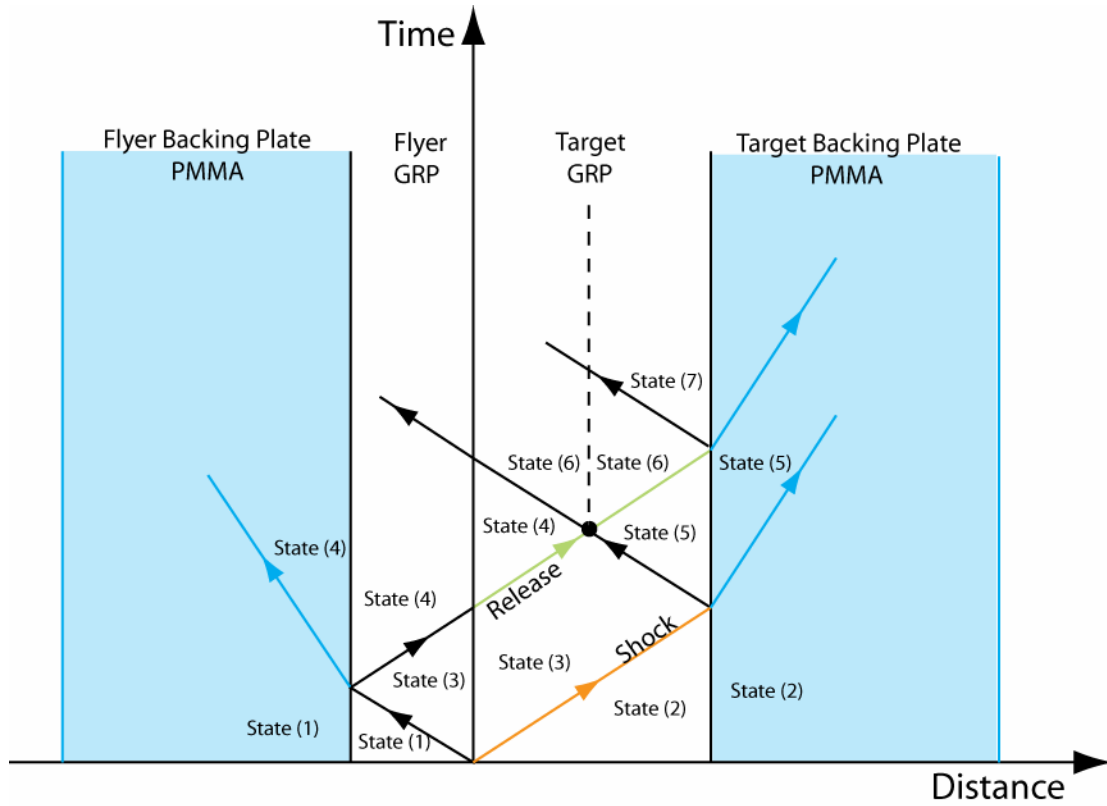


Figure 6.5: Time-Distance diagram for shock-release experiments.

Figure 6.6 shows the S-V diagram for shock-release experiments. The abscissa represents the particle velocity while the ordinate represents the normal stress in the shocked state. The States 1 to 7 correspond to the shock states shown in Figure 6.5. The important shock states are States 5, 6, and 7. In order to avoid spall, State 6 has to be under compressive stress, a condition that is satisfied in the present experiments. States 5 and 7 are states measured at the rear surface of

the target during the experiments. Since the GRP target plate is backed by a PMMA window in both the shock-release and shock-reload experimental configurations, the stress and particle velocity in State 5 at the same impact velocity is the same in the two configurations. In the shock-release experiments the stress and particle velocity in State 7 traverses to a lower level than state 5 (about 68% of State 5). The velocity for State 5 and State 7 can be related to the impact velocity u_1 , as

$$u_7 = \frac{2Z_{PMMA}}{(Z_{GRP} + Z_{PMMA})} u_5 = 0.448u_1 \quad (6.22)$$

where, u_5 is given by Equation (6.19).

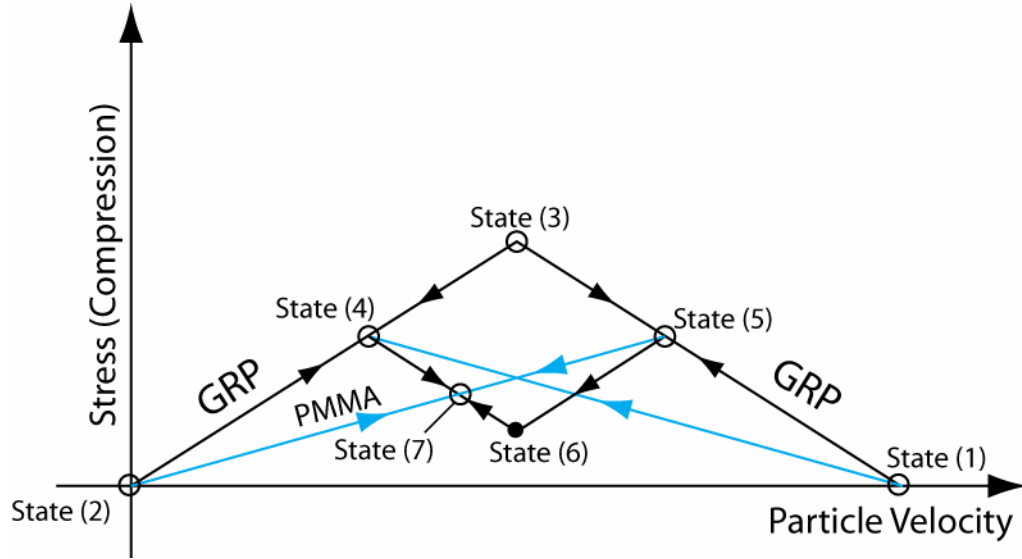


Figure 6.6: Stress versus Particle Velocity diagram for shock-release experiments.

6.5 Experimental Results and Discussion

Two sets of shock reshock and shock release experiments on GRP were conducted.

The shock-release experiment LT71, and the shock-reshock experiment LT73, were conducted at impact velocities of 252 m/s and 264 m/s, respectively. The shock-release experiment LT76 and the shock-reshock experiment LT77 were performed at relatively higher impact speeds of 498 m/s and 485 m/s, respectively.

Figure 6.7 shows the particle velocity versus time profiles for experiments LT71 and LT73. The abscissa represents the time after the arrival of the shock wave at the free surface of the monitoring plate while the ordinate represents the measured rear-surface particle velocity recorded by the VISAR system. The dashed lines indicate the elastic prediction of the “First Hugoniot shocked state” and the reshock/release particle velocity levels calculated using Equations (6.19), (6.20), and (6.22). The arrival times of reshock and release waves do not exactly coincide due to the differences in the flyer thickness. The rise-time associated with the reshock waves as well as the fall-time associated with the release wave is

much larger when compared to the rise of the first shock wave. Also, the oscillatory structure of the first shock Hugoniot state in the GRP is much less prominent in the reshock and release wave profiles. The details of the shock wave parameters obtained from these experiments are provided in

Table 6.3.

Figure 6.8 shows the particle velocity versus time profiles for Experiments LT76 and LT77. The abscissa represents the time after shock wave arrived and the ordinate represents the free surface particle velocity. Detailed shock wave parameters are presented in

Table 6.4. The dashed lines indicate the elastic prediction of the “First Hugoniot shock state” along with the calculated reshock and release particle velocity levels.

Again, because of the slight difference in the flyer thicknesses, the arrival times of the reshock and release waves do not coincide. Also, unlike in experiments LT71 and LT73, the rise-time and the fall-times associated with the reshock as well as the release waves show small changes in slope compared with the rise time

associated with the first shock wave. Moreover, the oscillatory characteristics of the first shock Hugoniot state in the GRP was not as prominent as that observed in experiments LT71 and LT73. The final release states in experiments LT71 and LT76 had good agreement with the elastic prediction but the final reshock states in experiments LT73 and LT77 were both below the elastic predictions.

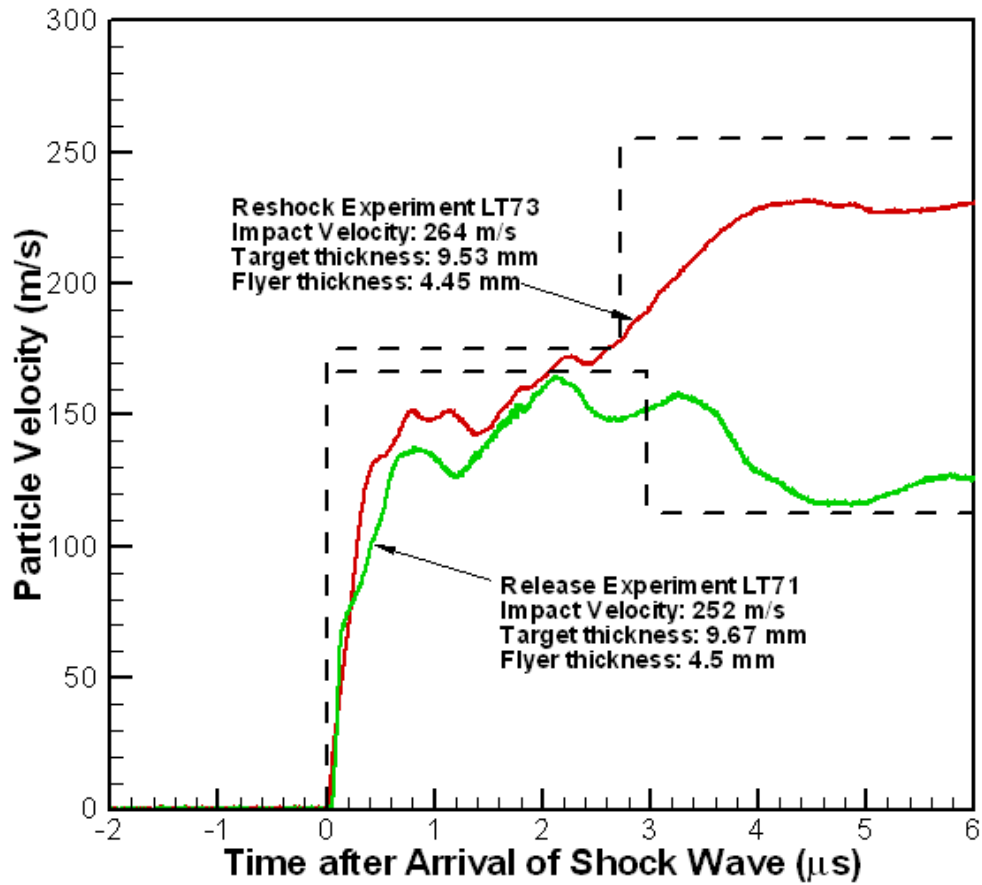


Figure 6.7: Free surface velocity-Time profile for experiments LT71 and LT73.

Exp No.	LT 71	LT 73
Impact Velocity (m/s)	252	264
Shock Wave arrival time (μs)	2.944	2.883
Rise time for first shock state (μs)	0.679	0.728
Averaged equilibrium first shock free surface velocity (m/s)	150	156.6
Arrival time of reshock/release waves (μs)	6.129	5.259
Rise/release time for reshock/release waves (μs)	1.178	1.619
Averaged final state free surface velocity (m/s)	119	230
Calculated Reshock/Unload Wave Velocity (km/s)	Unload wave speed: 2.01	Reshock Wave speed: 2.52

Table 6.3: Shock wave parameters for experiments LT71 and LT73.

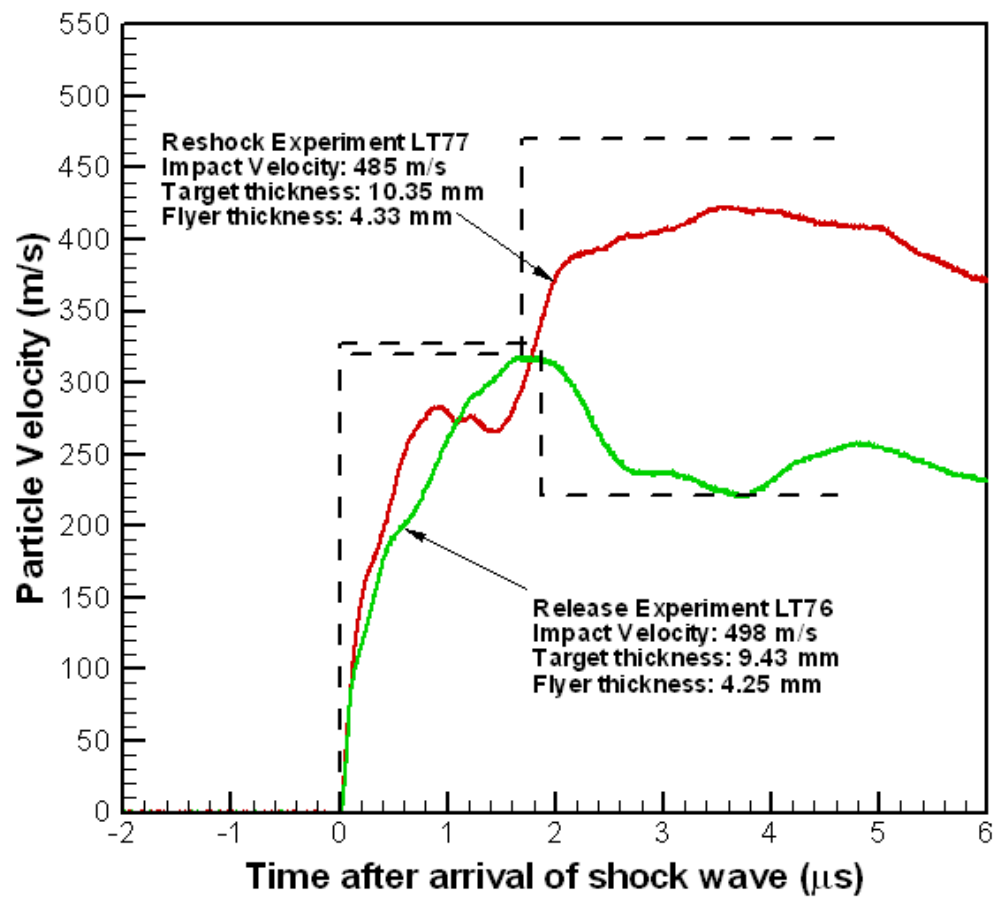


Figure 6.8: Free surface velocity-Time profile for experiments LT76 and LT77.

Exp No.	LT 76	LT 77
Impact Velocity (m/s)	498	485
Shock Wave arrival time (μs)	3.033	2.736
Rise time for first shock state (μs)	1.235	0.777
Averaged equilibrium first shock free surface velocity (m/s)	316	283
Arrival time of reshock/release waves (μs)	4.783	4.142
Rise/release time for reshock/release waves (μs)	0.654	1.014
Averaged final state free surface velocity (m/s)	236	415
Calculated Reshock/Unload Wave speed: (km/s)	Unload Wave speed: 2.68	Reshock Wave speed: 3.74

Table 6.4: Shock wave parameters for experiment LT 76 and LT 77.

6.6 Results and Discussion

6.6.1 Calculation of Hugoniot Stress versus Hugoniot Strain Curves Corresponding to the Off-Hugoniot States

An approach that employs the incremental form for stress and strain, both related to the corresponding Lagrangian velocity, was used for calculating the Hugoniot stress and strain paths corresponding to the off-Hugoniot states

$$\begin{aligned}\sigma &= \sum \rho_0 C_L \Delta u_p \\ \varepsilon &= \sum \frac{\Delta u_p}{C_L}\end{aligned}\tag{6.23}$$

In Equation (6.23) ρ_0 is the initial material density; u_p is the particle velocity; and C_L is the Lagrangian wave speed.

The particle velocity u_p was calculated from the measured free surface velocity by using the relation

$$u_p = \frac{u_{fs}}{2} \frac{(Z_{PMMA} + Z_{GRP})}{Z_{GRP}},\tag{6.24}$$

where, u_{fs} is the free surface particle velocity, Z_{PMMA} is the shock impedance for the PMMA window, and Z_{GRP} is the shock impedance for the GRP.

Equation (6.24) was derived from the S-V diagram for the shock-res shock and shock-release experiments, i.e Figure 6.4 and Figure 6.6, respectively.

The Lagrangian velocity C_L was calculated using

$$C_L(u_{fs}) = \frac{\delta_T}{\left[T + \Delta t(u_{fs}) - 2\delta_F / U_{eff} \right]}. \quad (6.25)$$

In Equation (6.25), T is the arrival time of the shock front at the rear surface of the GRP target; δ_T and δ_F are the GRP target and the flyer thickness, respectively; and U_{eff} is the effective shock wave speed.

The effective shock velocity U_{eff} was introduced by Reinhart and Chhabildas (2003) to take into account the finite rise-time of the shock in the flyer as a single shock wave traversing at an effective shock velocity. It is calculated by using the relation

$$U_{eff} = \frac{\sigma_H}{\rho_0 u_H} \quad (6.26)$$

In (6.26) σ_H and u_H represent the stress and particle velocity of the first shock state, respectively.

The off-Hugoniot stress vs. strain curves for experiments LT71, LT73, LT76, and LT77 from the “First Hugoniot Shocked State” are presented in Figure 6.9. The abscissa represents the engineering strain and the ordinate represents the normal stress along impact direction. The squares indicate the Hugoniot states of GRP calculated from the experiments described in Chapter 4, and the triangle represents the shock Hugoniot states of GRP from Dandekar *et al.* (2003a). The four circles represent the Hugoniot states of the reshock/release experiments. These Hugoniot states were calculated from the following equations:

$$\begin{aligned}\varepsilon_H &= \frac{u_H}{U_s} \\ \sigma_H &= \rho_0 U_s u_H\end{aligned}\tag{6.27}$$

The calculated Hugoniot curve (dashed orange line) utilized the relationship between Hugoniot stress and strain derived from EOS:

$$\sigma_H = \frac{\rho_0 C_0^2 \varepsilon_H}{(1 - S \varepsilon_H)^2}\tag{6.28}$$

For higher impact stress experiments, LT76 and LT77, the path of the off-Hugoniot states was observed to deviate much more from the calculated Hugoniot curve when compared with the lower impact velocity experiments, LT71 and

LT73. Some previous reshock/release tests on Alumina (Asay and Chhabildas, 1981; Reinhart and Chhabildas, 2003) and Silicon Carbide (Dandekar *et al.*, 2003b) showed elastic reshock as well as elastic release at the leading edge of the reshock/release waves. But there is no indication of elastic precursor in the reshock waves or elastic release in the release waves at the leading front when reshock/release waves arrived in GRP materials. The states “1” and “2” in Figure 6.9 were chosen from the time when the reshock and release waves intersect with the $\pm\tau_c$ dashed Hugoniot lines. The Hugoniot states of the reshock/release experiments matched pretty well with the calculated Hugoniot curve and the critical strength can be calculated graphically (Reinhart and Chhabildas, 2003). The summary of the Hugoniot stress, Hugoniot strain, and the residual strength are shown in

Table 6.5.

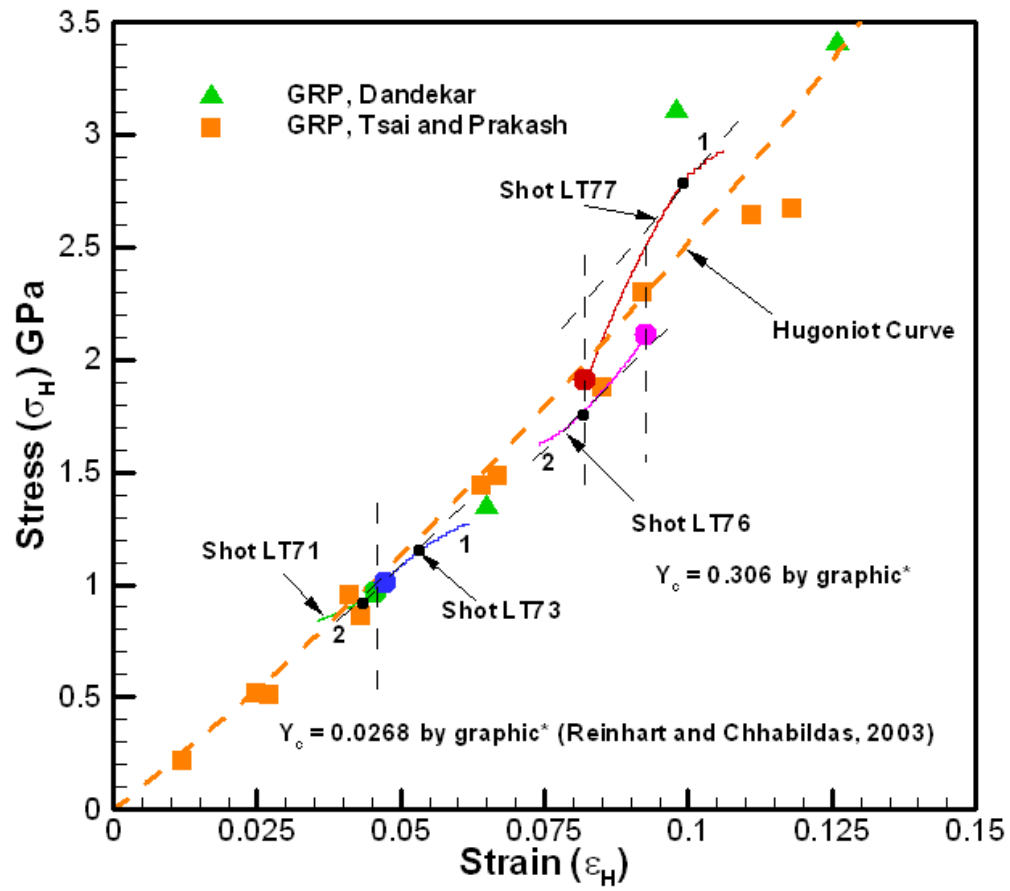


Figure 6.9: Stress vs. Strain curves for experiment LT71, LT73, LT76, and LT77.

Exp No.	Hugoniot velocity (m/s)	Hugoniot stress (GPa)	Hugoniot strain	Critical strength (GPa)
LT 71	107.5	0.965	0.0457	0.0268
LT 73	112	1.014	0.0474	
LT 76	223.8	2.112	0.0926	0.306
LT 77	199.8	1.911	0.0821	

Table 6.5: Summary of Hugoniot states and critical strength for experiment LT71, LT73, LT76, and LT77.

6.7 Summary

Plate impact shock-resock and shock-release experiments were conducted on GRP materials to estimate the shear strength of the material. There is no indication of elastic behavior in the reshock waves and the release waves. The rise time in the reshock waves and decent time in the release waves decreased with increasing impact stress. The critical strength increased dramatically from 0.0268 GPa to 0.306 GPa between the two pairs of experiments. The strain hardening in the tested stress range was quite obvious but further shock-resock and shock-release experiments at higher stress range were necessary to fully understand the strain hardening behavior of GRP at higher stresses.

REFERENCE

Asay J. R. and Chhabildas L. C., 1981. 'Determination of the Shear Strength of Shock Compressed 6061-T6 Aluminum', Shock Waves and High-Strain-Rate Phenomena in Metals, eds. Myers, M.M. and Murr, L. E. Plenum Pub. Corp, New York, NY, 417-431.

Asay J. R. and Lipkin J., 1978. "A self-consistent Technique for Estimating the Dynamic Yield Strength of a Shock-loaded Material," Journal of Applied Physics, 49, 4242-4247.

Barker L. M., Hollenbach R. E., 1972. 'Laser Interferometer for Measuring High Velocities of Any Reflecting Surface', Journal of Applied Physics, 43, 4669-4675.

Dandekar D. P., Hall C. A., Chhabildas L. C., Reinhart W. D., 2003a. 'Shock Response of a Glass-Fiber-Reinforced Polymer Composite', Composite Structures, 61, 51-59.

Dandekar D. P., Reinhart W. D., Chhabildas L. C., 2003b. 'Reshock Behavior of Silicon Carbide', Journal of Physics IV France, 110, 827-831.

Fowles G. R., 1961. "Shock Wave Compression of Hardened Annealed 2024 aluminum," Journal of Applied Physics, 32, 1475-1487.

Kutz M., 2002. Handbook of Materials Selection, John Wiley & Sons, 694-698.

Reinhart W. D., Chhabildas L. C., 2003. 'Strength Properties of Coors AD995 Alumina in the Shocked State', International Journal of Impact Engineering, 29, 601-619.

Swalen J. D., 1996. 'Linear Optical Properties of NLO Polymers', Pure and Applied Optics, 5, 723-729.

Zaretsky E., deBotton G., Perl M., 2004. 'The Response of a Glass Fibers Reinforced Epoxy Composite to an Impact Loading', International Journal of Solids and Structures, 41, 569-548.

Chapter 7

CONCLUSIONS

Shock-wave propagation in heterogeneous material systems is a complex phenomenon, and GRP's dynamic shock response is affected by scattering, dispersion and attenuation of shock waves. These material nonlinearities can be attributed to a number of material and geometrical heterogeneities including material impedance mismatch, geometry of the fiber reinforcement, elastic-plastic material behavior, material failure and delamination. In the present study, in order to understand the shock response of the GRP, an integrated experimental and analytical approach is carried out to study the structure of shock waves in layered material structures. Asymptotic techniques were applied to analyze propagation of acceleration waves in 2-D layered material systems. The analysis makes use of the Laplace transform and Floquet theory for ODE with periodic coefficients. Both wave-front and late-time solutions for step-pulse loading on layered half-space are presented for several elastic/elastic and elastic/visco-elastic bilaminates. From these studies a two-wave shock structure is predicted -- a leading elastic precursor wave

followed by late-time oscillatory wave in the Shocked Hugoniot state. By changing the material properties and layer thicknesses in elastic/elastic and elastic/visco-elastic bilaminates, the effect of layer density, material impedance mismatch, and material inelasticity on the attenuation and dispersion of shock waves through layered materials was systematically studied. The elastic precursor was found to decay with increasing layer density, material impedance mismatch, and propagation distance while the late-time oscillation frequency was found to decrease with impedance mismatch and increase with layer density. Also, the material inelasticity was found to dramatically decrease the late-time oscillation frequency and the amplitude of the elastic precursor.

To verify the analytical results, normal plate-impact experiments are conducted on layered material targets to understand the role of material architecture and material inelasticity in governing the elastic precursor decay and late-time wave dispersion. In this study, iron/titanium and aluminum/polycarbonate bilaminates were carefully prepared and shock compressed to 0.8 to 1.9 GPa. The observed elastic precursor decay and late-time wave oscillation profile showed good agreements with the asymptotic solutions.

A series of plate impact experiments were conducted on GRP specimens to study its dynamic response under shock stresses ranging from 0.04 to 2.6 GPa. Unlike the elastic-elastic bilaminates, no elastic precursor was observed in the GRP, and the late-time oscillations were not as distinct as in bilaminates. Because the inelasticity of polymer matrix and the geometry of the glass weave, the elastic precursor was not observed in the measured free surface particle velocity profiles; moreover, the late time oscillations were weaker than expected. However, by increasing the shock compression, the rise-time of the shock front and the amplitude of late time oscillations decreased. The critical amplitude for GRP, which represents the specific shock stress for a clear shock-front to appear during shock loading, was observed to be between 1.5 to 2.0 GPa. The effect of propagation distance on the attenuation of the shock waves in GRP was also studied by changing the thickness of GRP specimens. Four different thickness GRP specimens, 3mm, 7mm, 13.5mm, and 20mm, were shock loaded to similar stress level around 0.85 GPa. The experiments were designed so that the hydrodynamic decay would not occur during the experiments. Under these conditions only limited shock wave attenuation with distance of shock wave propagation was observed in the tested thickness range.

Although shock waves propagation in GRP was somewhat irregular, some important material shock parameters were determined through careful data analysis. Equation of State (EOS) is essential to describe the shock response of materials and can only be determined experimentally. Combining the results of the present experiments with data from Dandekar *et al.* (2003) and Hall *et al.* (2003), EOS of GRP was determined between 0.04 GPa to 20 GPa. Besides EOS, the Hugoniot curve (Hugoniot stress vs. Hugoniot strain) was calculated using Rankine-Hugoniot relationships; the departure of the Hugoniot stress vs. particle velocity curve from linearity allowed the estimation of the Hugoniot Elastic Limit (HEL) of the GRP to be about 1.6 GPa.

The GRP is chosen to be one of the core materials in composite integral armors because of its excellent strength along the glass fiber reinforcement directions; however, the interfacial strength between the glass layers and the resin matrix is quite weak, and spall usually occurs during a typical impact process. Spallation is the failure of material due to the action of tensile stresses developed in the interior of a material and usually determines the integrity of composite materials. Plate impact experiments were employed to study the spall strength of GRP. Normal plate impact, and combined pressure and shear experiments with skew

angles ranging from 12° to 20° , were performed to study the effects of both normal compression and combined compression and shear on the GRP's spall strength. The GRP specimens were shock loaded to around 1.0 GPa and the skew angle of impact resulted in a maximum shear strain of 0.615% during the combined pressure and shear loading. A 3-dimensional failure surface, as a function of the applied shear-strain and the normal-stress, was constructed to illustrate the results of spall strength experiments. The spall strength of GRP was always less than 0.05GPa, and was observed to decrease with increasing tensile and shear stress.

In addition to the shock compression and spall experiments, several plate-impact shock/reshock and shock/release experiments were conducted on the GRP at a Hugoniot stress of 1.0 to 2.0 GPa. The objective of these shock/reshock and shock/release experiments was to determine the dynamic yield strength of GRP under shock compression, using the self-consistent technique proposed by Asay *et al.* (1978). The rise-time in the reshock waves and the release waves was found to decrease with increasing impact stress. From the calculated reshock and release off-Hugoniot curves and the Hugoniot curve, the critical strength of the GRP in shock compression was determined. The critical

strength of GRP increased dramatically from 0.0268 GPa to 0.306 GPa in the test range.

The shock compression response of GRP experiments showed that GRP have good shock resistance but poor spall strength. The HEL of GRP was estimated to be around 1.6 GPa but the spall strength was below 0.05 GPa. The low spall strength suggests that more material development is required to improve the spall strength of composite armor systems. Pressure-shear plate impact spall experiments with skew angles larger than those employed in the present study could be used to help refine the failure surface for the GRP. Although the results from shock-resock and shock-release experiments showed clear strain hardening in the tested stress range, further exploration at higher stress range is necessary to fully understand the strain hardening behavior of GRP at higher stresses. Some recent research has also proposed that the addition of 1% by weight of nano-particles in GRP can increase the inter-laminar shear strength, bending strength and fracture toughness by at least 20%. More experimentation needs to be conducted along these lines to investigate the improvements in GRP's shock performance, in particular the dynamic material response and the spall strength of nano-particle reinforced GRP.